UNIVERSITY OF CALIFORNIA

Los Angeles

Development of a Combined microPET and microCT

System for Mouse Imaging

A dissertation submitted in partial satisfaction of the

requirements for the degree Doctor of Philosophy

in Biomedical Physics
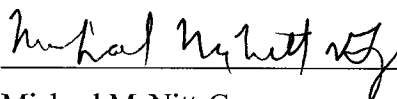
by

Andrew Leonard Goertzen

2003

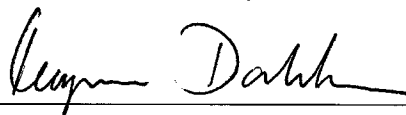The dissertation of Andrew Leonard Goertzen is approved.

John M. Boone

Simon R. Cherry

Michael McNitt-Gray

Magnus Dahlbom, Committee Co-chair

Edward J. Hoffman, Committee Co-chair

University of California, Los Angeles

2003

This work is dedicated to my wife, Cindy,

as we conclude one adventure and

begin another.

Table of Contents

List of Figures

List of Tables

Acknowledgements

I would like to begin by thanking my dissertation committee:

Dr. Simon Cherry – for being my advisor, securing the funding for the project, and keeping me around after the move to Davis. Your work was what brought me to UCLA in the first place. In the lottery that is picking an advisor, I think I lucked out.

Dr. Edward Hoffman – for co-chairing my committee and teaching me the importance of getting to know the people you work with outside of lab.

Dr. Magnus Dahlbom – for co-chairing my committee, and always being around to answer any questions about practical issues in image reconstruction and PET.

Dr. Michael McNitt-Gray – for raising valuable questions about validating experimental results and performing reality checks.

Dr. John Boone – for being a sounding board and endless source of information about the practical issues involved in microCT and x-ray detector performance.

I would like to thank the many fine people I met and worked with in the Imaging Sciences Lab at UCLA, many who have now moved on to other locations. Specifically, Dr. Randy Slates, Dr. Yiping Shao, Dr. Niraj Doshi, Dan Rubins, Dr. Yuan-Chuan Tai, Dr. Freek Beekman, and Ken Meadors.

I would like to thank Dr. Bob Silverman for all his help in getting the PET system electronics working, and for spreading his love of the finer things in life.

For their contributions to Chapter 4, and a crash course in the world of TLD dose measurements, Dr. Mercedes Rodriguez-Villafuerte and Dr. Arnulfo Martinez Davalos.

For help with image reconstruction, both through supplying code and helpful discussions, I thank Dr. Michel Defrise and Dr. Richard Leahy.

For help with navigating the administrative nightmare that is UCLA, I would like to thank Terry Moore, Maianh Nyugen, Blaine Sheppard, and Margy Blavin. To the International Students Office at UCLA, I would like to say thanks for nothing.

Finally, and most importantly, I would like to thank my family. My wife Cindy, for agreeing to move to Los Angeles in the first place, and then staying despite the pause this caused to your career. For putting up with my constant travelling to northern California, and motivating me to push for the finish. I could not have done this without you. Our parents, Leonard and Lottie Goertzen and Raymond and Alice Fleury, for all their support, visits, and interest in my progress. Our siblings, Bonnie, Nancy, Julie and Paul, along with their significant others, for their visits to make us not feel so far away from home.

Parts of Chapter 2 and Chapter 5 are a version of the paper "Simultaneous Anatomical and Molecular Imaging in the Mouse" by A.L. Goertzen, A.K. Meadors, R.W. Silverman and S.R. Cherry which appeared in Physics in Medicine and Biology, 47:4315-28, 2002.

Appendix A is a version of the paper "Effect of phantom voxelization in CT simulations" by A.L. Goertzen, F.J. Beekman and S.R. Cherry which appeared in <u>Medical Physics</u>, 29(4):492-8, 2002.

Figure 1.1A was supplied by Dr. Craig Abbey, UC Davis. Figure 1.1B was supplied by Dr. Anna Wu, UCLA. Figure 1.3 was supplied by Dr. Michael Paulus, Imtek, Inc., Knoxville, TN. Figures 2.3 and 2.4 were supplied by Thermotrex, Inc., San Diego, CA. Figures 4.1 and 4.2 are courtesy of Dr. Mercedes Rodriguez-Villafuerte and Dr. Arnulfo Martinez Davalos, IFUNAM, Mexico City, Mexico.

"Do or do not…. There is no try" – *Yoda*

VITA

June 14, 1976   Born, Winnipeg, Manitoba, Canada

1994   Chown Centennial Entrance Scholarship
University of Manitoba
Winnipeg, Manitoba, Canada

1997   Top Poster Award
Canadian Undergraduate Physics Conference
Vancouver, British Colombia, Canada

1994-1998   Canada Scholarship in Science and Engineering
Government of Canada

1997-1998   Student Researcher
Department of Physics and Astronomy
University of Manitoba
Winnipeg, Manitoba, Canada

1997-1998   Teaching Assistant
Department of Mathematics
University of Manitoba
Winnipeg, Manitoba, Canada

1998   B. Sc. (Hons.), Physics
University of Manitoba
Winnipeg, Manitoba, Canada

2001   M.S., Biomedical Physics
University of California, Los Angeles
Los Angeles, California

2001   Student Travel Scholarship
High Resolution in Small Animals Conference
Rockville, Maryland

2002   Student Travel Scholarship
IEEE Medical Imaging Conference
Norfolk, Virginia

2002   Norman Baily Award

Southern California Chapter of the American Association of Physicists in Medicine

1998-2002   Teaching Assistant
                     Department of Physics
                     University of California, Los Angeles
                     Los Angeles, California

1998-2003   Graduate Student Researcher
                     University of California, Los Angeles
                     Los Angeles, California

PUBLICATIONS AND PRESENTATIONS

Goertzen, A.L., Meadors, K., Silverman, R.W. and Cherry, S.R., "Simultaneous Anatomical and Molecular Imaging in the Mouse" Physics in Medicine and Biology, 47:4315-28, 2002.

Goertzen, A.L., Chow, P.L., Chatziiaonnou, A.F. and Cherry, S.R., "A Study of Image Quality and Dose vs. X-ray Beam Spectrum in Small Animal CT With an a-Se Flat Panel Detector" Presented at IEEE NSS-MIC, Norfolk, VA, 10-16 Nov. 2002.

Goertzen, A.L., Meadors, K., Silverman, R.W. and Cherry, S.R., "Simultaneous PET and x-ray CT imaging of the mouse" Presented at AMI Annual Conference, San Diego, CA, 23-27 Oct. 2002.

Goertzen, A.L., Beekman, F.J. and Cherry, S.R., "Effect of phantom voxelization in CT simulations." Medical Physics, 29(4):492-8, 2002.

Chow P.L., **Goertzen A.L.**, Berger F., DeMarco J.J. and Chatziioannou, A.F., "Monte Carlo model for estimation of dose delivered to small animals during 3D high resolution x-ray computed tomography" 2001 IEEE NSS Conference Record, San Diego, CA, 4-10 Nov. 2001, vol. 3., 1678-81.

Chow P.L., **Goertzen A.L.**, Berger F., DeMarco J.J. and Chatziioannou, A.F., "Monte Carlo model for estimation of dose delivered to small animals during 3D high resolution x-ray computed tomography" Presented at IEEE NSS-MIC, San Diego, CA, 4-10 Nov. 2001.

Goertzen, A.L., Meadors, K., Silverman, R.W. and Cherry, S.R., "Design of a Simultaneous Combined PET-CT Imaging System for Mouse Imaging."

presented at High Resolution Imaging in Small Animals conference, Rockville, Maryland, 9-11 Sept. 2001.

Page, J.H., **Goertzen, A.L.**, Yang, S., Liu, Z., Chan, C.T. and Sheng, P., "Acoustic Band Gap Materials." in *Photonic Crystals and Light Localization in the 21st Century*, edited by C. M. Soukoulis (Kluwer Academic Publishers, Amsterdam) pp. 59-68, 2001.

Goertzen, A.L., Beekman, F.J. and Cherry, S.R., "Effect of voxel size in CT simulations." 2000 IEEE NSS Conference Record, Lyon, France, 15-20 Oct. 2000, vol. 3., 20/93-7.

Goertzen, A.L., Beekman, F.J. and Cherry, S.R., "Effect of voxel size in CT simulations." presented at IEEE NSS-MIC, Lyon, France, 15-20 Oct. 2000.

Liu, Z., Chan, C.T., Sheng, P., **Goertzen, A.L.** and Page, J.H., "Elastic wave scattering by periodic structures of spherical objects: Theory and experiment." Physical Review B - Condensed Matter, 62:2446-57, 2000.

ABSTRACT OF THE DISSERTATION

Development of a Combined microPET and microCT

System for Mouse Imaging

by

Andrew Leonard Goertzen

Doctor of Philosophy in Biomedical Physics

University of California, Los Angeles, 2003

Professor Edward J. Hoffman, Co-chair

Professor Magnus Dahlbom, Co-chair

The mouse has become the laboratory mammal of choice in many areas of biomedical research. Mice are widely used for studying the basic biology of mammalian systems, to create models of human disease and for testing new therapeutic approaches in these models. The physiologic similarity and genetic homology with man, combined with the availability of sophisticated methods for genetic manipulation, their rapid breeding cycle and relatively low maintenance costs, have all contributed to the success of the mouse in the biomedical research laboratory. The completion of the mouse genome will only add to the opportunities for improving our understanding of mammalian biology and for creating new and improved models of human disease.

It has been widely recognized that non-invasive imaging technologies can provide a window into the biology of the living mouse. In this project we have developed a prototype bench-top combined x-ray computed tomography (CT) and positron emission tomography (PET) system designed specifically for mouse imaging. The x-ray system

consists of a compact mini-focal x-ray tube and an amorphous selenium (a-Se) flat panel x-ray detector. The PET system uses planar arrays of lutetium oxyorthosilicate (LSO) scintillator coupled to position-sensitive photomultiplier tubes. PET and CT images of both phantoms and mice were acquired simultaneously on this system.

The effect of the x-ray detector on the microCT system was investigated by comparing the performance of an a-Se detector, an amorphous silicon (a-Si) detector coupled to a gadolinium oxysulfide (GOS) screen, and a charge coupled device (CCD) detector coupled via to a GOS screen. The a-Se detector had the best performance as measured by the detective quantum efficiency (DQE), however reconstructed CT images acquired with the a-Si detector had lower noise. The effects of the x-ray spectrum on image contrast and radiation dose to the mouse were investigated, with the results showing that little contrast is lost through using a harder x-ray spectrum while dose is reduced significantly.

The goal of the bench-top PET-CT system was to study the effects of operating the two systems simultaneously and to optimize the microCT system for the specific task of mouse imaging.

Chapter 1. Background and Significance

1.1 Introduction

The goal of this project is to develop a combined Positron Emission Tomography and x-ray Computed Tomography (PET-CT) system for use in mouse imaging. It is believed that combining these two imaging modalities will allow better quantification of the PET images while at the same time making the PET images easier to interpret due to the anatomical information provided by the CT data.

1.2 Mouse Imaging

The mouse has become the laboratory mammal of choice in many areas of biomedical research. Mice are widely used for studying the basic biology of mammalian systems, to create models of human disease and for testing new therapeutic approaches in these models. The physiologic similarity and genetic homology with man, combined with the availability of sophisticated methods for genetic manipulation, their rapid breeding cycle and relatively low maintenance costs, have all contributed to the success of the mouse in the biomedical research laboratory. The completion of the mouse genome will only add to the opportunities for improving our understanding of mammalian biology and for creating new and improved models of human disease.

It has been widely recognized that non-invasive imaging technologies can provide a window into the biology of the living mouse. In many cases, this opens up the unique possibility of making repeated measurements of biologic function and specific molecular or genetic events within a single animal over time. A number of groups have been

developing micro-imaging technologies designed around the mouse, with the goal of integrating the opportunities created through research in mouse biology and genetics with the power of non-invasive or non-destructive imaging at the organ or whole-mouse level.

For example, *ex vivo* imaging techniques now exist to study mouse anatomy, pathology and development at extremely high (~10-100 micron) resolution using magnetic resonance microscopy (MRM) [Johnson et al., 1997; Jacobs et al., 1999], x-ray computed tomography (CT) [Jorgensen et al., 1998; Ruegsegger et al., 1996] high-frequency ultrasound [Pan et al., 1998] and optical techniques [Sharpe et al., 2002]. At somewhat reduced spatial resolution (~ 0.2–2 mm), these same techniques can also be used to produce images of anatomy *in vivo* [Paulus et al., 2000; McDaniel et al., 2001; Foster et al., 2000]. In addition, highly sensitive techniques also are being developed that produce *in vivo* images of specific biochemical pathways, molecular targets and gene expression/regulation using targeted contrast agents [Ntziachristos et al., 2002]. These contrast agents use a variety of signal-producing mechanisms, including radioactive decay [Gambhir et al., 2000], fluorescence [Weissleder et al., 1999], bioluminescence [Contag et al., 2000], acoustic echoes [Lanza and Wickline, 2001], and the interaction of water molecules with paramagnetic ions [Louie et al., 2000]. The corresponding *in vivo* imaging technologies include positron emission tomography (PET), single-photon emission computed tomography (SPECT), optical imaging, high-frequency ultrasound and magnetic resonance imaging (MRI).

1.3 PET

Positron emission tomography is an imaging modality that provides functional data by imaging the distribution of a radioactive tracer in the body [Budinger et al., 1996; Phelps, 2000]. In a conventional whole-body PET scanner, detectors are arranged in a ring geometry that surrounds the patient. When a positron is emitted from the radionuclide and annihilates with an electron in the patient, two 511 keV annihilation photons are produced travelling at 180° to each other. If the two 511 keV annihilation photons are detected within a given coincidence time window, then an annihilation event is determined to have occurred and it is binned into the appropriate line of response [Phelps et al., 1978; Sorenson and Phelps, 1987]. After collecting millions of these coincident annihilation events, images are reconstructed using filtered backprojection [Shepp and Logan, 1974] or iterative methods [Vandenberghe et al., 2001].

A nuclear medicine scan is only as effective as the tracer used in the imaging. In PET, the most common tracer used is ^{18}F-fluorodeoxyglucose (FDG) [Phelps et al., 1979; Czernin, 2002]. This tracer is very useful since it is a glucose analog that images glucose metabolism. FDG has been used for studies ranging from brain function assessment for early detector of Alzheimer's disease [Azari et al., 1993] to staging of cancer [Gambhir, 2002]. Since FDG traces glucose metabolism, FDG-PET produces images with a relatively high level of anatomical information, since all cells in the body take up glucose, as shown for the case of a mouse FDG image in figure 1.1A.

In recent years PET imaging of animals has become a popular research area [Cherry and Gambhir, 2001] due to the ability to perform *in vivo* longitudinal studies on

the same animal. This allows each animal to act as its own control and thus reduces the effects of inter-animal variability. To take advantage of the ability of PET to assess function *in vivo*, novel new methods such as labeled antibody fragments [Wu et al., 2000; Yazaki et al., 2001] and "marker/reporter genes" [Gambhir et al., 2000] have been developed. These new tracers are designed to bind to cells based on their levels of expression of certain genes or proteins and as a result are usually only concentrated in a few discrete areas in the body, resulting in images with very little anatomical information. An example of such a study is shown in figure 1.1B. This is a PET image of an athymic mouse with a tumour xenograft which expresses the carcinoembryonic
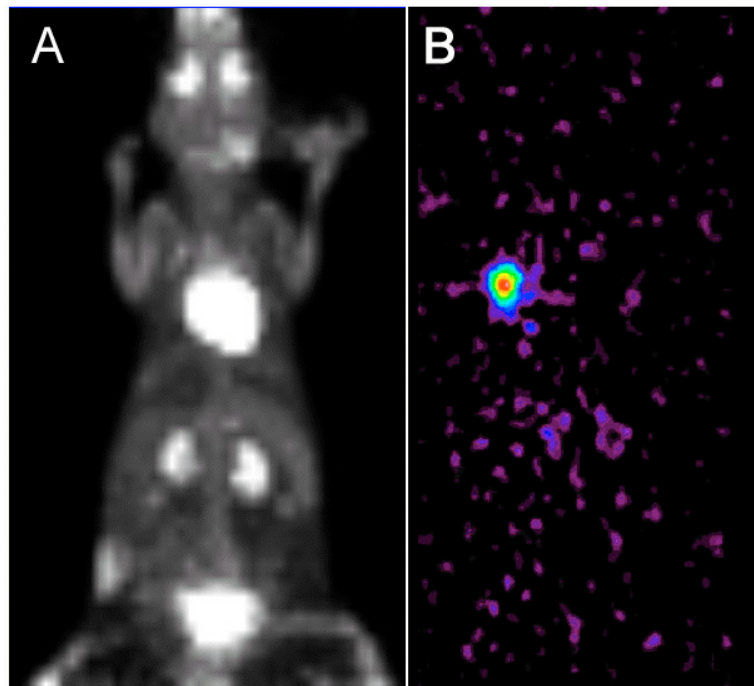
Figure 1.1. A) ^{18}F-FDG microPET image of a mouse. Note the large amount of anatomical detail and the lesion near the left hind leg. B) microPET image of an athymic mouse using an ^{124}I labeled anti-CEA diabody tracer. Note the complete lack of anatomical information in the image, with only the tumour showing uptake of the tracer.

antigen (CEA). This mouse was imaged using an ^{124}I labeled anti-CEA diabody, or modified antibody, tracer. One can see that there is no anatomical information in this image, although one might conclude that the hotspot is the likely location of the tumour cells against which the diabody is directed.

In cases where the region of interest is not a tumour xenograft, but rather say an internal organ, identification of the location of uptake can be much more difficult. It is

Figure 1.2. The UCLA microPET.

studies such as these that have led to a demand for dual-modality scanners that can provide both functional and anatomical information.

1.4 Animal PET Systems

In this section a survey of several dedicated animal PET systems is presented. This list does not cover all animal PET systems in existence but rather highlights several systems which use different detector technologies.

1.4.1   The UCLA microPET

The UCLA microPET was constructed in 1997 [Cherry et al., 1997; Chatziioannou et al., 1999]. Since construction, over 3000 scans have been performed on this system. The microPET system consists of a ring of 30 position-sensitive scintillation detectors, each with an 8×8 array of $2 \times 2 \times 10$ mm^3 lutetium oxyorthosilicate (LSO) crystals coupled via optical fibres to a multi-channel photomultiplier tube. The reconstructed image resolution 1 cm from the centre is 2.0 mm, giving a volumetric resolution of 8 mm^3. The system has an absolute sensitivity at the centre of the field of view (CFOV) of 0.4% when the energy window is set at 350 to 650 keV. The coincidence timing window is set at 12 ns. There is no measured attenuation correction used on this system. A picture of the system is shown in figure 1.2. This biggest advantages of this system are the good resolution and very stable performance. The use of a single ring of detector modules means that the sensitivity of the system is limited.

1.4.2   The Concorde microPET P4

The Concorde microPET P4 [Tai et al., 2001] (Concorde Microsystems Inc., Knoxville, TN) is the commercial version of the UCLA microPET. It inherits the fundamental detector design of the prototype system, with 8×8 arrays of LSO being coupled via fibre optics to PS-PMTs. The crystal size is $2.2 \times 2.2 \times 10$ mm^3, with each array being cut from a single continuous block of LSO. The microPET P4 system consists of 4 rings, each with 42 detector modules, for a total of 168 detectors. The primary advantage of the P4 system over the prototype microPET is the increased axial field of view, which at 7.8 cm is sufficient for whole body mouse imaging. The system has a resolution at the CFOV of 1.8 mm FWHM, with resolution within a 4 cm radial offset being under 2.5 mm. The greater axial field of view leads to a much larger absolute sensitivity of 1.43% at the CFOV for the $350 - 650$ keV energy window. The resolution of this system is slightly worse than the prototype microPET owing to the slightly larger crystal size. The coincidence timing window is set at 10 ns. There is the option for a measured attenuation correction using a rotating point source, which will allow for improved quantitation of the PET images.

1.4.3   Oxford Positron Systems quad-HIDAC

The quad-HIDAC (Oxford Positron Systems, Weston-on-the-Green, Oxfordshire, UK) is based on multiwire proportional chamber technology that leads to large-area high-resolution detectors [Jeavons et al., 1999]. The HIDAC system produces images with an excellent resolution of 0.95 mm FWHM at the CFOV, with resolution remaining

approximately less than 1.5 mm within the FOV. The absolute sensitivity of the system is 0.9% at the CFOV. The gas detector design means that there is inherently poor count rate performance since the coincidence window is set at 60 ns. This large timing window means that the effect of random coincidences will be much larger than for a scintillator based system. Since a gas detector has poor energy resolution, the effect of scatter will be greater in this system than in a scintillator based system. There is no measured attenuation correction on this system. The poor count rate performance of this system means that the activity in the FOV must be kept low to avoid saturating the system. However, for point-like sources in a minimally scattering environment (e.g. a mouse ^{18}F$^-$ bone scan) excellent images should be seen due to the reasonable sensitivity and excellent resolution.

1.4.4   Sherbrooke APD PET

Roger Lecomte's group at the University of Sherbrooke has built a dedicated animal PET system based on avalanche photodiodes (APDs) [Lecomte et al., 1996]. This system consists of 2 rings of $3 \times 5 \times 20$ mm^3 BGO crystals in a ring of 310 mm diameter. The resolution of the system is 2.1 mm FWHM at the CFOV, falling to 2.4 mm at 1 cm from the centre. The volumetric resolution of this system is not at good at the UCLA microPET due to the larger dimension extent of the crystals. The scanner absolute sensitivity is 0.51% at the CFOV. A coincidence window setting is not quoted for this system, and no measured attenuation correction is used. This system is a prototype to prove that APDs can be viable as detectors for a PET system, and is in many ways

limited by the current state of APD development and electronics to read out the APDs. Since they are silicon devices, the potential for mass-produced cheap APDs exists, and at that time they may replace PMTs as the photon detector of choice for scintillation detectors.

1.4.5   NIH ATLAS Small Animal PET Scanner

The NIH ATLAS system [Vaquero et al., 2001] is based on a two layer LGSO-GSO scintillator crystal structure coupled to Hamamatsu R7600-C8 PMTs. The system consists of 18 phoswich detector modules arranged in a ring 11.8 cm in diameter. Each module consists of a 9×9 array of $2 \times 2 \times 15$ mm^3. The modules have a two-level depth of interaction resolving capability since the decay time of the GSO (60 ns) is slower than the decay time of the LGSO (40 ns), and the differing decay time is discriminated in the digitizer electronics. The crystal pitch is 2.25 mm. Complete performance results for this system have not yet been published. The small ring diameter together with the 15 mm deep crystals should create a high efficiency, while the increased sampling due to the dual layer scintillator should improve on the resolution of the system. However, the multi-layer design means increased complexity in the data handling due to factors such as normalization for a line of response (LOR) between crystals located in different rings and uneven sinogram spacing for the LORs between different rings.

1.4.6   Future Directions of Small-Animal PET

With the exception of the Oxford Positron Systems quad-HIDAC system, all currently used small-animal PET systems are based on pixelated crystal scintillator arrays coupled to either PMTs or APDs. Most of these systems have crystal elements close to 2 mm in size. While this design has proven successful, it also ultimately places limits on the performance of a small-animal PET system. Recent work on the microPET II system [Chatziioannou et al., 2001] has shown that the limit of how far the pixelated crystal design can be pushed is being approached. The microPET II system is based on $1 \times 1 \times 12.5 \text{ mm}^3$ LSO crystals coupled to multi-channel PMTs. Despite its 1 mm crystal size, the measured resolution of the system remains above 1 mm due to difficulties in resolving the individual crystal elements and the fact that the crystals are arranged in a multi-sided polygon rather than a true circle. Going to a continuous detector or perhaps a solid-state detector such as cadmium zinc telluride (CZT) could alleviate some of these issues.

In order to get around the problems inherent to pixelated crystal systems, two approaches can be utilized. The first is to improve the design of the detectors through approaches utilizing continuous detector elements. The second approach is to improve the data through software corrections. Approaches using system modeling [e.g. Bai et al., 2002] can improve the image quality and quantification.

Proper quantification of PET images [Visvikis et al., 2003] and modeling of the scattering medium (the mouse) [Holdsworth et al., 2002] requires accurate anatomical information obtained through a transmission scan. Anatomical information can either be

provided by a transmission scan using a radioactive source or through incorporating a x-ray source [Zaidi and Hasegawa, 2003]. Using the x-ray source for a CT scan results in an attenuation map that has a much better signal to noise ratio (SNR) than the radioactive source. For all of these reasons, there are compelling reasons to include x-ray CT capability in future small-animal PET systems.

1.5 X-ray CT

X-ray computed tomography is an imaging modality that provides anatomical data by measuring the attenuation of a beam of x-rays as it passes through an object. In order to reconstruct two-dimensional images of a slice of the object, x-ray projection data must be measured along multiple lines and at multiple angles. In the first successful CT scanner [Hounsfield, 1973], for which Godfrey Hounsfield and Allan Cormack received the Nobel prize for medicine in 1979, projection data was measured along a narrow pencil beam in a rotate/translate method. In this method, an x-ray tube and a single detector were translated across the width of the patient, then rotated by 1°, and again translated across the patient. This process was repeated until data had been measured for a 180° of rotation about the patient. This system produced an 80×80 image with a 3 mm pixel size, and each slice required approximately 4.5 minutes of scanning time and 1.5 minutes of reconstruction time.

Rapid advances in computer systems and detector electronics in the late 1970s and 1980s, along with improvements in image reconstruction [Shepp and Logan, 1974], made possible x-ray CT systems of much greater complexity. These systems utilize

hundreds to thousands of detector elements and can acquire a slice of data in under a second. This advance in system complexity was also made possible by the large and immediate of interest in clinical use of the CT scanner [Hounsfield, 1980] due to its ability to differentiate between tissue types in the body and to see physical deformities in the brain.

1.6 Dedicated Mouse CT Systems

The design of microCT systems is largely constrained by the availability of detectors and x-ray sources to use. In order to be of a practical nature for a mouse imaging centre, the scanner can not be of the dimensions of a human clinical scanner. The limit on size imposes a direct limit on the choice of x-ray tube. Human CT systems utilize very large rotating anode x-ray tube designs capable of 140 kVp and hundreds of mA of tube current [Bushberg et al., 1994]. A tube of this size and cost, not to mention the associated power supply, is not practical for a mouse CT system, meaning that lower output, stationary anode x-ray tubes must be used instead. This use of low output x-ray tubes means that the limiting factor to image acquisition is the x-ray flux that the x-ray tube can put out. It is thus essential that the maximum usage be made of the x-ray flux that the tube does put out. The most efficient way to use the x-ray flux is to acquire a 2D projection image at each rotation step instead of a single slice as is done in most human CT systems. However, this approach necessitates the use of 3-D reconstruction methods and also leads to an increased amount of scatter in the projection data.

Several mouse CT systems have become available commercially in recent years. This section presents a review of several of these systems. Again this list of systems is not an inclusive list of all systems available, but does cover the major suppliers of rodent x-ray systems. Most commercially available systems for imaging mice or specimens have a common trait in that they utilize a charge coupled device (CCD) for the detector. The *in vivo* systems also share a similar geometry where the mouse is placed on a horizontal bed and the detector and x-ray source are rotated around the mouse. These are different from dedicated *ex vivo* specimen scanners, in which the object being imaged is typically placed on a rotation stage and rotated in order to acquire tomographic data.

Small animal CT is now at the point where there are systems being manufactured by various manufacturers based on primarily identical system designs, with things such as reconstruction time being one of the few things to differentiate the systems. There is as yet no specific performance measurements specified to characterize microCT system performance, as the resolution and sensitivity measurements can characterize a PET system. Thus comparing the various systems is difficult. In most of these microCT systems, the resolution is quoted as being the reconstruction voxel size, and no discussion is made about contrast or noise in images. For these reasons, the listing of microCT systems that follows can do little more than discuss the hardware components and quoted reconstruction time for the systems.

1.6.1   Imtek Inc. microCAT

Intek Inc. (Imtek Inc., Knoxville, TN) manufactures a dedicated mouse x-ray CT system, called the microCAT, which is based on a prototype built at the Oak Ridge National Laboratory [Paulus et al., 1999]. The Imtek microCAT system utilizes a CCD detector fibre optically coupled to a phosphor screen. The x-ray tube is a 50 kVp 75 Watt model (Oxford X-ray Instruments, Scott's Valley, CA). Such a system has been recently installed at UCLA. This system can image a mouse in 2 bed positions. The data acquisition rate is 2 s per frame, with one frame being 1024×1024 pixels. Newer versions of this system incorporate a larger CCD camera capable of imaging a whole mouse in one bed position. The data is acquired in a cone-beam geometry and is reconstructed using cone-beam filtered back projection [Feldkamp et al., 1984]. The reconstructed image has a voxel size of either 50 μm or 100 μm. An example of a reconstructed image of a mouse from the microCAT is shown in figure 1.3. Newer
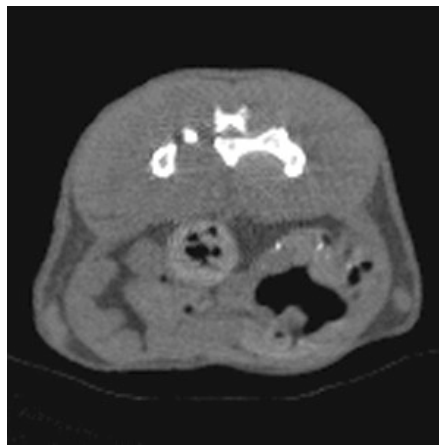
Figure 1.3. A reconstructed image from the Imtek microCAT showing a slice through the abdomen of a mouse. (Image courtesy of Imtek Inc., Knoxville, TN)

versions of this system have available as an option a dedicated high-speed reconstruction engine so that the images are reconstructed nearly simultaneously with completion of the scan.

1.6.2 *Enhanced Vision Systems Corp./GE Medical Systems microCT*

Enhanced Vision Systems Corp./GE Medical Systems (EVS/GEMS, London, Ont., Canada) manufactures a microCT system, called the RS-9 Small Animal Micro CT scanner. This system utilizes a CCD detector and an x-ray tube capable of 20 – 90 kVp. The system is capable of either 45 or 90 μm resolution, with typical scan times of 3-15 minutes.

1.6.3 *SkyScan 1076 In-Vivo microCT System*

The SkyScan 1076 microCT system (SkyScan, Aartselaar, Belgium) incorporates a 4000 × 2300 pixel CCD detector and a x-ray tube capable of 20-100 kVp. The reconstruction voxel size is 9, 18, or 35 μm. The novel component of this system is the inclusion of an animal physiological monitoring system, consisting of a small camera to monitor movement, and monitors for temperature, ECG, and breathing. Using this monitoring system, the data being acquired can be gated for breathing and heartbeat, providing images free of motion artifacts.

1.6.4   Future Directions of mouse CT Imaging

All of the currently available microCT systems used for mouse imaging are based on CCD detectors coupled via fibre optic taper to a scintillating screen. This method has been used primarily because it has allowed the rapid construction of a system. Because of the similar detector, the systems all are capable of approximately similar performance. Unfortunately, all of the systems also have the same drawbacks as a result. It is not clear whether the CCD camera is the optimum x-ray detector for mouse imaging, and thus an evaluation of how the performance of a CCD camera compares to other devices is needed. Due to the 2-D projection acquisition, all of these systems will have a significant amount of scatter in the projection data. All of these system utilize a simple circle orbit for data acquisition and the Feldkamp cone beam reconstruction algorithm to reconstruct the data. The result of these choices is that the reconstructed data away from the central plane will have artefacts due to incompleteness of the data. Due to the low energy used (typically around 40 kVp), beam hardening can be a significant problem in mouse microCT images. None of these systems incorporate a beam hardening correction option. The performance of each of these systems could likely be improved through the incorporation of such corrections to the data.

1.7 Motivation for Dual-Modality Systems

Most *in vivo* molecular imaging techniques, as mentioned in section 1.2, use contrast agents or imaging probes that are targeted to specific enzymes in a biochemical pathway, bind to specific receptors, or that accumulate in a specific fashion in cells

expressing particular genes or proteins. Another way to utilize these imaging techniques is in cell trafficking studies in which a small number of cells are directly labeled with contrast agent. After introduction into the animal, the distribution and localization of the labeled cells can be studied over time. In many cases, the specific signal created by the contrast agent or imaging probe and measured by the imaging device, will be localized in certain organs or cell populations. Furthermore, many agents can also produce non-specific signal from circulating contrast agent in the blood, non specifically bound agent in the tissue, and from routes of excretion, commonly either the renal system or the hepatobiliary system. In the absence of explicit anatomic information, interpretation of molecular imaging studies, both in terms of precise localization of the signal, and separation of specific and non-specific signal, can be extremely difficult. For this reason, there is considerable interest in integrating different imaging techniques that can provide both anatomical and molecular imaging information in the same experimental animal [e.g. Da Silva et al., 2001; Williams et al., 2000; Shao et al., 1997].

In addition to providing directly registered images, the combination of functional PET imaging and an anatomical modality, such as CT or MRI, can bring additional benefits in terms of accurately quantifying the PET signal *in vivo*. One of the major errors in quantifying radiotracer concentrations with PET is caused by attenuation of the 511 keV photons in tissue. In the mouse this error is on the order of 10-20%. The CT scan is a direct image of the attenuation of tissue at the lower x-ray energies and can be used to compute the attenuation coefficients at 511 keV (using the known attenuation of tissue and bone as a function of energy) [Kinahan et al., 1998]. The other major

quantitative error in PET is caused by the partial volume effect [Hoffman et al., 1982]. This leads to significant errors in quantifying radiotracer concentrations, when the dimensions of the structure(s) of interest are comparable to or smaller than the resolution of the imaging device [Meltzer et al., 1990]. The error is directly related to the physical shape and volume of the structure and the distribution of the radiotracer. The resolution of current small animal scanners is at best 1-2 mm, and therefore many structures of interest are subject to this error. The higher resolution CT images can be used to provide a first-order correction for this partial volume effect by providing an estimate of the size of the organ or structure of interest.

A particular interest is in using this type of dual-modality imaging system to identify the time at which metastasis emerge in mouse models of cancer, and to accurately localize these metastasis for detailed histochemical and genomic analysis using other techniques. We believe this, and similar studies, in which imaging is used to detect the timing and location of biologic events of interest, thereby directing tissue collection for further detailed analysis, will be an important application of this technology. Other applications might include cell trafficking studies (the CT images providing the localization of radiolabeled cells detected by PET imaging) and whole-body anatomical and metabolic phenotypic screening studies.

1.8 Dual-Modality Imaging Systems

Several dual-modality imaging systems that have been built by different groups are reviewed in this section. Only those systems that combin anatomical (CT, MRI, etc.) and functional (PET, SPECT, etc.) modalities are discussed.

1.8.1   PET-MRI System for Animal Studies

A PET system capable of operating inside a MRI scanner was constructed at UCLA in 1996 [Shao et al., 1997]. This system consisted of a single ring of 48 $2 \times 2 \times 10$ mm^3 LSO crystals in a 38 mm diameter ring. The crystals were coupled to multi-channel photomultiplier tubes (MC-PMTs) by 4 m long double-clad optical fibres. The system was operated successfully inside various MRI systems to acquire simultaneous PET and MR data [Slates et al., 1999a].

This PET system was too small to use for routine animal studies and as a result the next generation system is currently under construction [Slates et al., 1999b]. This new design will utilize three layers of LSO crystals in a single ring to give depth of interaction information to compensate for the small ring size. This new system will still be only a single ring PET system and as such limited in the types of studies that can be performed on it. The ultimate goal of this project is to develop a human brain PET scanner that can be used in conjunction with MRI.

While the concept of combined PET-MR is attractive, it has proven very difficult to implement in practice. Only single ring PET systems have been developed capable of being put in the bore of a MR system magnet, and this means that the PET system is not

practically useful for routine imaging due to its low sensitivity. The single ring PET system design is necessary because the light from the scintillation crystals must be piped out along fibre optic tapers to PMTs that are sufficiently far away from the magnet. Clearly to make this a routinely usable technology, photon detectors that are immune to magnetic fields are required.

1.8.2 PET-CT Scanner for Human Imaging

A combined PET-CT system was designed and built at the University of Pittsburgh by David Townsend's research group [Beyer et al., 2000]. The scanner is based on a combination of a spiral CT scanner, a Somatom AR.SP (Siemens, Iselin, NJ), with the PET components from a rotating partial-ring tomograph, an ECAT ART scanner (Siemens). The two systems are mounted on one gantry but are offset axially by 60 cm. This design results in a scanner tunnel some 90 cm long.

The typical protocol for imaging patients is to perform a post-injection CT scan (requiring 5-10 minutes) followed by a multibed PET acquisition (45-60 minutes). It was important that the CT scan be done post-injection due to the 60 minute uptake time of FDG. It would be an unacceptable use of the scanner time to perform the CT scan, inject the patient with FDG, wait one hour (with the patient unable to move in this time), and then perform the PET scan. Fortunately, it was found that the activity in the patient did not produce any noticeable artefacts in the CT scan. Since the CT scan only accounts for about 15% of the scan time, there was no great benefit in attempting simultaneous PET-

CT acquisition. Attempting simultaneous data acquisition proved impossible in this case due to the enormous scattered x-ray flux into the PET detector elements.

This scanner has been very useful in imaging oncology patients. The ability to have perfectly registered functional and anatomical information has been very useful in planning treatment protocols for patients, identifying and staging lesions, and directing biopsies. The success of this prototype system has led several companies to begin producing commercial PET/CT products for clinical use, all based on the same design of having PET and CT systems offset axially on a single gantry. This approach has proven to be an effective, if not particularly elegant system design. Approaches using a single detector for both imaging modalities could represent the next step forward in combined PET/CT systems [e.g. Iwata et al., 2000]. However such a system usually represents a compromise in either PET or CT system performance and generally such compromises are not looked upon favourably in a clinical setting.

1.8.3 CT-Scintillation Camera for Human Imaging

A x-ray CT system was combined with a scintillation camera for tumour localization by Bruce Hasegawa's group at the University of California, San Francisco [Tang et al., 1999]. This system combines a GE 9800 Quick x-ray CT system (General Electric Medical Systems, Milwaukee, WI) with a GE 600 XR/T scintillation camera. The two systems are placed next to each other such that the same patient bed can be used for both systems. The scintillation camera could be rotated to produce SPECT images.

The patient protocol for this system is very similar to that described earlier for the PET-CT system.

The data from this system was used to quantify radiopharmaceutical concentrations in patients using *a priori* knowledge of the volume of interest (VOI) information available from the CT data. Their goal is to achieve quantification of the VOI using a planar nuclear medicine scan only and using the CT images to determine the region in which the activity is concentrated. Their phantom experiments to this end have been fairly successful, with measured activity concentrations being within 10% of their true values. Experiments with patients have shown that the technique is clinically viable.

This system demonstrates the usefulness of having x-ray CT data to help with the interpretation of nuclear medicine scans even if the nuclear medicine scan is not a tomographic data set.

1.8.4   Combined Scintimammography-Digital X-ray Mammography

Mark Williams' group at the University of Virginia has built a prototype combined scintimammography-digital x-ray mammography system [Goode et al., 1999]. The digital x-ray system consists of a 3×2 array of CCD detectors coupled via fibre optics to a phosphor screen. These detectors are mounted on a LoRad MIII mammography chassis. The scintillation camera is based on arrays of $3 \times 3 \times 6$ mm^3 CsI crystals coupled to PS-PMTs via a light guide.

A mammogram is first acquired and then the gamma camera is moved over the area of interest. The patient's breast remains compressed for the duration of the

scintimammography study in order to improve image registration and reduce scatter of the gamma rays. The resulting images are fused to show where the regions of increased tracer uptake are localized in the breast.

This system is useful for showing how scintimammography images compare to standard x-ray mammograms since there is no motion between the two scans. Unfortunately, this also means that the patient's breast must remain compressed for a lengthy period of time. Since both methods are planar techniques, there is no information about the depth of a detected lesion. This lack of depth information can make the results of the scintimammography study difficult to determine since the amount of attenuation and scatter can not be quantified.

1.9 Project Goal and Outline of Dissertation

It is the ultimate aim of this project to develop a combined, simultaneous PET-CT system for use in routine mouse imaging. However, for this dissertation, the work will focus on building a prototype bench-top PET-CT system. This system will be designed specifically to study the impact that both imaging systems have on each other when operated simultaneously and to optimize the performance of both systems for the specific application of combined PET and x-ray CT imaging. The target performance for the bench-top system is to image a mouse simultaneously on the PET and CT systems, with an imaging time of less than 20 minutes. Since development of new PET detectors is not the focus, the PET system will utilize a standard block detector design.

The majority of the work will focus on the development of the microCT system for mouse imaging. A human is approximately 30 cm across and the resolution of state of the are human CT scanners is around 1 mm. In order to produce comparable images of a mouse, which is approximately 3 cm across, a resolution of around 10 times better is required. The target resolution of the CT system will be 150 μm. This value is chosen since with a 150 μm voxel size and a 256×256 voxel image, the reconstructed FOV is 3.84 cm, which is sufficient to image a mouse plus the bed the mouse is placed on. The image acquisition time will be less than 15 minutes for a routine scan. It will produce images of sufficient contrast to delineate soft tissue differences in the mouse. The resolution target of 150 μm represents a compromise between the need for high resolution images and practical issues such as dose to the mouse, data set size, and acquisition time. The resolution and imaging time targets are also partially chosen in order that the system was comparable or superior to existing stand-alone systems. This is done so that use of the CT system in the combined PET-CT system will not represent a compromise to the user in the quality of the data.

The initial portion of this work, discussed in chapter 2, focused on the development and construction of a microCT system suitable for *in-vivo* mouse imaging utilizing an a-Se x-ray detector. Factors considered in this development included the corrections necessary to the raw x-ray projection data in order to reconstruct high quality CT images, accurate geometric calibration of the system, and operational parameters of the system.

Following construction of this microCT system, the performance of the a-Se detector was compared with that of various other x-ray detector technologies, including the more conventional CCD device, through measurement of the detective quantum efficiency and the modulation transfer function. These comparisons are discussed in chapter 3.

It is generally considered that radiation dose to the mouse is the limiting factor in pushing the performance of an *in-vivo* microCT scanner [Ford et al., 2001]. The radiation dose given to a mouse during a typical scan on the prototype microCT system was estimated through thermoluminescent dosimeter measurements. These measurements, discussed in chapter 4, were compared to the results given by computer simulations as well as published results from other groups.

The a-Se microCT system was combined with a benchtop small field of view PET system in order to acquire simultaneous PET and CT data. This proof of principle system, described in chapter 5, showed that combined PET/CT imaging of the mouse is in fact practically possible in one system.

Chapter 2. Development of a Benchtop X-ray CT System for Mouse Imaging

2.1 Introduction

The x-ray system is a simple PC-based setup, with a x-ray tube and digital detector controlled by data acquisition cards in the PC. X-ray exposures are controlled by a mechanical shutter in front of the x-ray tube and moved with a stepper motor. To generate CT data, the object to be scanned is placed on a rotation stage between the x-ray tube and the detector. The equipment is mounted on an optical breadboard. The goal of this system design was to have maximum flexibility in order to be able to easily vary the geometry and acquisition parameters in order to explore optimization of these parameters. The second primary goal of this work was to develop a dependable method of CT data acquisition that produced high quality CT images of a mouse, with a resolution of around 150 μm and an acquisition time of less than 15 minutes. A diagram of the experimental
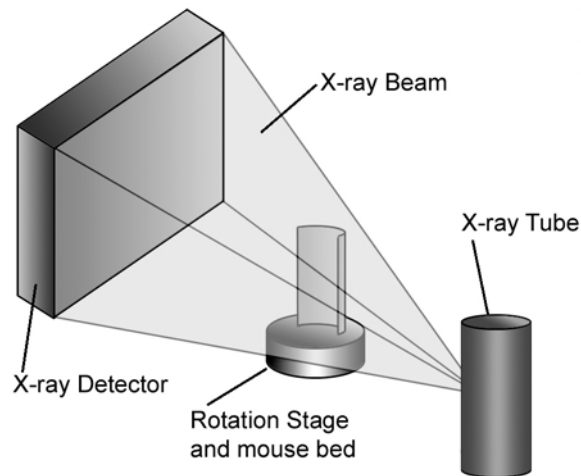
Figure 2.1. Experimental setup for the x-ray system.

setup is shown in figure 2.1. The x-ray hardware is described in section 2.2. The process

of acquiring a x-ray image and a description of the corrections applied is given in section

2.3. The CT image reconstruction process is described in section 2.4. The choice of

operating parameters such as x-ray tube settings is discussed in section 2.5. Finally,

section 2.6 deals with the limitations of the system as constructed.

2.2 X-ray Hardware

2.2.1   X-ray Detector

The job of all digital x-ray detectors is to convert the x-ray photons into electrical

charge that can be collected and digitized. There are two classes of detectors that can be

used to perform this job. The first class of detector is the indirect detector, as shown in

figure 2.2A. This class of detector utilizes a scintillator to convert the x-rays into visible

light, which is then collected by a detector sensitive to visible light. An example of such

a detector is a phosphor screen coupled to a charge coupled device (CCD). The second
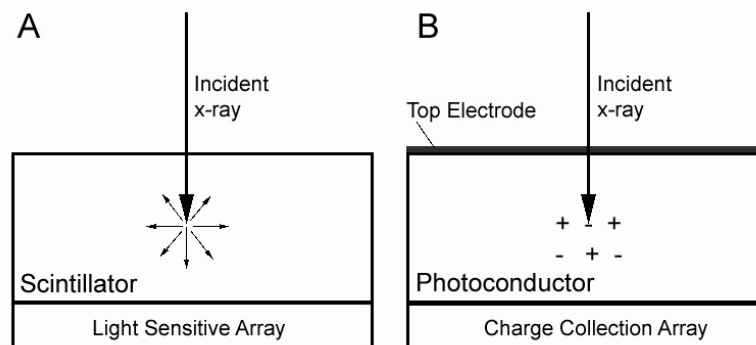
Figure 2.2. Schematic diagrams showing indirect (A) and direct (B) detectors. In the
indirect detector, the incident x-ray is converted to light, which then produces charge in
the detector array. In the direct detector, the incident x-ray produces charge directly in
the photoconductive layer, and this charge is collected by the detector array.
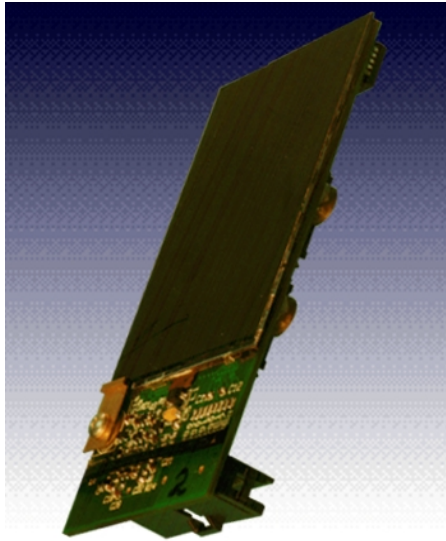
Figure 2.3. Picture of bare x-ray detector. Note the readout electronics on the chip at the base. (Image courtesy of Thermotrex Inc.)

class is the direct detector, as shown in figure 2.2B. This class of detector consists of a photoconductive layer that directly converts the x-rays into electron-hole pairs. An applied electric field forces the charges to opposite sides of the photoconductive layer where they are collected and stored in an array of capacitors until the array can be read out. Examples of such detectors include a-Se and HgI. Direct detectors have an advantage over indirect detectors since there is one less step in the chain between x-rays and charge. This means that there is one less step to add noise to the image. Indirect detectors tend to be less expensive since CCDs are a more mature technology.

The digital x-ray detector chosen for the initial work consists of a uniform 250 μm layer of amorphous selenium (a-Se) deposited on a CMOS readout array (Thermotrex Inc., San Diego, CA) [Andre et al., 1998]. The detector is an array of 1024×832 pixels with a 66 μm pixel pitch, creating an active area of 67.5×54.9 mm^2. An image of the

bare detector is shown in figure 2.3. The integrated circuit design of the CMOS read out array allows the pixel readout circuitry to be placed on the end of the detector. This detector is placed inside an aluminum housing containing the associated electronics. There is a carbon fibre plate over the detector to protect it and keep it dark, as the selenium is slightly light sensitive. This detector was chosen for the initial experiments because it was known to have a very good resolution and sensitivity for the x-ray energy range that would be used to image mice. A secondary reason for the choice was to study the advantages and disadvantages of a direct detector relative to the more commonly used indirect detector.

When an x-ray is absorbed in the a-Se layer, the x-ray energy creates electron-hole pairs in the selenium layer. An electric field of approximately 800V applied across the a-Se forces the charge to be collected at small pixel-sized electrodes on the top layer of the CMOS array. Figure 2.4 shows a cross section of the detector. The electrodes are connected to small capacitors which collect the charge and produces a voltage, V, such
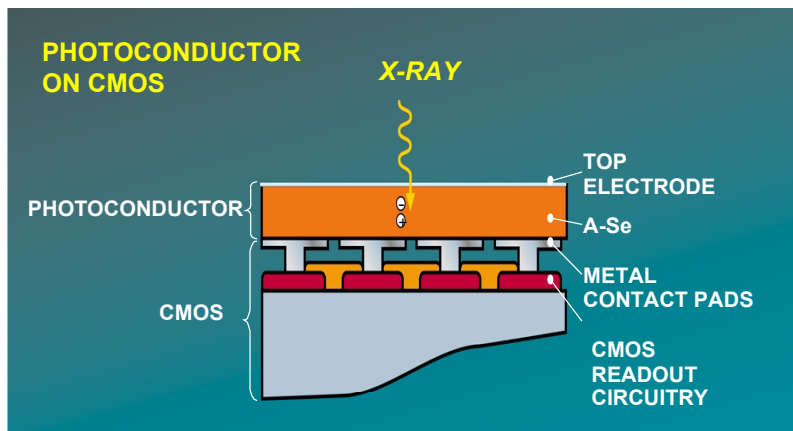
Figure 2.4. Cross section of the X-ray detector. (Image courtesy of Thermotrex Inc.)

29

that

$$V = Q_{in} / C_{pix} \qquad\qquad (Eq.\ 2.1)$$

where Q_{in} is the charge collected and C_{pix} is the capacitance of the pixel. Unlike silicon detectors where the electrons are more mobile than the holes, selenium has holes with greater mobility than the electrons. Thus it is the holes that are collected at the capacitors.

After an exposure is made, the pixel voltages are digitized using 8 parallel onboard 12 bit digitizers. The image is stored onto random access memory (RAM), where it can be stored until the host computer is ready to download the data. In this manner multiple images can be stored and downloaded when it is convenient. The data link between the detector and the PC is a 30 MByte/s fibre optic link. The time to digitize the image is approximately 0.5 s and the time to upload the image to the host PC is 0.06 s.

Selenium detectors are known to have some level of image "ghosting", or
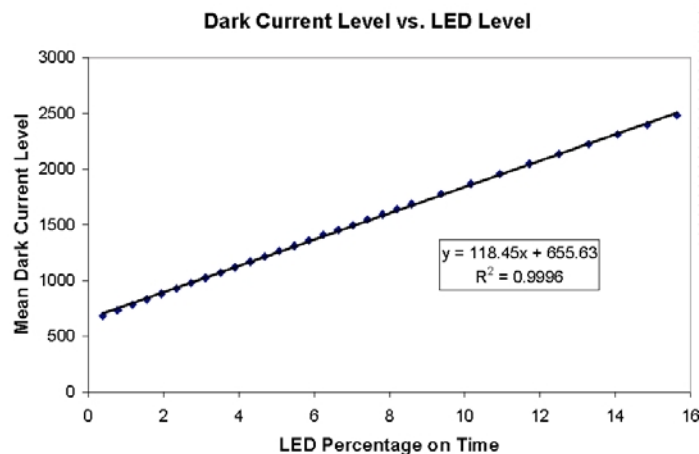
Figure 2.5. Plot of dark current level in the a-Se detector vs. LED percentage on time. Note the linear nature of the response with an R^2 value of 0.9996.

retention of the previous exposure which affects the next exposure [Chotas et al., 1997]. To help control ghosting on this detector, there are a series of light emitting diodes (LEDs) inside the detector casing that produce a steady amount of illumination. Since the selenium is light sensitive, this illumination creates a steady state amount of charge in the detector which helps to remove the ghosting effects, in essence "flushing" the detector. The amount of light produced by the LEDs is controlled by varying the percentage on time of the LED. The response of the detector to the LEDs is shown in figure 2.5. The plot shows the mean signal level recorded on the detector in a one second frame for various setting of the LED illumination. The plot shows that the detector responds linearly to the LED illumination, with an R^2 value for the line of 0.9996.

2.2.2 X-ray Tube

Next to the x-ray detector, the most critical part of the CT system is the x-ray

Figure 2.6. Oxford Instruments XTF5011 tungsten anode X-ray tube. Note the ruler with the scale in cm.

tube. The x-ray tube must have a small enough focal spot in order to be able to resolve fine details in the images while at the same time have a large enough output that the exposure can be acquired in a reasonable time. The tube must also have a high enough heat load capacity that multiple exposures can be acquired, as is required in CT data acquisition. The choice of x-ray tube is invariably a compromise between focal spot size and tube output.

The x-ray tube being used, shown in figure 2.6, is the XTF-5011 (Oxford Instruments, Scott's Valley, CA). This tube has a fixed tungsten anode, is capable of 50 kVp and a tube current of 1.5 mA. The nominal focal spot size as reported by the manufacturer is 70 μm. The fixed anode means that the tube has a lower heat load capacity, but also makes it much more compact than the larger rotating anode tubes. These large rotating anode x-ray tubes also have much larger power supplies, which would increase the size of gantry required for a dedicated mouse CT system. To compensate for the lower output of this x-ray tube, the distance from the source to the detector can be minimized and the exposure time can be increased. Since the target resolution for this system was 150 μm and the detector pixel size is 66 μm, there was no need to use a x-ray tube with a smaller focal spot since the resolution would still have been limited by the pixel size of the detector. A choice of x-ray tube with a smaller focal spot would have resulted in an even smaller x-ray flux. To keep the x-ray tube cool during continuous operation, a fan is placed directly below it to blow cool air over the tube. To monitor temperature, there is a type K thermocouple in the tube.
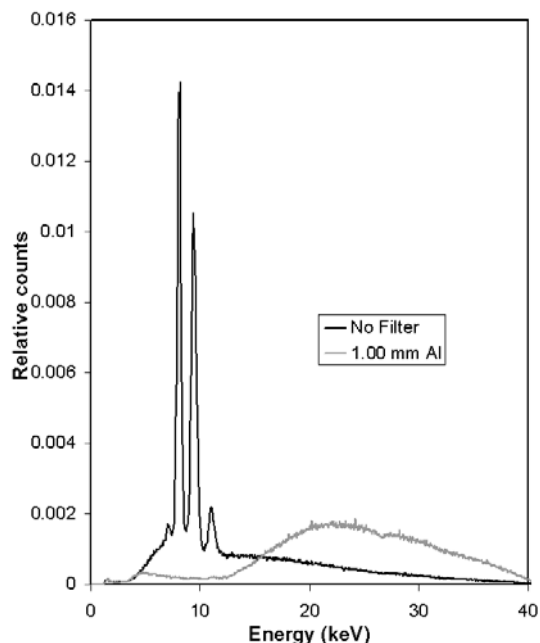
Figure 2.7. X-ray spectrum acquired using a single pixel CZT detector with no filtration and 1.0 mm Al filtration. The x-ray tube was operated at 40 kVp. The large peaks around 10 keV are the L fluorescence line of tungsten. Note the dramatic decrease in the fraction of low energy x-rays in the filtered beam. Both spectra have a total of 10^6 counts.

The x-ray tube is about 15 cm long and 8 cm in diameter. It weighs approximately 4 pounds. To allow for a greater choice in x-ray beam spectrum, a similar tube with a molybdenum anode was also obtained. This tube is the same model as the tungsten anode tube, with the only differences being a maximum tube current of 1.0 mA instead of 1.5 mA and a slightly larger focal spot of 125 μm × 240 μm. Both x-ray tubes have a thin beryllium window, which allows most low energy x-rays to pass through. A sample spectrum from the W anode tube is shown in figure 2.7. This spectrum was acquired using a 3 × 3 × 2 mm CZT detector (Amptek Inc., Bedford, MA) with the x-ray tube set at 50 kVp. The multi-channel analyzer (MCA) was calibrated using an Am-241 source. The dramatic peaks around 10 keV are the L fluorescence lines of tungsten.

The x-ray tube is powered by a Spellman PCM50P75X2779 (Spellman High Voltage, Hauppauge, NY) high voltage supply. This power supply powers both the high voltage and the tube current. To remotely control the power level, two voltages of between 0 and 10 volts are input for the kV and current respectively, where 0 V corresponds to the 0 power level and 10 V is maximum output (50 kVp or 1.5 mA). The power supply monitors the voltage and current and outputs this information as two 0-10 V voltages. The tube current is regulated through a feedback circuit in the high voltage line that detects the current and regulates the cathode current to adjust the tube current. This design creates a very stable x-ray exposure when the tube is continuously running. To control short exposures, a mechanical shutter is placed in front of the x-ray tube window. A diagram of this shutter is shown in figure 2.8. This shutter operates by sweeping from left to right on the first exposure and then right to left on the next
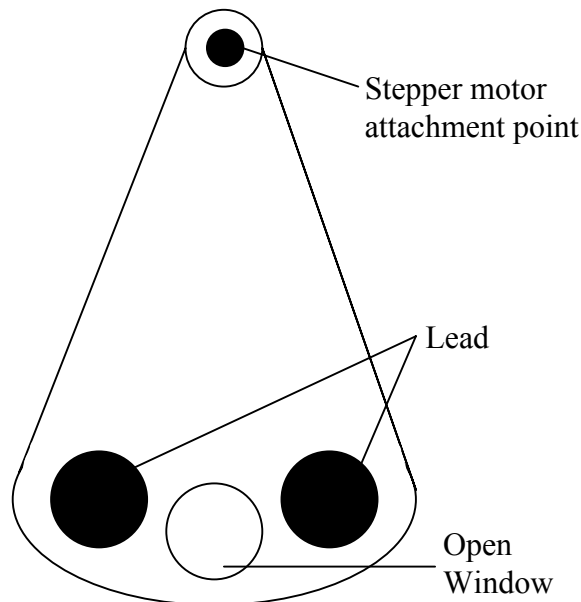
Figure 2.8. Diagram of the x-ray shutter. In one exposure the shutter sweeps from left to right. In the next exposure, the shutter sweeps the reverse direction.

34

Mean Signal Level Distribution
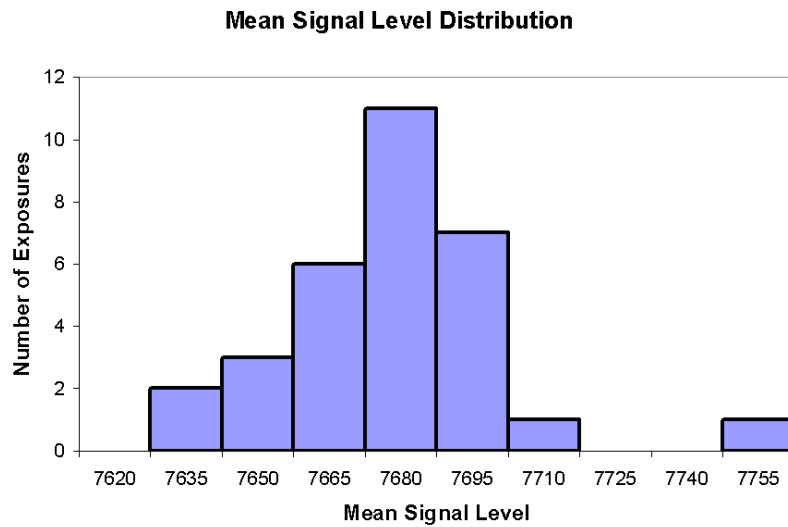
Figure 2.9. Histogram of the mean signal level on the a-Se detector from 31 consecutive exposures. The mean signal was 7669.5 ADU with a standard deviation of 23.2 ADU, or 0.3% of the mean.

Mean Signal Level vs. Exposure Time

$$y = 5245x - 100.43$$
$$R^2 = 0.9995$$
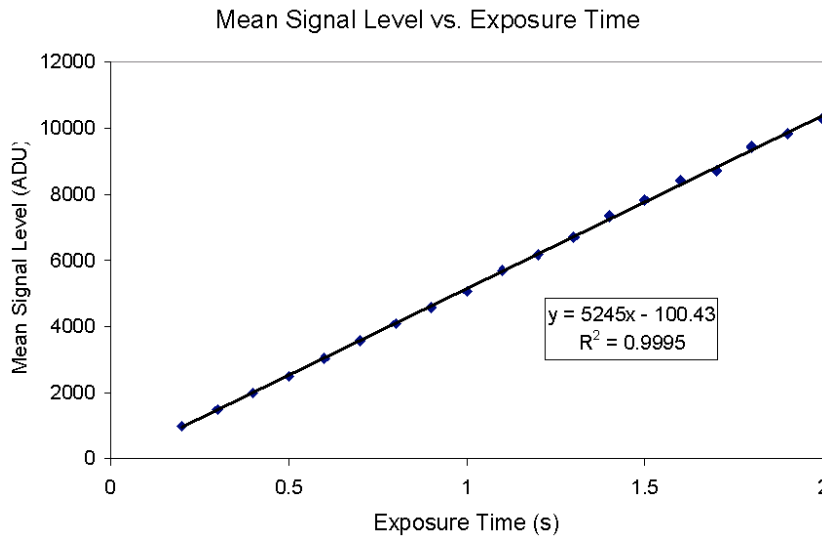
Figure 2.10. Plot of mean signal level on the a-Se detector vs. exposure time. Note the linear behaviour, with a R^2 value of 0.9995. Also note the non-zero intercept, which is due to the design of the shutter.

exposure. It is thought that such a shutter will give a more uniform exposure then a solenoid, which always opens in the same direction, thus always giving greater exposure to one side. One disadvantage to this shutter design is that there is some hysteresis in the

motion of the shutter owing to its dependence on a stepper motor. As a result of this, separate flat field corrections must be collected for both directions of the shutter motion.

This experimental setup creates a very stable exposure level as shown in figure 2.9. This histogram shows the mean signal level on the a-Se detector from 31 consecutive exposures, each 0.75 s in length with the tube set at 40 kVp and 500 μA. The mean signal level is 7669.5 analog to digital units (ADU) with a standard deviation of 23.2 ADU, or 0.3% of the mean. The response of the detector was very linear with exposure time as is shown in figure 2.10. These measurements were acquired by measuring the mean signal level on the a-Se detector with the x-ray tube set at 30 kVp and 500 μA, while varying the exposure time. The measurement for each exposure time was repeated four times. The detector response is linear with the exposure time with a R^2 value for the line of 0.9995. It is interesting to note that the intercept of the line is not 0, as might be expected, but is rather −100.4. This is due to the design of the shutter. The exposure time in all of these measurements refers to the time taken for the shutter to sweep from one position to the next. As can be seen from the shutter schematic in figure 2.8, this is not equal to the time that x-rays are passing through the shutter.

2.2.3   Motion Control Hardware

A National Instruments MID-6020 stepper motor power supply (National Instruments, Austin, TX) controlled by a PCI-7624 stepper motor PC-based control card (National Instruments) drives two stepper motors. The first stepper is placed above the x-ray tube window and controls the motion of the shutter assembly. The second stepper

motor is attached to a Velmex B5990TS (Velmex, Inc., Bloomfield, NY) rotation stage. This stage is used to rotate the specimen being imaged in a CT scan.

2.2.4 Optical Breadboard

The entire experimental setup in mounted on an optical breadboard (Melles Griot, Carlsbad, CA). This breadboard measures 2' × 4' × 4" thick and has holes laid out on a regular grid of 1" centres. The breadboard holds the components rigidly, absorbs vibrations, and also allows for easy alignment of the components.
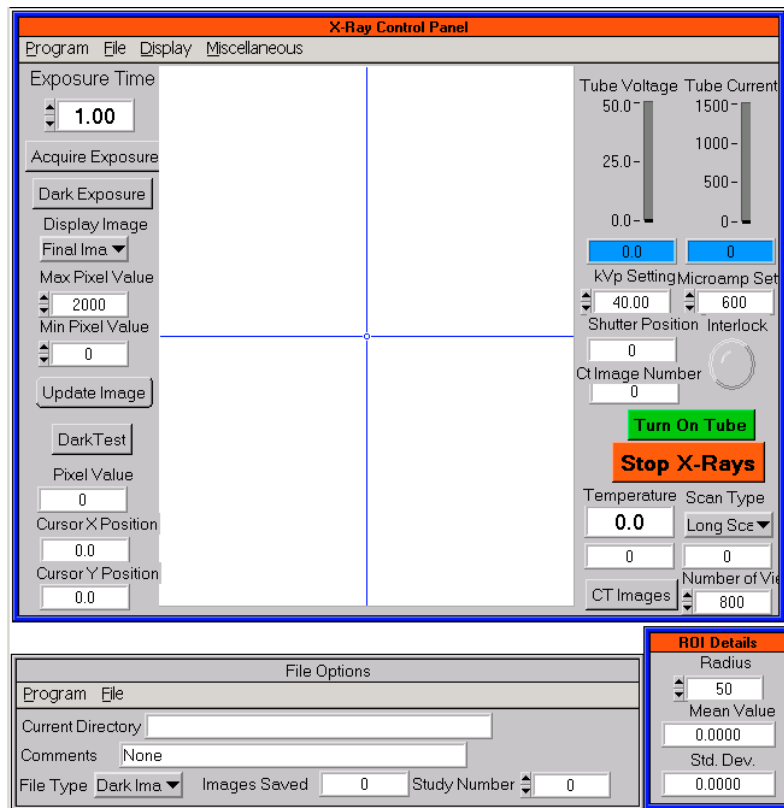
Figure 2.11. Screenshot of data acquisition control program.

2.2.5   Data Acquisition System

The PC (Optiplex Gx1p, Dell Computers Inc., Round Rock, TX) contains an Intel Pentium III processor (Intel Corp., Santa Clara, CA) operating at 600 MHz and is running Windows NT 4.0 (Microsoft Corp., Redmond, WA). The system contains an 18 gigabyte SCSI hard-drive for data collection, a 60 gigabyte IDE hard-drive for data storage, and 512 megabytes of RAM.

The PC interfaces to the x-ray hardware via a PCI-MIO16-E4 analog input/output card. This card supplies the 0-10V control voltages for the tube current and voltage, monitors the tube current and voltage information supplied by the x-ray tube power supply, and monitors x-ray tube temperature.

The data acquisition software is written in LabWindows/CVI 5.0 (National Instruments, Austin, TX). This is a C based programming language with extensive
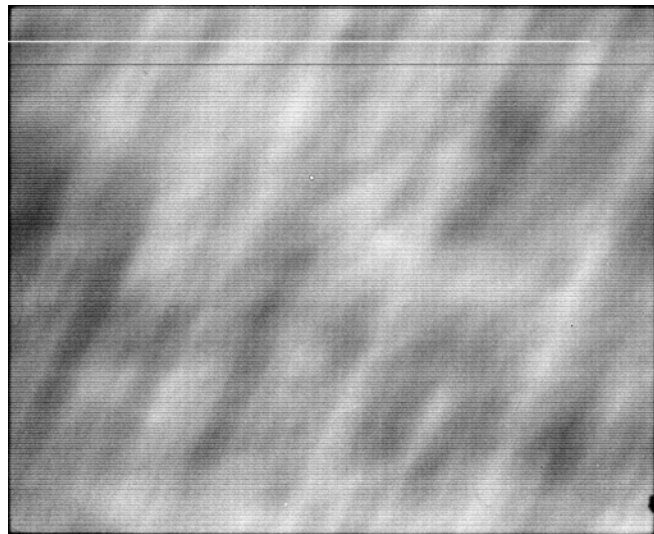
Figure 2.12. A sample dark frame from the a-Se detector. Note the two column defects near the top of the detector. The "clouding" is due to variations in the selenium layer while the regular pattern of horizontal rows are due to the slightly different response of the eight AD converters used in the readout.

libraries for creating graphical user interfaces (GUIs). A screen image of the control program is shown in figure 2.11.

2.3 X-ray Image Acquisition

2.3.1   Image Acquisition Process

To obtain an x-ray image, two frames must be acquired. The first is the dark frame. This is an image of equal time as the exposure image that is subtracted from the exposure image. It allows for correction of the dark current present in the detector. The second frame is the white, or exposure frame. This is the actual exposure. Both frames are stored on the onboard RAM and downloaded to the PC once both frames are complete. An example of dark and white frames are shown in figures 2.12 and 2.13

Figure 2.13. A raw exposure image. Note the detective columns and the non-uniformity wherein the image is brighter at the bottom than at the top.

respectively. These images are images of a mouse acquired with the x-ray tube set at 40 kVp and 675 µA, with a 1 s exposure time. In the dark frame image the defective columns can be seen near the top of the image. The general "clouding" in the image is due to the varying sensitivity of the selenium while the regular horizontal rows are due to the slightly different response of the eight AD converters used in the readout. In the white image the defective columns can be seen as well as a non-uniformity where the image is brighter at the bottom than at the top. The regular pattern due to the eight parallel digitizers is still apparent in the white image.

2.3.2   Corrections Applied to the X-ray Image

The corrections described in this section are applied in the order they are
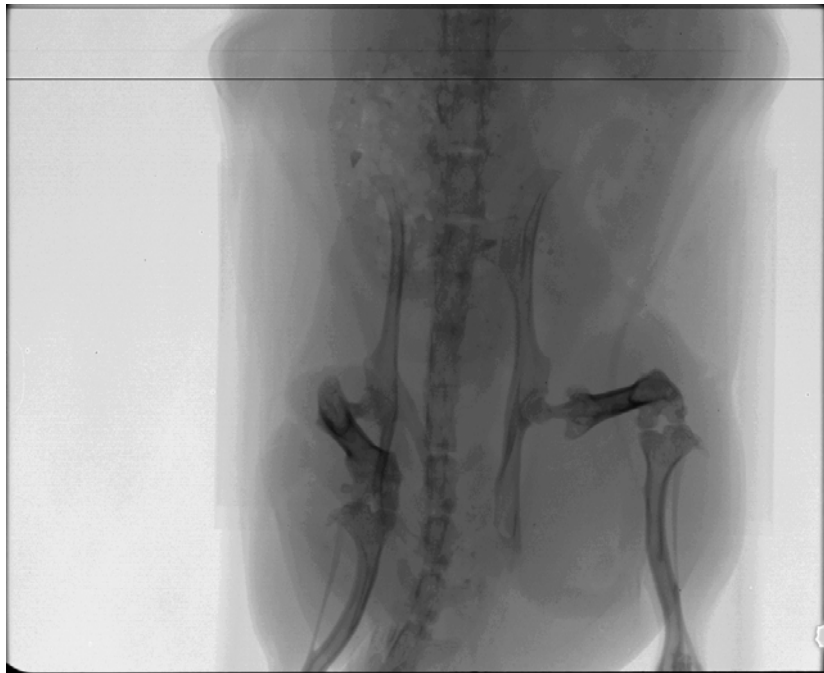
Figure 2.14. The dark-subtracted image. Note that the majority of the artefacts created by the eight parallel digitizers have been removed.

described.

a) Dark Frame Subtraction

The dark frame is subtracted from the white frame to correct for the detector dark current. The result is the dark-subtracted image. An example of a dark-subtracted is shown in figure 2.14. This image is the result of subtracted the dark frame in figure 2.12 from the white frame in figure 2.13. The dark-subtracted image shows that the majority of the horizontal lines created by the eight parallel digitizers have been removed. While one would expect that the effect of the digitizers should simply be a multiplicative factor, each digitizer has its own zero offset which the dark field correction also corrects for.

b) Flat Field Correction

The dark-subtracted image is multiplied by a sensitivity correction map, also known as a flat field correction. This correction map is created by averaging multiple exposures (usually 10) acquired without any attenuator in the field of view. This process corrects for regions of varying sensitivity on the detector, caused by such factors as varying thickness of the selenium layer, varying window thickness, x-ray beam non-uniformity, digitizer gain variations, and geometrical factors such as the $1 / r^2$ factor at the edge of the frame.

c) Defective Pixel Correction

When the detector was first delivered, a map of the defective pixels on the sensor was created. A defective pixel is defined as one where the response of the pixel is more than 25% different from the global response. Usually the defective pixels will either be "dead", meaning there is no charge collected in them, or they will be "hot", and always give a maximum reading. There are also a few defective pixels falling between these two extremes, with most of these pixels being at the edge of the sensor where the selenium thickness changes rapidly. The correction is performed by replacing the value in defective pixels with a value equal to the nearest neighbour average. An example of the flat-fielded, defective pixel corrected image is shown in figure 2.15. This image shows the uniformity improvement due to the flat-field correction and the defective column
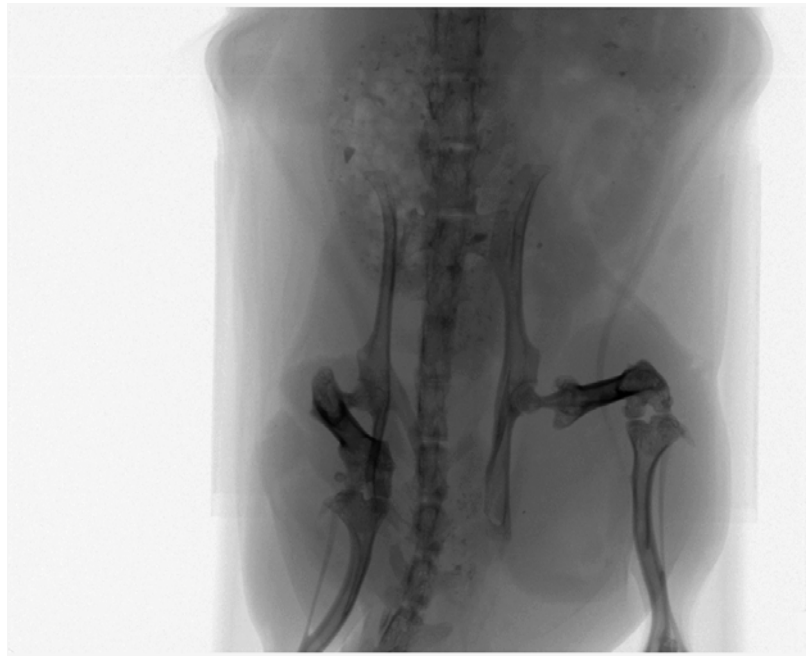
Figure 2.15. The flat-fielded, defective pixel corrected image. Note the uniform exposure level from top to bottom and the absence of the defective columns.

removal by the defective pixel correction.

2.4 CT Image Reconstruction

To properly reconstruct CT images, the geometric parameters must be very accurately known. If the geometry used in the reconstruction is inaccurate, artefacts will be seen in the reconstructed data sets. Measuring the geometry parameters can be both tedious and difficult, since the exact location of the centre of rotation and the focal spot of the x-ray tube are difficult to determine. To solve this problem, a technique has been developed that utilizes a scan of a wire of diameter 250 μm. The CT data is rebinned from cone-beam data into 2D "sinograms", where each sinogram is the response from one row of the detector for all angles. This data is similar to the data acquired from a conventional fan-beam CT scanner. An example of such a 2D sinogram is shown in figure 2.16.
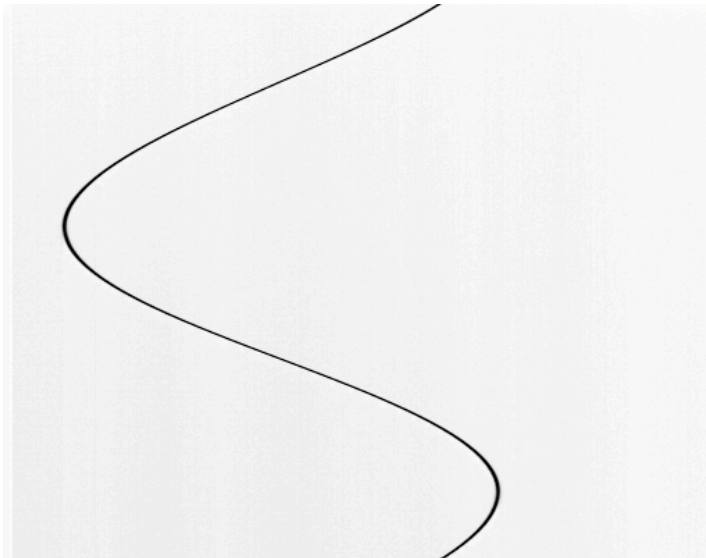
Figure 2.16. A 2D "sinogram" of the x-ray data for a 250 μm wire.
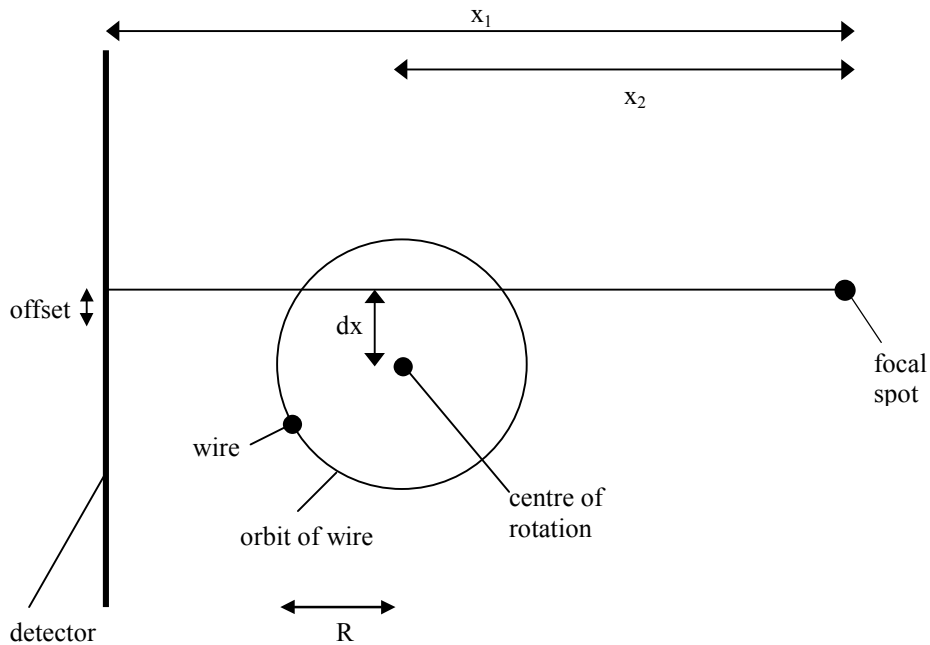
Figure 2.17. Schematic of geometry parameters for the image reconstruction.

A computer simulation was written that computes the 2D sinogram of the wire using 7 parameters, as shown in figure 2.17. These parameters are:

1) x_1, the distance from the focal spot to the detector along a normal to the detector.

2) x_2, the distance from the focal spot to the x position of the centre of rotation.

3) dx, the horizontal distance from the centre of rotation to the line normal to the detector passing through the focal spot.

4) offset, the number of pixels on the detector from the centre of the detector (pixel 512) to the line normal to the detector passing through the focal spot.

5) R, the radius of the orbit of the wire.

6) dz (not shown in plot), the vertical position of the line normal to the detector passing through the focal spot.

Figure 2.18. A subtraction of a simulated sinogram from a measured sinogram.

7) γ, the angular offset between the simulated and real data.

Allowing all 7 parameters to vary independently produces multiple possible solutions since there is a dependency among the parameters. In order to get around this problem, the distance x_1 is measured and then fixed in the program. The choice of fixing x_1 was based on the fact that of all the parameters, this one was the easiest to measure. If the measurement of x_1 is incorrect, the geometry finding routine will still converge, although the values will be inaccurate. The images reconstructed using the incorrect parameters will be free of visible artefacts, however the pixel size will be inaccurate (i.e. the reconstructed image will be minified or magnified). Thus a possible correction for this problem is to image an object of known dimensions and use the known dimensions to determine the pixel size of the reconstructed image.

A CT data set is simulated using a first guess of the geometry parameters of the system. The difference between the real and simulated data is measured and the simulation repeats after updating the geometry parameters. The minimization process used is the downhill simplex method in multidimensions, implemented using the AMOEBA routine [Press et al., 1989]. This process continues until the difference between the simulated and real data sets converges to a minimum. The cost function used measures the position of the centre of the wire in each line of the sinogram. The cost is the sum of the square differences of the position of the centre of the wire between the simulated and real data. An example of a simulated sinogram subtracted from a real sinogram is shown in figure 2.18. To verify the geometry parameters, the wire data is reconstructed to see if a point object results as shown in figure 2.19.

To determine if the geometry finding routine would give reproducible results, a wire was scanned 13 separate times, each time using a 400 view study. In between each study, the wire was removed and then replaced on the rotation table. This was done so that the parameters for R and γ would be different for each parameter solution. The distance x_1 was fixed at 180 mm. Table 2.1 shows the parameter results for each of the 13 studies. The values for R and γ are not tabulated since they are different for each scan based on the initial placement of the wire. It can be seen that the routine very consistently predicts the values of offset and dx, while there is greater variation in the other parameters. Regardless of the differences, all of the parameter sets produced acceptable results when used to determine the geometry for the reconstruction process.

Scan #	x_1 (mm)	x_2 (mm)	Offset (pixels)	dx (mm)	dz (pixels)
1	180.0	281.468	420.369	0.373	42.2
2	180.0	280.940	420.089	0.398	36.7
3	180.0	284.431	420.178	0.386	38.3
4	180.0	285.526	420.402	0.380	35.7
5	180.0	282.620	419.729	0.396	42.2
6	180.0	283.691	419.690	0.402	39.2
7	180.0	279.163	419.914	0.386	36.5
8	180.0	282.544	420.003	0.392	45.1
9	180.0	281.523	420.475	0.362	40.9
10	180.0	281.523	420.060	0.389	49.8
11	180.0	278.193	419.463	0.422	39.0
12	180.0	283.298	419.277	0.412	47.2
13	180.0	277.036	419.276	0.437	40.5

Table 2.1 Results of the geometry parameter finding routine for 13 separate calibration scans.
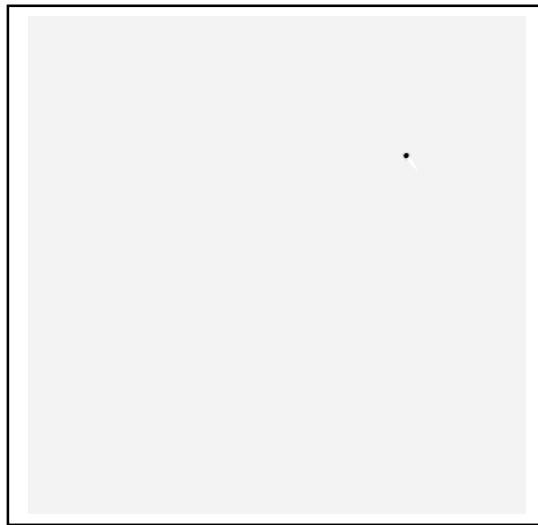
Figure 2.19. Reconstructed image of the wire shown in the sinogram in figure 2.15.

Once the geometry has been determined, the data is reconstructed using the Feldkamp-Davis-Kress (FDK) cone-beam reconstruction algorithm [Feldkamp et al., 1984]. The implementation of the reconstruction algorithm is from the group of Dr.
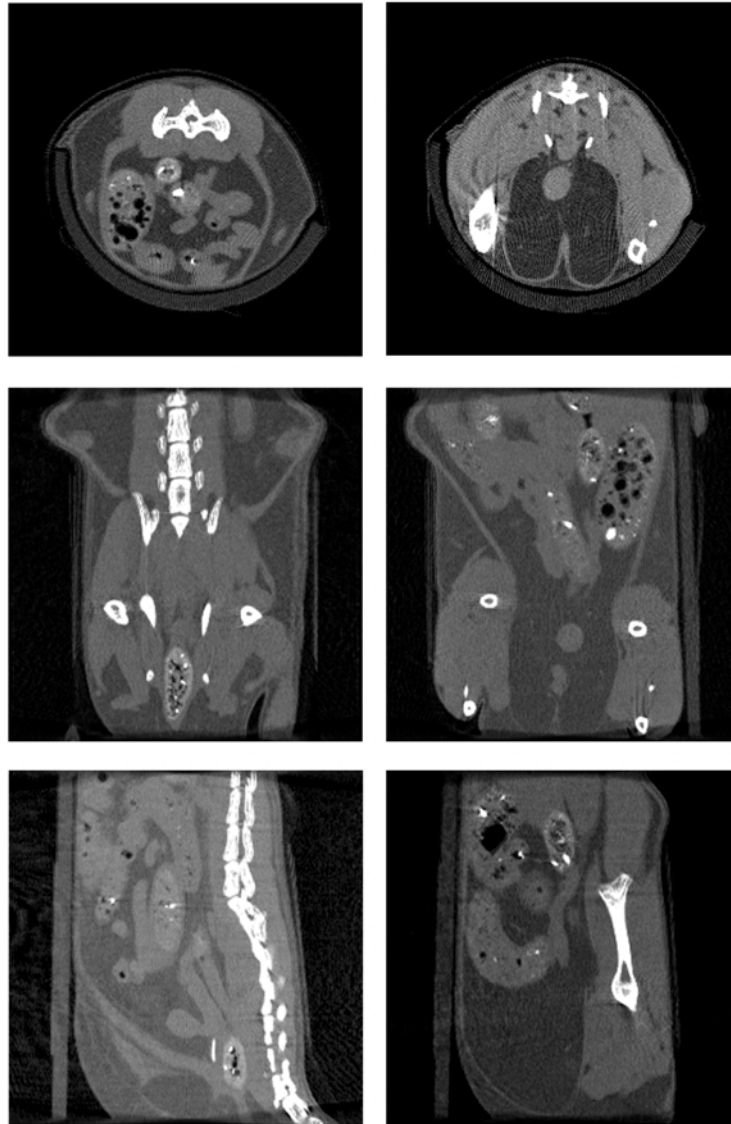
Figure 2.20. Reconstructed images of a mouse from data acquired on the bench-top CT system. The top row are transverse slices, the middle row coronal slices, and the bottom row sagittal slices. The data was acquired using 400 projections with the x-ray tube set at 40 kVp and 675 μA and 1 s exposure time.

Michel Defrise. Typical reconstruction parameters are a $256 \times 256 \times 256$ matrix with a voxel size of 150 μm^3. A set of sample reconstructed images is shown in figure 2.20. These images were reconstructed from data acquired with 400 projections. The x-ray tube was set at 40 kVp and 675 μA with a 1 s exposure time.

2.5 Choice of CT System Operating Parameters

There are many practical considerations involved in determining the operating parameters of the CT system. A prime example of this is in the choice of exposure time. Since a mechanical shutter attached to a stepper motor was used to control the x-ray beam, each flat field correction image was valid for only one choice of exposure time. This was because the exact motion of the shutter was slightly different for each choice of exposure time. For this reason, it was arbitrarily decided that a 1 s exposure time would be used wherever possible for acquisition. The choice of the other operating parameters is a combination of hardware considerations as well as considerations of radiation dose to a mouse being scanned. This issue of dose will be dealt with further in chapter 4.

2.5.1   Number of Views Per Scan

The number of views for a typical scan was decided based initially on the target time for a scan. Consider that with a 1 s exposure time, the time needed per frame due to the combination of exposure, readout, and motion of the rotation stage is approximately 2.25 s. This means that for a 15 minute scan, 400 views can be acquired. When a mouse was imaged with this many views, the reconstructed images were found to be adequately free of sampling artefacts.

Upper and lower limits for the number of views to use were not thoroughly examined. Certainly less than 400 views can be used, since studies using only 200 views were found to give acceptable images (e.g. see figures 5.4 and 5.6). In theory the upper

limit for the number of views is determined by the data storage space the data acquisition computer has available.

2.5.2 X-ray Tube Settings

The choice of kVp for a CT scan is a multivariable problem. A partial list of factors that vary with x-ray tube kVp include tube output, response of the detector, contrast of objects being imaged, dose deposition in the object being imaged, and beam hardening artefacts in the reconstructed image. In addition to the choice of kVp, adding a x-ray beam filter will dramatically change the characteristics of the beam. There are quite possibly many operating points that work equally well for imaging a mouse. In order to study some of the tradeoffs in the choice of kVp and filter, four representative operating points were chosen and investigated in greater depth. These choices for x-ray spectra are tabulated in table 2.2 and the spectra as measured by the single pixel CZT detector are shown in figure 2.21.

Beam	Anode	kVp	Filter (in mm)	Tube Current (mA)	Exp. Time (s)
A	Mo	30	0.02Mo + 0.5Al	1.0	2.0
B	Mo	40	0.02Mo + 0.5Al	0.8	1.0
C	W	40	1.0Al	0.6	1.0
D	W	40	2.0Al	1.2	1.0

Table 2.2. Information about each of the four spectra used in the measurements and the labels for each.

Two mice were imaged using these four spectra, one for the W anode spectra and the second mouse for the Mo anode spectra. Each acquisition consisted of 400 views over a full circle orbit. To account for the different x-ray beam fluxes due to the different
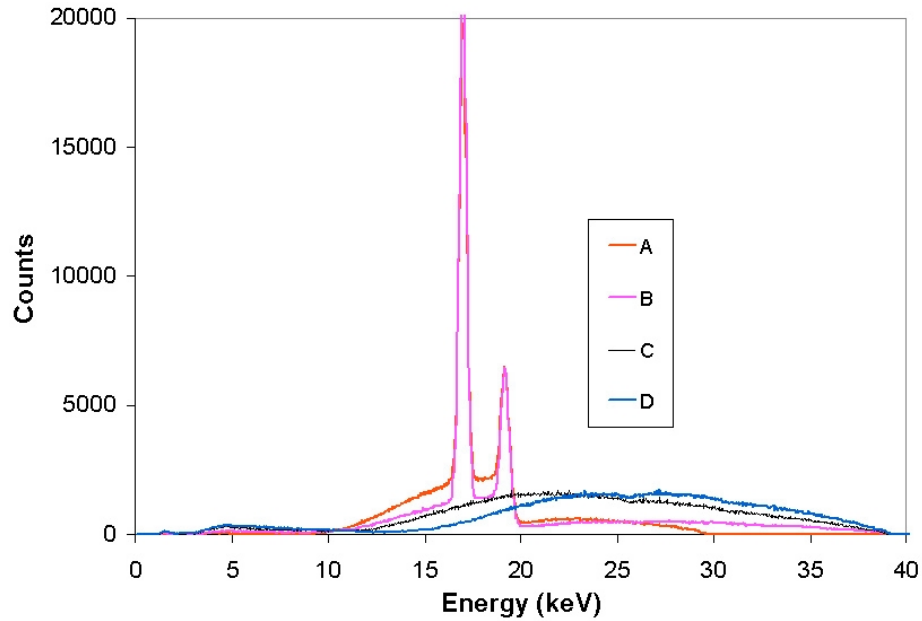
Figure 2.21. Energy spectra of the four x-ray beams used. Information about each beam is given in table 2.2. The plots are scaled so that each spectrum has the same number of total counts.
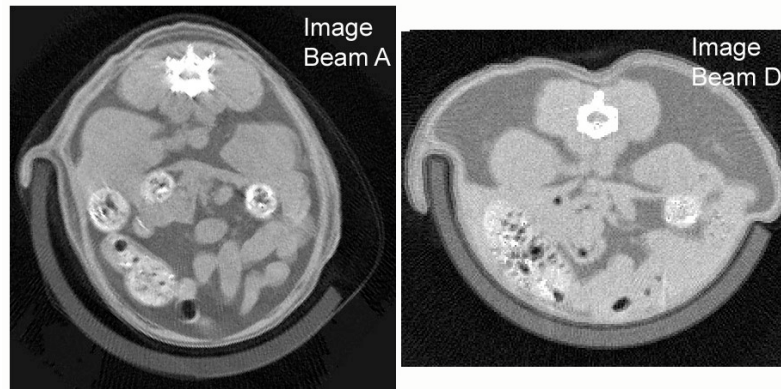
Figure 2.22. Reconstructed images for beam A and beam D.

filtering, the tube current was varied so that the mean signal level produced on the detector in an unattenuated area was comparable for all four data sets.

Figure 2.22 shows reconstructed images from the softest beam (A) and hardest beam (D). Table 2.3 lists the reconstructed attenuation value for various tissues in the mouse as well as the ratio between various tissues.

51

Beam	Bone	Fat	Kidney	Muscle (near skin)	Muscle (near centre)	Testicle
A	$\mu=2.290$	$\mu=0.481$	$\mu=0.776$	$\mu=0.824$	$\mu=0.777$	$\mu=0.448$
B	$\mu=2.106$	$\mu=0.3753$	$\mu=0.576$	$\mu=0.632$	$\mu=0.585$	$\mu=0.358$
C	$\mu=1.678$	$\mu=0.255$	$\mu=0.409$	$\mu=0.439$	$\mu=0.412$	$\mu=0.257$
D	$\mu=1.285$	$\mu=0.229$	$\mu=0.354$	$\mu=0.376$	$\mu=0.352$	$\mu=0.225$

Table 2.3. Attenuation values (μ in cm^{-1}) for various locations in the mouse for each spectrum used.

As expected, the attenuation values decrease as the input spectrum increases in energy, however the ratio between the attenuation values for different tissues does not change greatly (with the exception of bone). Another factor to note is the amount of beam hardening artefacts observed. Since x-ray beams are polyenergetic, as it passes through an attenuator the lower energy photons will be preferentially removed and the mean energy of the beam will increase. In the reconstructed images, this will show up as a difference in attenuation values from the centre of the object out towards the edge. In the mouse images, this is demonstrated by the attenuation values for muscle near the edge of the mouse and near the centre. The Mo anode beams show a larger difference between these two attenuation values than do the harder W anode beams. The results suggest that little contrast is lost by using a harder x-ray beam, while the dose to the mouse is reduced approximately 35%. The issue of dose from these different beams will be addressed in chapter 4.

For routine operation of the CT system, an operating voltage of 40 kVp was chosen with a beam filtration of 1.0 mm Al. The results suggest that a filtration of 2 mm Al would also have been adequate, however the x-ray tube current must be turned up to account for the loss of x-ray flux from the increased filtration. The x-ray tube current

was chosen so that the signal seen on the x-ray detector was at approximately half its dynamic range. For a tube setting of 40 kVp and 1.0 mm Al filtration, this means a tube current of approximately 600 μA while for a 40 kVp beam with 2.0 mm Al filtration, the current needed was 1200 μA. In this case practical issues must again be considered since the x-ray tube does not have unlimited heat loading capacity, and 1200 μA at 40 kVp produces a x-ray tube temperature that is very close to the maximum recommended. Thus the lower filtration level and corresponding lower tube current was chosen in order to avoid causing damage to the x-ray tube. For the setting of 40 kVp, 1.0 mm Al filtration, and 600 μA, the exposure incident on the detector is 26 mR.

2.6 Limitations of Current CT System

This CT system was designed to be a flexible bench-top prototype for optimizing the data acquisition process, and was successful in that regard. However, as a consequence of this design, there is an inherent difficulty in the routine imaging of mice. This difficulty is caused primarily by the vertical placement of the mouse. Once the mouse has been secured to the bed, the only way to adjust the region of the mouse being imaged is to take it off the bed and re-secure it at a new height. This difficulty in placing the mouse also makes it difficult to do longitudinal studies of one animal. Since the detector is of a limited size, only half of the mouse can be imaged at one time, making whole body imaging an arduous task. The design of the shutter requires that there be two flat field correction images, adding an extra layer of complexity to the image processing of the system and doubling the calibration time of the system.

The reconstructed resolution limit of the CT system was not measured due in large part to the lack of an appropriate method to measure it. In human CT systems, the resolution is measured by imaging a high contrast phantom consisting of closely spaced holes in an acrylic phantom. This method is not applicable for a microCT system due to the difficulty of constructing a phantom with closely spaced holes of diameter < 100 μm. The method described by Boone [Boone, 2001] of measuring the pre-sampled MTF in the reconstructed image by using a metal foil was attempted. This method was unsuccessful however, because the beam-hardening artefacts along the length of the foil interfered with the line spread function in the reconstructed image. The absolute signal to noise ratio and contrast of the system were not measured due to the lack of an agreed upon method of performing this measurement. There are currently no standard phantoms in existence for evaluating these parameters of a microCT system.

The reconstructed data was always displayed as μ values measured in 1/mm. The data was not converted to Hounsfield units (HU), as is typically done in human CT, due to the lack of calibration factors for the system. Determining such calibration factors was difficult since the system was in a constant state of change, which would have required constant recalibration. Converting the data to HU would have been advantageous since HUs range from 0 to 4095 (12 bit numbers) whereas the μ values were 32 bit floating point numbers. Thus the conversion would have represented an immediate factor of two compression in the data.

Chapter 3. A Comparison of X-ray Detectors for Mouse Imaging

3.1 Introduction

Most commercially available mouse x-ray CT scanners utilize a charge coupled device (CCD) detector coupled via fibre optic taper to a phosphor screen. However, little research has been done to determine if this is in fact the optimum detector for the task of mouse imaging. Instead, much of the evaluation of these CCD cameras, and other digital x-ray detectors, have focused around the task of digital mammography [e.g. Vedantham et al., 2000; Andre et al., 1998; Karellas et al., 1992]. The requirements for small animal CT imaging are however quite different from the requirements for digital mammography, thus the detectors need to be evaluated from a different point of view. In digital mammography, four exposures are made of each patient, with a minute or so interval between each exposure and a 10-15 minute interval between patients. In CT acquisition mode, several hundred exposures are made within a 15 minute time frame. Thus issues such as image lag are not nearly as important in digital mammography. Another factor that differs between small animal CT and mammography is the x-ray beam used. In digital mammography, a Mo anode x-ray tube is used, with an applied voltage of 24-28 kVp typically used [Bushberg et al., 1994]. In mouse CT, a W anode tube is typically used and set at around 40 kVp [Paulus et al, 1999; Chow et al, 2001; Corrigan et al, 1999]. As a result, it is not clear how the performance measurements made with the Mo anode tube will compare to those made with a W anode tube. The field of specimen imaging has also made use of some of these digital detectors, primarily CCD cameras [e.g. Ruegseggar et al., 1996]. Specimen scanners also differ in their detector

requirements from mouse scanners. The primary difference is that radiation dose to a specimen is not a concern since it is not a living system. Thus unlimited imaging time can be used to obtain very high resolution (e.g. 8 μm resolution reported by Ruegseggar et al.). To obtain this high resolution a CCD camera is used, but with a much greater amount of geometric magnification than would be seen in a mouse system. This magnification requires that a higher x-ray flux and/or longer imaging time be used in order to get a reasonable signal level on the detector due to the increased source-detector distance. Because of the application, resolution is of utmost importance, and little consideration is given to sensitivity of the detector.

For the reasons discussed above, an evaluation of three different types of digital x-ray detectors has been conducted using x-ray beam parameters typically used for mouse imaging.

3.2 Materials

3.2.1   Description of Detectors

Three different x-ray detectors were evaluated for this study. The first is the direct a-Se detector described in section 2.2.1. The second detector, an indirect detector, is an amorphous silicon (a-Si) High Optical Fill Factor Array (HOFFA) (Palo Alto Research Center, Palo Alto, CA) [Rahn et al., 1999] flat panel detector directly coupled to a minR gadolinium oxysulfide (GOS) scintillator screen (34 mg/cm^2) (Eastman Kodak Company, Rochester, NY). The minR screen was chosen because of its good resolution relative to thicker screens. The HOFFA array is a 512×512 array of 75 μm pixels,
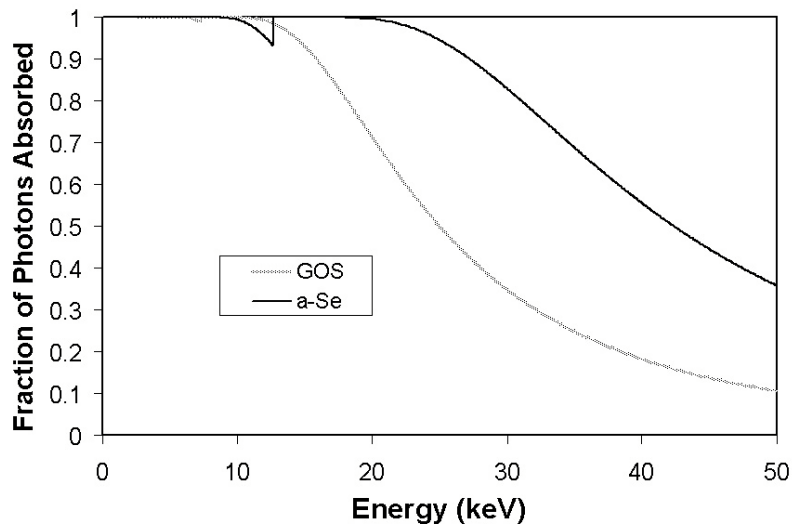
Figure 3.1. Plot of the fraction of photons absorbed vs. photon energy for the 250 μm a-Se layer and the 34 mg/cm^2 GOS screen.

giving an active area of 3.84 cm by 3.84 cm. The third detector, also an indirect detector, is a CCD camera manufactured by Dalsa-MedOptics (Dalsa Life Sciences, Tucson, AZ) based on the Kodak KAF-1000 sensor, coupled via a nominal 3:1 reducing fibre optic taper to a minR GOS scintillator screen. The effective pixel size is 67.55 μm, giving an active area of 6.9 cm by 6.9 cm. Figure 3.1 shows the fraction of photons absorbed as a function of photon energy for the 34 mg/cm^2 GOS screen and the 250 μm layer of a-Se.

3.2.2 X-ray Tube

The x-ray tube used for these experiments is the Oxford Instruments XTF-5011 described in section 2.2.2 For the purpose of evaluating the detectors, the x-ray tube was run at 40 kVp with either 0.5 mm Al or 1.0 mm Al added filtration.

3.3 Methods

3.3.1 Corrections to Images

Since all digital x-ray detectors have inherent dark signal levels and non-uniformities in signal level, each exposure frame needs to be corrected. The process for correcting each image is to subtract a dark current frame, and then normalize the signal level using a pixel sensitivity map. After normalizing the image, a defective pixel correction is applied using a nearest neighbour interpolation method. For the CCD and a-Si detectors, each dark frame was the average of 10 dark frames. For the a-Se detector, the dark frame used was from one measurement of the dark current only. For all the detectors, the flat field correction applied was the average of 10 exposure frames.

3.3.2 X-ray Spectrum Measurement

The x-ray spectrum was measured using a $3 \times 3 \times 2$ mm^3 single pixel cadmium-zinc-telluride (CZT) detector (Amptek Inc, Bedford, MA). The detector was placed approximately 20 cm from the x-ray tube window. Two tungsten collimators, separated by approximately 5 cm, were used to reduce the count rate to several thousand events per second. This low count rate was required to avoid pulse pile-up issues in the CZT detector, which had a relatively long pulse shaping time of 6 μs. The front collimator was 100 μm in diameter and the back collimator was 400 μm in diameter. The measurement of the spectra was complicated by the addition of a low energy tail created by the escape of a fluorescence x-ray generated by a photoelectric interaction of the incident x-ray in the CZT. Since these spectra were to be used to estimate photon

fluence, this low energy tail was unacceptable as it did not reflect the actual spectrum coming out of the x-ray tube. To address this problem, a x-ray spectrum was measured with no filter in place, and then this measured spectrum was used as the input for an analytical simulation where a beam filter could be added. Due to the large attenuation value of aluminum at low energies relative to high energies, this method effectively removed any of the low energy tails due to the escape of the fluorescence x-rays.

3.3.3   Photon Fluence Measurement

The value of the photon fluence per unit exposure, q, in photons/mm^2/mR must be known in order to calculate the detective quantum efficiency (DQE(f)). The value of q was calculated by measuring the exposure per frame using a Keithley 35050A dosimeter equipped with a model 96035B ion chamber (Keithley, Cleveland, OH). The spectrum calculated as described in section 3.3.2 was then used, along with a table of mR/photon as a function of energy to calculate the average mR/photon for a given spectrum. The exposure measured with the ion chamber was divided by the average mR/photon value to come up with a measure of photons/mm^2/mR.

3.3.4   Detector Stability

In x-ray CT it is important that the response of the detector to a given exposure level be consistent throughout the scan. To test this stability, each detector was exposed to a series of 30 mR exposures with the x-ray tube set at 40 kVp and 1.0 mm Al filtration,

and the mean signal level was measured on the detector as a function of exposure number.

3.3.5   Modulation Transfer Function

The modulation transfer function (MTF(f)) was measured using the method of Fujita et al. [Fujita et al., 1992]. In this method, an image of a 10 μm slit, tilted at a small angle to the vertical, is acquired. The slit was placed directly on the cover of the detectors, and positioned so that the perpendicular ray from the source to the detector passed through the centre of the slit. Due to the angle of the slit, each row across the slit represents a slightly difference sampling phase of the slit, as shown in figure 3.2. As shown in the diagram, the response of each row varies as the position of the slit relative to the pixel centers changes. To create the finely sampled line spread function the number of rows that correspond to the slit shifting over one column must be known. To
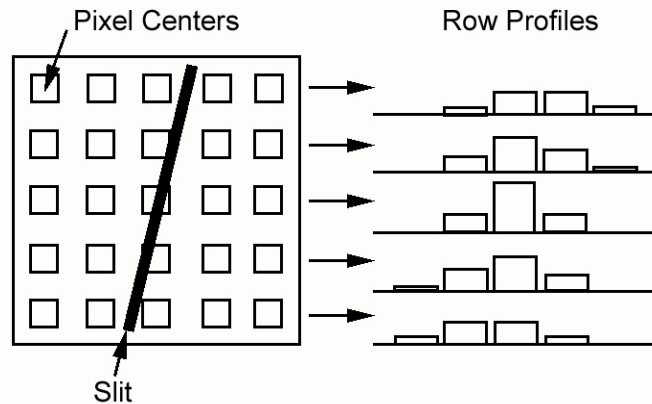
Figure 3.2. Diagram showing the angle of the slit on the detector and the resulting sampling pattern in the pixels under the slit. Note that for this example, a total of five rows would be used to create the finely sampled line spread function.

determine this number the maximum value of each row is plotted vs. row number. An example of this is shown in figure 3.3. In the example plot, there are 23 rows between successive minima in the profile. This means that 23 rows would be used to synthesize the finely sampled line spread function (LSF), with a spacing of 1/23 of the pixel pitch between each sample point. To normalize for each row response, the integral of the pixel values along each row is taken and used to normalize the value of each pixel in that row.

Once the finely sampled LSF is obtained, the MTF(f) is calculated by taking the Fourier transform of the LSF. The MTF(f) curve is then corrected for the finite width of the 10 μm slit by dividing by a sinc function. Since the MTF(f) curve must be used in the calculation of the DQE(f), and the MTF(f) is sampled at frequency points that need not coincide with values sampled in the noise power spectrum, the MTF(f) curve is fit with a 4th order polynomial. This polynomial fit is then used to calculate the MTF(f) for use in
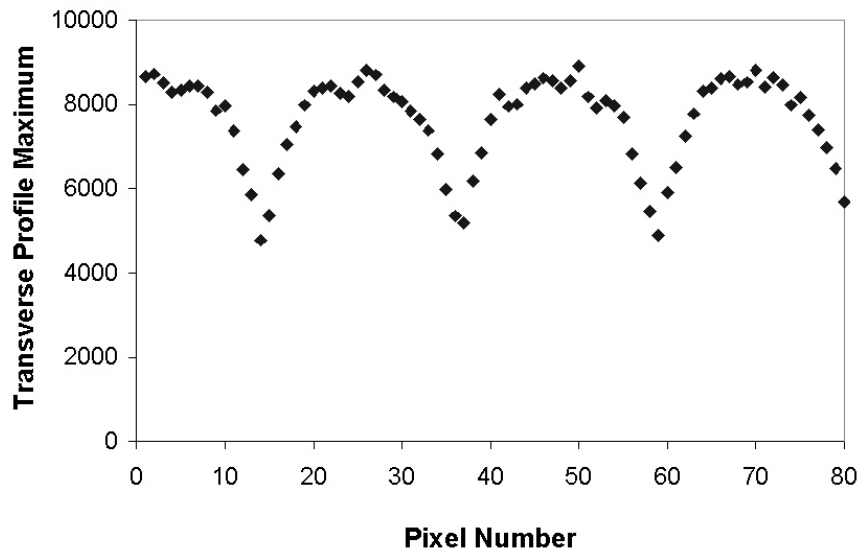
Figure 3.3. Plot of transverse profile maximum along the slit. The minima correspond to the point where the slit is exactly between two pixel centers. In this example, 23 rows would be used to synthesize the finely sampled LSF, since there are 23 rows between successive minima in the plot.

calculating DQE(f).

3.3.6 Noise Power Spectrum

The normalized noise power spectrum (NPS(f)) is essentially a measure of the variance as a function of frequency. The NPS(f) for each detector was measured by averaging the NPS(f) from 100 exposure frames. The NPS(f) of an individual frame is calculated by taking a central portion of the image (a 512×512 area for the CCD and a-Se detector and a 256×256 area for the a-Si detector) and then calculating the 2-D NPS as

$$NPS(u,v) = \frac{|FT(u,v)|^2}{(Mean\ signal)^2} N_x \Delta_x N_y \Delta_y \qquad \text{(Eq. 3.1)}$$

The NPS(u,v) for each frame is then averaged to create a 2-D NPS image. To calculate the 1-D NPS(f) needed for the calculation of DQE(f), a method similar to that described by Dobbins et al. is used [Dobbins et al., 1995]. A 1-D slice is taken through the 2-D image adjacent to the axes of the image, and the frequency represented by a given pixel is determined as $(u^2 + v^2)^{1/2}$. A total of 10 lines (5 on either side of the central axis) are averaged in this way to calculate the 1-D NPS(f).

The NPS(f) was measured at 40 kVp with a filtration level of 1.0 mm Al and 0.5 mm Al. For the a-Se detector, exposure levels per frame of 30 mR, 3 mR, and 0.3 mR were used for both x-ray beam settings. For the a-Si detector, exposure levels per frame used were 30 mR and 3 mR for the 40 kVp, 1.0 mm Al beam and 30 mR for the 40 kVp, 0.5 mm Al beam. For the CCD detector, exposure levels of 30 mR and 3 mR were used

for both x-ray beam settings. It should be noted that in order to get a reliable low exposure level (i.e. 0.3 mR/frame), the x-ray tube was set to a level of higher output, and the distance between the x-ray tube and detector was increased. For the a-Si and the CCD detectors, the distance between source and detector were fixed due to mechanical constraints and thus the low exposure level NPS(f) could not be measured.

3.3.7   Detective Quantum Efficiency

DQE(f) is a measure that relates the statistical quality of the input signal to the statistical quality of the signal output by the detector [Bushberg et al., 1994]. If the imaging system added no noise to the signal and had a perfect MTF(f), the DQE(f) would be 100% for all frequencies. However, there are many steps in the imaging chain, each adding noise to the image. A partial list of the steps that can add noise includes incomplete absorption of the incident x-ray photons in the photoconductor/scintillator layer, incomplete charge collection (in the case of a direct detector) or incomplete light collection (in the case of an indirect detector) by the detector array, and readout noise inherent in the digitization of the signal. DQE(f) is calculated using the formula

$$DQE(f) = \frac{(MTF(f))^2}{X * q * NPS(f)}$$ (Eq. 3.2)

where MTF(f) is the MTF(f) calculated from the polynomial fit to the MTF(f) plot, NPS(f) is the noise power spectrum measured, q is the photon flux, in photons/mm^2/mR, and X is the exposure per frame, as measured with the ion chamber.

3.3.8   CT Data

For the a-Se detector and the a-Si detector, x-ray computed tomography (CT) data
was acquired by placing a rotation table between the detector and x-ray tube. The
distance from the source to the centre of rotation was 18 cm and the distance from the
source to the detector was 28 cm. The object imaged was a 1 cm diameter cylinder of
water with a nylon screw inside to give a region of lower attenuation. The phantom was
imaged for 400 views over a 360° rotation of the rotation stage. The x-ray tube setting
used for both was 40 kVp, 0.5 mm Al filtration, 350 μA x-ray tube current, and a 1 s
exposure per frame, corresponding to a 30 mR exposure on the detector for each frame.
The images were reconstructed using the Feldkamp reconstruction algorithm [Feldkamp
et al., 1984] using a ramp filter. Noise was measured in the reconstructed images by
measuring the standard deviation in the water region and the nylon insert region. The CT
number in HU was calculated for the nylon region using the formula

$$CT\#_{Nylon} = 1000 \left[\frac{\mu_{Nylon} - \mu_{Water}}{\mu_{Water}} \right]$$

(eq. 3.3)

with the error in the CT number being given by

$$\sigma_{CT\#} = \sqrt{\left(\frac{\partial CT\#_{Nylon}}{\partial \mu_{Nylon}} \right)^2 (\sigma_{Nylon})^2 + \left(\frac{\partial CT\#_{Nylon}}{\partial \mu_{Water}} \right)^2 (\sigma_{Water})^2}$$

$$\sigma_{CT\#} = 1000 \sqrt{\left(\frac{\sigma_{Nylon}}{\mu_{Water}} \right)^2 + \left(\frac{\mu_{Nylon} \sigma_{Water}}{\mu_{Water}^2} \right)^2}$$

(eq. 3.4)

where σ_{Nylon} and σ_{Water} refer to the standard deviation of the reconstructed μ value of the
nylon and water, respectively.

Due to the sensitivity change of the a-Se detector as a function of exposure history (section 3.4.3), this phantom was imaged for five successive scans on the a-Se system. The mean attenuation value and standard deviation was measured for each scan in order to see if the sensitivity shift caused changes in the reconstructed images. The data was reconstructed in two ways, firstly using a new flat field correction acquired before each scan, and secondly using only one flat field correction acquired at the beginning of the five scans.

3.4 Results

3.4.1 X-ray Spectra

Figure 3.4 shows a plot of the raw spectrum measured by the CZT detector, and the resulting spectra obtained by simulating a 0.5 mm and 1.0 mm Al filtration level. Since the attenuation of the spectrum results in a dramatic decrease in the number of photons in the spectrum, the simulated spectra are multiplied by a factor of 20 in order to be more easier seen on the scale of the plot.

3.4.2 Photon Fluence

The photon fluence was calculated to be 49604 photons/mm^2/mR for the 40 kVp beam with 0.5 mm Al filtration and 67757 photons/mm^2/mR for the 40 kVp beam with 1.0 mm Al filtration.

Figure 3.5 shows a plot of the ratio of the mean signal level to the initial frame mean signal level for each of the detectors for 200 successive exposures. The a-Se detector response drops by 15% over the first 200 exposures, and continues to drop with increasing exposure frame, reaching a 45% decrease in sensitivity over 2000 exposure frames. This drop is likely due to two effects. First, there is a buildup of trapped charges in the Se layer, which can recombine with the holes and reduce the charge collected. Secondly, the buildup of trapped charges can alter the electric field being applied though a space-charge effect. This change in the electric field can reduce the hole collection efficiency. The CCD signal decreases by a very minor 1% before stabilizing. It is
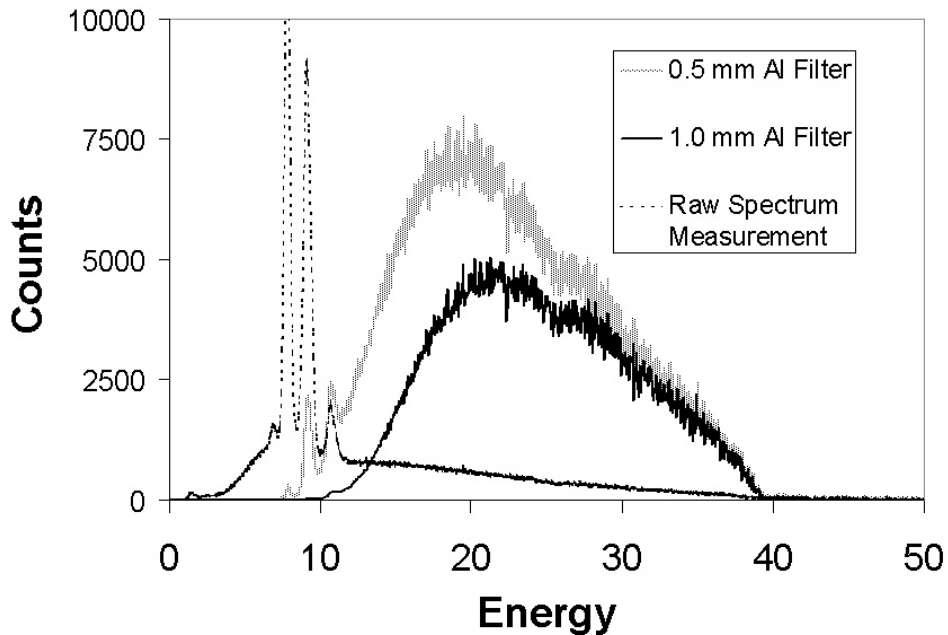
Figure 3.4. Energy spectrum for the raw beam and for simulated 0.5 mm Al and 1.0 mm Al filters. The filtered spectra are multiplied by a factor of 20 in order to be more easily seen on the scale of the plot.

uncertain what the precise cause of this change in signal is. The a-Si signal increases approximately 5% from the first frame to about the 20th frame, where it stabilizes. In the plot of the a-Si detector signal, there are occasional drops in the signal. This is because of a shutter control problem, and is not related to the performance of the detector. The increase in signal level is due to image lag in the detector causing a buildup of charge in the array. This lag follows an exponential decay pattern and thus a correction can be devised for it if the previous exposure frames are still saved.
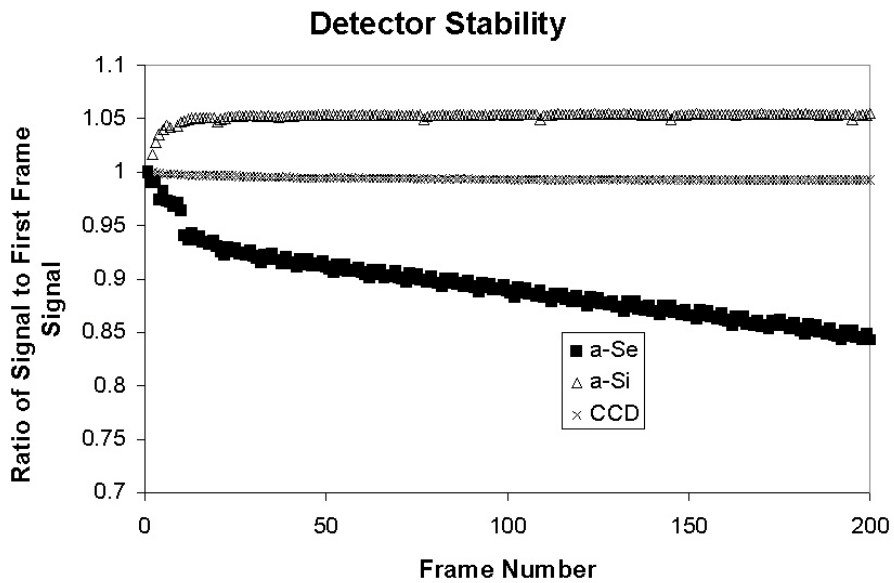
Figure 3.5. Plot showing the ratio of the mean signal level on each detector to the mean signal level in the first exposure frame. For the a-Si detector, there is a slight 5% increase in the signal level from frame 0 to 200. The drops in the signal level along the curve are because of x-ray shutter problems. For the CCD detector, the signal level is very constant, with a drop of less than 1%. The a-Se detector response drops by 15% after 200 views, and continues to drop, with the response being at 55% of the initial value after 2000 exposures.
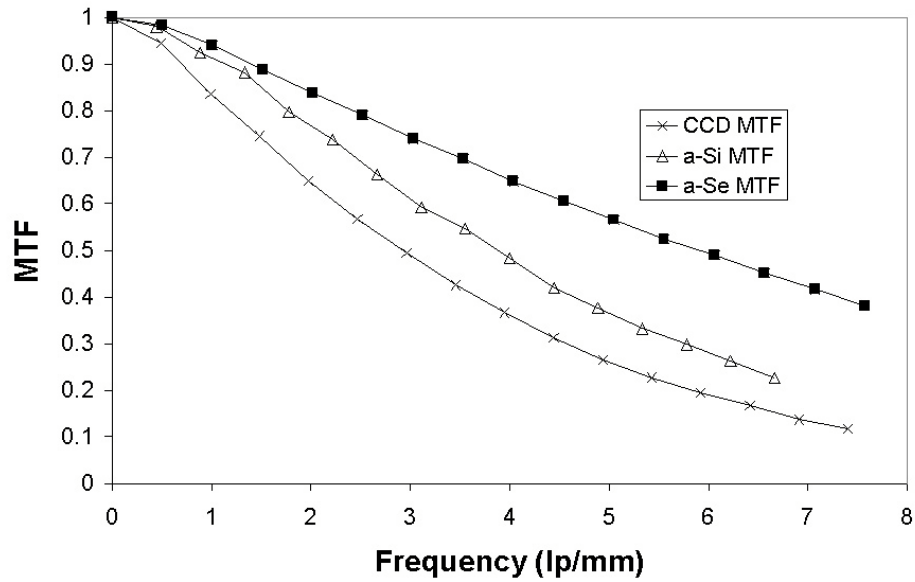
Figure 3.6. Plot of MTF(f) for all three detectors for a 40 kVp beam with 1 mm Al filtration.

3.4.4 MTF(f)

Figure 3.6 shows a plot of MTF(f) for all three detectors acquired with the x-ray tube set at 40 kVp and 1.0 mm Al filtration. No appreciable difference was seen in the MTF curves when the filter was changed to 0.5 mm Al. It can immediately be seen that the a-Se detector has the best MTF curve of the three detectors. This is not surprising since selenium is known to have a very high intrinsic resolution. The CCD and a-Si detectors both utilize the minR phosphor screen, so the difference in the MTF plot demonstrates the difference inherent in the detectors. The MTF of the a-Si detector is superior to the MTF of the CCD detector, largely due to the fact that the CCD system will have extra blurring caused by the fibre optic taper between the phosphor screen and the CCD.

3.4.5   NPS(f)

Figure 3.7 shows the NPS(f) for the x-ray settings of 40 kVp, 1.0 mm Al filter and 30 mR per exposure. Figure 3.8 shows the NPS(f) for the case of 40 kVp, 1.0 mm Al filter and 3 mR per exposure. In the 30 mR per frame plot, it can be seen that at low frequencies, the a-Se detector is superior while at higher frequencies, the a-Si detector approaches the a-Se NPS and the CCD NPS becomes considerably better. Similar behavior is seen in the plot of NPS at the case of 3 mR exposure per frame. It is believed that the better performance of the NPS at high frequencies for the a-Si and CCD devices is due to the blurring in the phosphor screen. This blurring essentially acts as a smoothing kernel, attenuating the noise at higher frequencies. Another factor that could serve to increase NPS(f) of the a-Se detector is the high MTF at the Nyquist frequency, which means that noise of frequencies above the Nyquist limit might be aliased back into frequencies below the Nyquist frequency. Also evident from the plots is that at high exposures (30 mR), the NPS(f) of the a-Si and CCD detectors are identical at low frequencies. However, in the low exposure NPS(f) (3 mR), the CCD has a superior NPS value at low frequencies. This would suggest that the performance of the a-Si device falls off quicker as exposure is reduced than the CCD device.

3.4.6   DQE(f)

Figure 3.9 shows the plot of DQE(f) for the x-ray setting of 40 kVp, 1.0 mm Al filtration and 30 mR per frame. It can be seen that the DQE of the a-Se detector is considerably higher than the other two detectors. The DQE measured for the a-Se
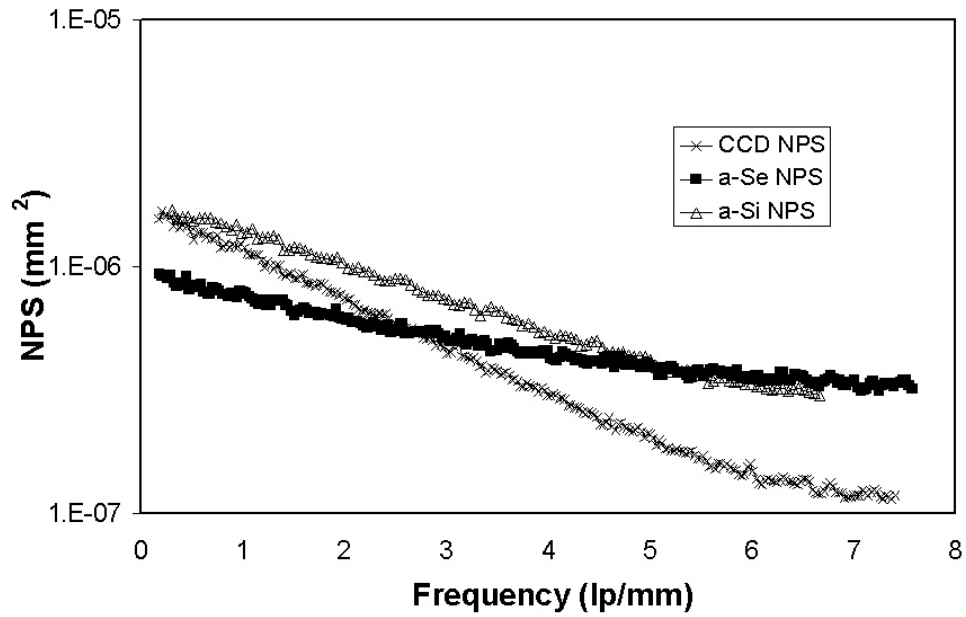
Figure 3.7. NPS(f) plots for the x-ray tube set at 40 kVp, 1.0 mm Al filtration, and 30 mR per frame.
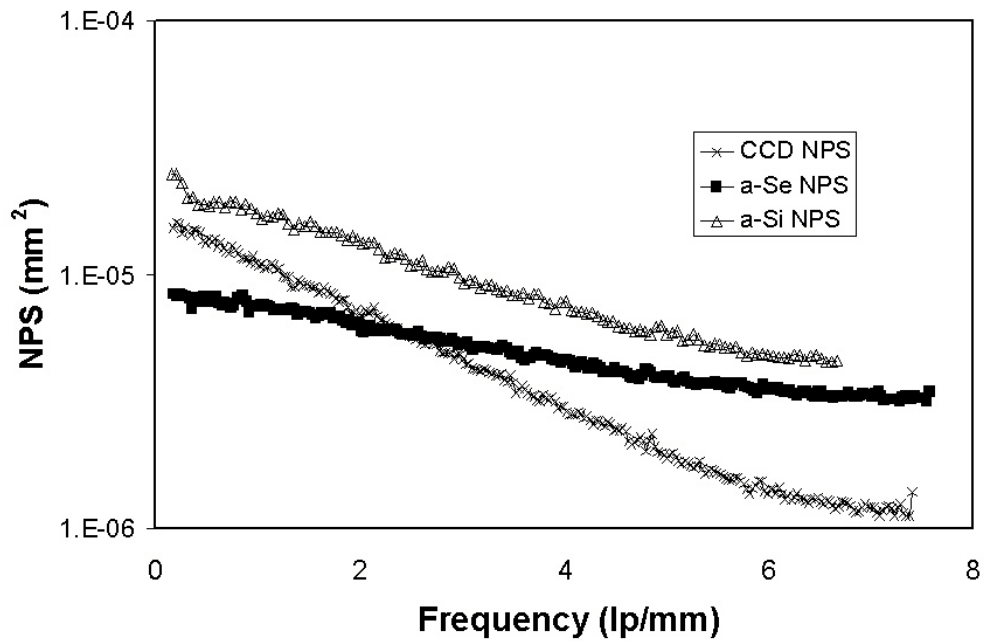
Figure 3.8. NPS(f) plots for the x-ray tube set at 40 kVp, 1.0 mm Al filtration, and 3 mR per frame.
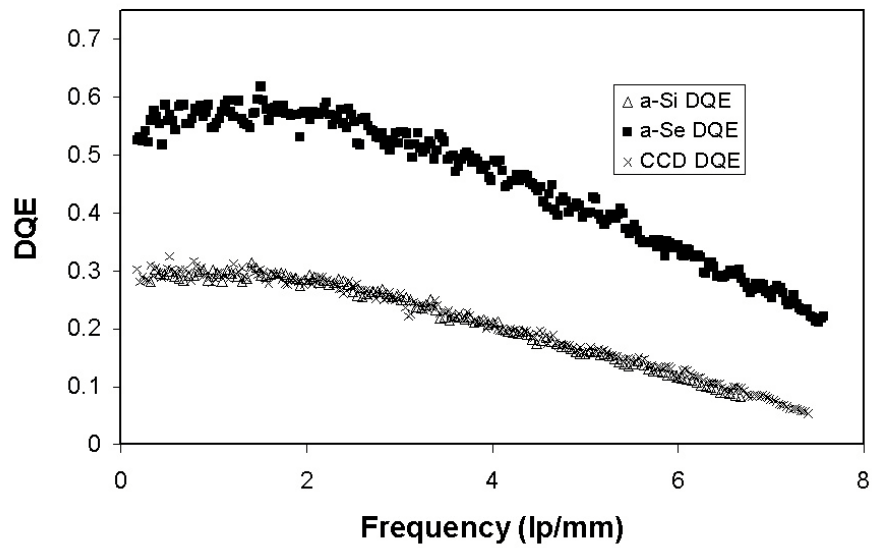
Figure 3.9. Plot of DQE(f) for the three detectors at x-ray tube settings of 40 kVp, 1.0 mm Al filtration, and 30 mR per frame.
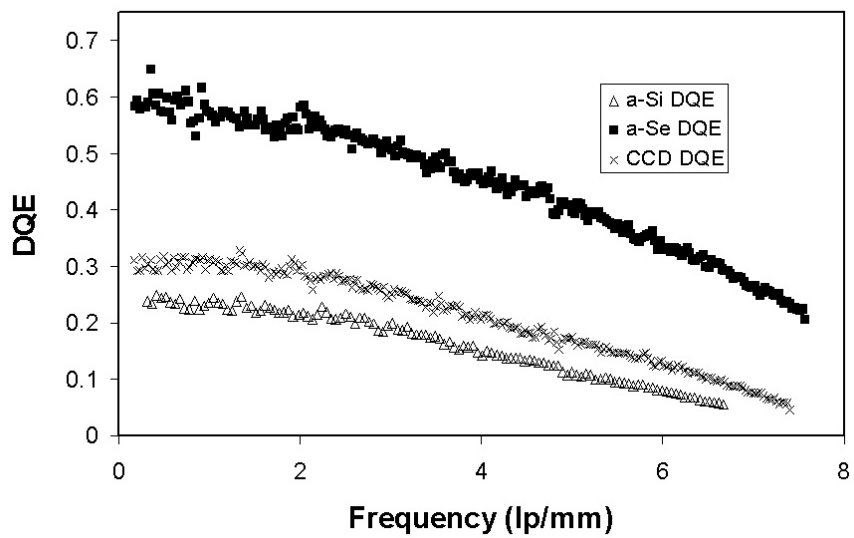
Figure 3.10. Plot of DQE(f) for the three detectors at x-ray tube settings of 40 kvp, 1.0 mm Al filtration, and 3 mR per frame.

detector also agrees well with what was reported by Andre et al. [Andre et al., 1998].

Also interesting to note is that the DQE of the other two detectors is essentially identical.

This would suggest that at this exposure level, the limiting factor of their performance is

the scintillating screen placed on the detector. Figure 3.10 shows the plot of DQE(f) for

x-ray settings of 40 kVp, 1.0 mm Al filtration, and 3 mR per frame. The a-Se detector is

still considerably better than the other two detectors. At this exposure level, the DQE of

the a-Si detector drops below that of the CCD detector. This drop is likely due in part to

the larger dark current on the a-Si device when compared to the CCD device. At the low

exposure level, the dark current on the a-Si device can be several times larger than the

signal that is being measured. Since the entire dark current image is essentially thermal

and electronic noise, there is a resulting decrease in the signal to noise ratio at low

exposure levels. Since the dark current of the CCD is much lower, this noise component

is not as severe. Figure 3.11 shows the DQE(f) for the a-Se detector at 40 kVp, 0.5 mm

Al filtration, and exposure levels of 30, 3, and 0.3 mR per frame. The DQE does not

change when the exposure is lowered from 30 to 3 mR per frame, but then begins to drop

off as the exposure level continues to drop. Figure 3.12 shows the DQE(f) for the CCD

detector at 40 kVp, 30 mR per frame and filtration levels of 0.5 and 1.0 mm Al. It can be

seen that the DQE is slightly higher for the beam with the lower filtration level. This is

likely due to the better efficiency of the minR screen for the softer x-ray beam. Figure

3.13 shows the DQE(f) for the a-Si detector at 40 kVp, 1.0 mm Al filtration, and

exposure levels of 30 and 3 mR per frame. As discussed earlier, there is a drop in DQE

for this exposure level change.
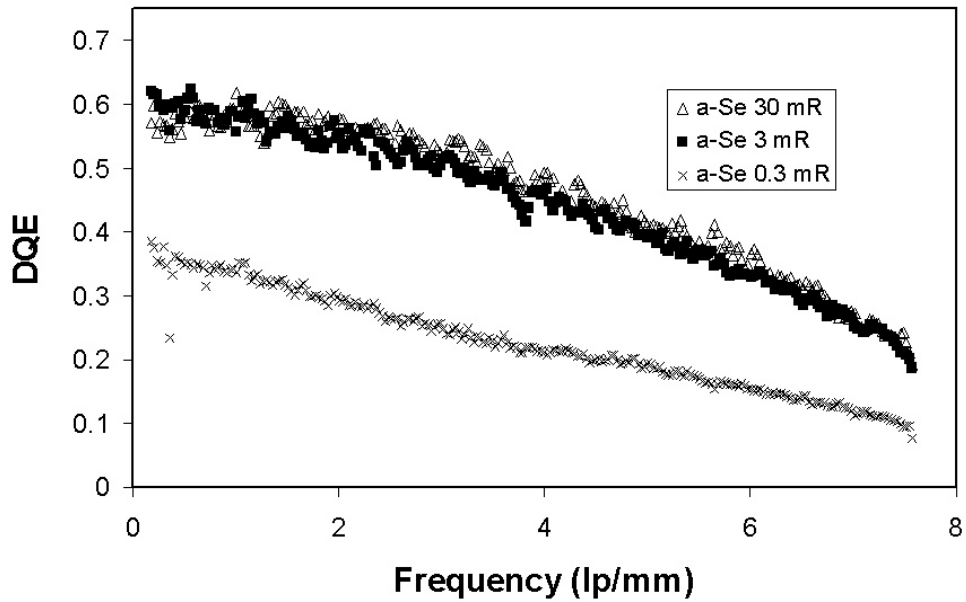
Figure 3.11. Plot of DQE(f) for the a-Se detector with the x-ray tube set at 40 kVp and 0.5 mm Al filtration and exposure levels of 30, 3, and 0.3 mR per frame.
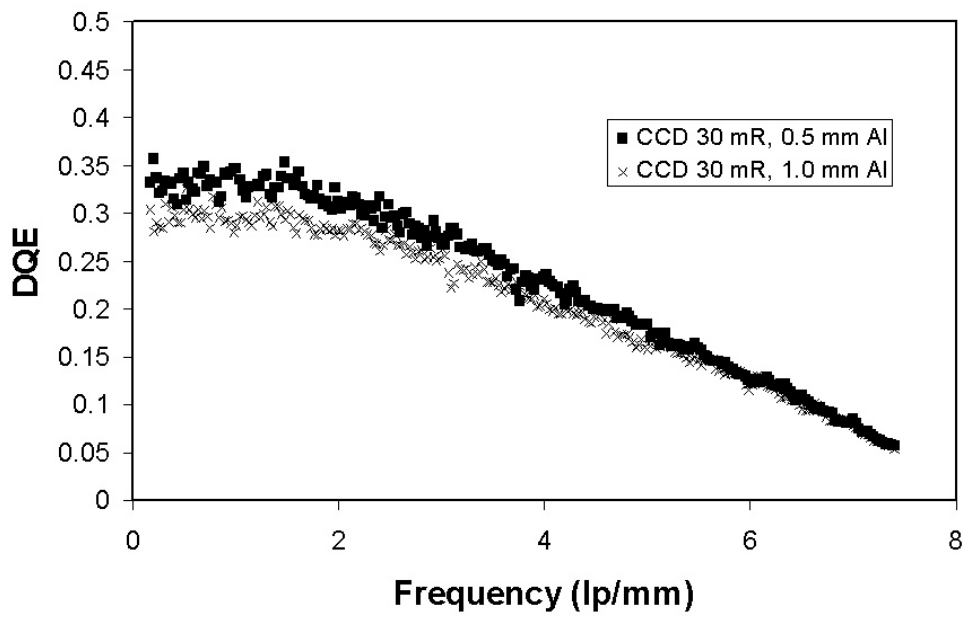
Figure 3.12. Plot of DQE(f) for the CCD detector with the x-ray tube set at 40 kVp, 30 mR per frame, and filtration levels of 0.5 and 1.0 mm Al.
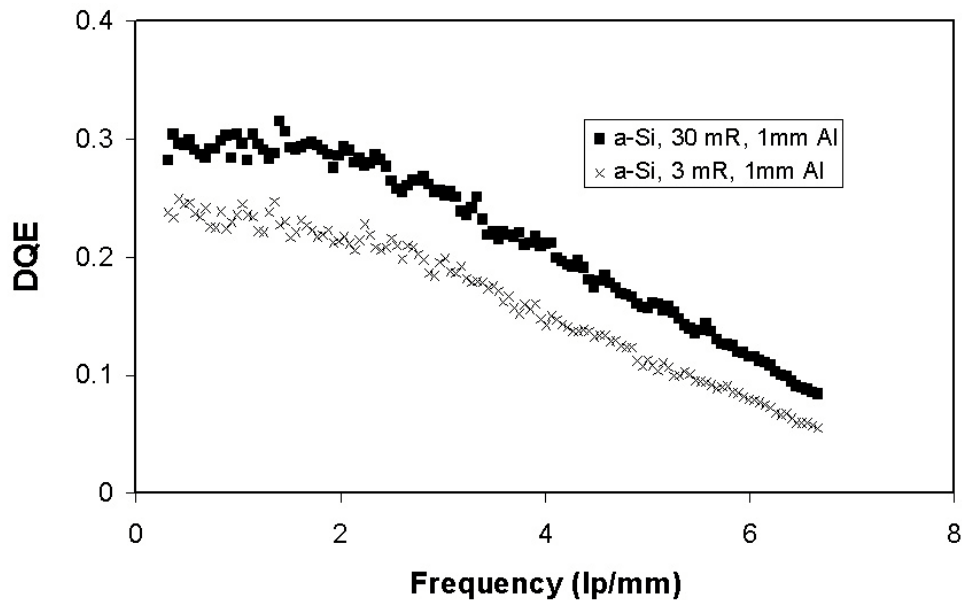
Figure 3.13. Plot of DQE(f) for the a-Si detector at 40 kVp, 1 mm Al filtration, and exposure levels of 30 and 3 mR per frame.

In typical microCT usage of these detectors, the exposure level per frame is 25 – 30 mR per frame (measured at the detector). The region of the detector shadowed by the mouse will see an exposure of 25% - 50% of this level, corresponding to 12.5 – 15 mR per frame.

3.4.7 CT Images

Figures 3.14 and 3.15 show reconstructed images of the phantom from the a-Se and a-Si detectors, respectively. Both of these images are through regions of the phantom where the nylon bolt can be seen. From the images, it can be immediately seen that the a-Si images appear to have much better noise characteristics. This is confirmed by looking

at the standard deviation in a uniform area of the phantom. These results are listed in

table 3.1.

Detector	Water μ value	Water % s.d.	Nylon μ value	Nylon % s.d.	Nylon CT Number
a-Se	0.046037	11.5	0.038246	13.3	-169±146
a-Si	0.056275	7.70	0.045678	8.16	-188±91

Table 3.1. Reconstructed μ values (in 1/mm) of water and nylon for the a-Se and a-Si detectors and CT numbers (in HU) for nylon. The CT numbers for water are not tabulated since they are by definition 0.
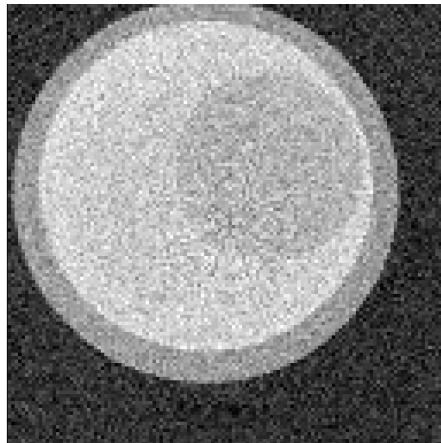
Figure 3.14. Reconstructed image of the phantom for the a-Se detector.
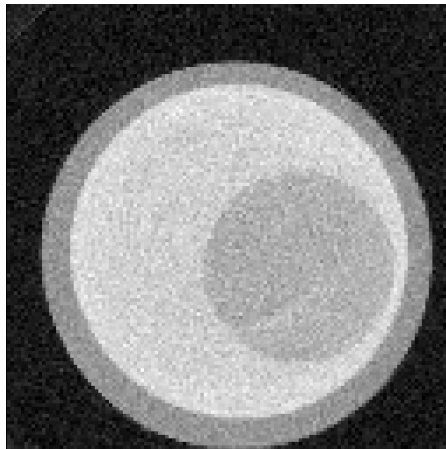
Figure 3.15. Reconstructed image of the phantom for the a-Si detector. Note the apparent reduction in noise vs. the a-Se detector images. The line seen in the nylon bolt section is a partial volume effect of reaching the top portion of the nut head that is grooved with a slot. The region containing the artefact was not used in the analysis.

Differences in the images obtained with the two detectors can immediately be seen from table 3.1. The standard deviation of the image in a uniform region of the phantom is indeed lower for the a-Si detector images. This difference in noise is possibly due to many sources. Firstly, the a-Si detector has a lower MTF curve compared to the a-Se detector, meaning that there is more blurring going on, resulting in smoother images. Secondly, the pixel size of the a-Si detector is 75 μm vs 66 μm for the a-Se detector, corresponding to an approximately 30% increase in pixel area. The data from the a-Se detector might have to be smoothed to match the resolution of the a-Si detector in order to account for this difference. Also immediately obvious from table 3.1 is that the reconstructed μ values are different, being higher for the a-Si detector images. This difference is due to the fact that the attenuation of the x-rays in the Se has a different energy dependence than the attenuation in the GOS minR screen, as shown in figure 3.1. Since the high energy photons are stopped less in the GOS than the a-Se, and these same high energy photons are less attenuated in the phantom than the low energy photons, the attenuation of the x-rays as measured by the GOS screen will be greater than that measured by the a-Se detector. This will result in the difference in the reconstructed attenuation values. The CT number for nylon is lower for the images acquired on the a-Si system than on the a-Se system, meaning that the ratio of μ_{Nylon} to μ_{Water} is different for the two systems as well.

Scan #	μ_{water} (New flat field correction)	% s.d.	μ_{water} (Old flat field correction)	% s.d.
1	0.047529	13.5	0.047529	13.5
2	0.046502	11.7	0.043552	14.2
3	0.045890	11.9	0.040987	15.2
4	0.044983	10.6	0.038871	14.8
5	0.045245	10.9	0.037263	13.4

Table 3.2. Reconstructed μ values (in 1/mm) and standard deviation for water in five successive CT scans preformed on the a-Se system. The first two columns of data represent the values obtained when a new flat field correction image is acquired before each scan while the last two columns represent the values obtained when the flat field correction used is the one acquired before the first scan.

Table 3.2 lists the reconstructed μ value for water from each of the five successive scans of the phantom using the a-Se detector. When a new flat field correction is acquired before each scan, the μ value for water decreases by approximately 5% over the five scans. When the flat field correction used in the one acquired before the first scan, the μ value decreases by 22% over the five scans. This decrease is a direct result of the sensitivity change of the detector. By acquiring a new flat field correction image, the exposure history of the device, and subsequent shifts in sensitivity of the detector in different regions, is accounted for. This method does not however account for the change in sensitivity that occurs within one scan. This drift in the μ value of water is one of the complicating factors that made routinely converting the data to CT numbers in HU difficult, as mentioned briefly in section 2.6. It might be possible to improve upon the 5% change in the μ value of water by acquiring a set of flat field correction images before and after the scan, and then using an average of the two to normalize the images.

3.5 Discussion/Conclusion

Each detector has its own set of advantages and disadvantages. The high DQE of the a-Se detector makes it very good for radiographic imaging, but its large sensitivity shift as a function of exposure history makes it a less ideal candidate for CT imaging since quantitative CT imaging depends on having a stable detector. The sensitivity shift might not have that great an impact on the reconstructed images since repeat measurements of the same phantom showed a minimal change in the μ values of water. The CCD detector exhibits very good stability as a function of exposure history, but has the worst MTF of any of the detectors. This is due to blurring in not only the phosphor, but also in the fibre optic taper. The fibre optic taper also introduces pincushion distortions into the image, which must be corrected for. The a-Si detector has a large dark current component, which adds noise to the images at low exposure levels. However, this device has a good MTF due to the direct coupling of the phosphor to the detector surface. The performance of both the CCD and a-Si detectors seems to be currently limited by the choice of phosphor placed on them since the DQE is identical for both of these devices at high exposure levels.

Chapter 4. Radiation Dose to the Mouse in a microCT Scan

4.1 Introduction

The quality of image that can be obtained in a microCT scan of a mouse is ultimately limited by the radiation dose that the mouse being imaged can tolerate. If a microCT scanner gives images of high quality but gives an unacceptably large radiation dose to a mouse, then it can not be practically used for longitudinal studies of a mouse, where the same animal would be imaged multiple times. Ford et al. [Ford et al., 2001] estimate that in order to obtain a variance of 1% in the reconstructed attenuation values, assuming an ideal detector, doses of 0.1 Gy, 1 Gy, and 10 Gy are needed for voxel size of 400 μm, 200 μm, and 120 μm respectively. Considering that the lethal dose in 50% of mice in 30 days (LD50/30) is 7.85 Gy [Patchen et al., 1992], the dose should certainly be kept on the order of cGy and not Gy.

Other groups investigating the problem of radiation dose to the mouse from a microCT scan have reported widely varying doses. The dose to the bladder of a mouse for a 390 view scan was measured using thermoluminescent dosimeters (TLDs) to be 45 cGy by Paulus et al. [Paulus et al., 2000]. TLD measurements and Monte Carlo simulations done by Chow et al. [Chow et al., 2001] report a dose of 10.4 cGy. These results suggest that the effects of radiation doses in the cGy range should be studied. Fornace et al. [Fornace et al., 2002] report the induction of stress-response genes *in-vitro* by gamma ray doses as low as 2 cGy. However, 2 and 5 cGy doses did not result in any increased apoptosis of the cells. Amundson et al. [Amundson et al., 2001] report elevated gene expression maintained in several organs *in vivo* for at least a day after exposure to

gamma rays doses as low as 20 cGy. The x-ray doses reported for microCT scans by Paulus are certainly sufficient to cause these elevated levels of gene expression.   This increase in gene expression is a concern for a combined PET-CT system that will be used, among other things, to image levels of gene expression in mice.

In order to determine the radiation dose delivered to a mouse from the microCT x-ray system described in chapter 2, both analytical simulations and TLD measurements were performed. These measurements were performed for a variety of x-ray spectra, including both Mo anode and W anode spectra. Section 4.2 discusses the methods of the simulations. Section 4.3 describes the process of the TLD measurements. The results of the simulations are presented in section 4.4, while the results of the TLD measurements are shown in section 4.5. Section 4.6 discusses the results and their limitations.

4.2 Computer Simulations

4.2.1   Choice of X-ray Spectra

Four x-ray spectra were chosen for an in depth analysis of dose using computer simulation methods. These spectra are the same ones described in section 2.5.2 and listed again in table 4.1. The x-ray beam spectra are plotted in figure 2.21. The choice of tube current and exposure time was made so that the mean signal response of the detector was approximately the same for each setting.

Beam	Anode	kVp	Filter (in mm)	Tube Current (mA)	Exp. Time (s)
A	Mo	30	0.02Mo + 0.5Al	1.0	2.0
B	Mo	40	0.02Mo + 0.5Al	0.8	1.0
C	W	40	1.0Al	0.6	1.0
D	W	40	2.0Al	1.2	1.0

Table 4.1. Information about each of the four spectra used in the measurements and the labels for each.

4.2.2 X-ray Exposure Measurements

The x-ray exposure per frame for each of the spectra chosen was measured using a Keithley 35050 dosimeter with a 96035B ion chamber (Keithley, Cleveland, OH).

4.2.3 Energy Fluence Calculations

The average mass energy-absorption coefficient, $(\mu_{en}/\rho)_{avg}$, for each of the x-ray spectra in air is calculated for the polyenergetic beam according to the formula

$$\left(\frac{\mu_{en}}{\rho}\right)_{avg} = \frac{\int\limits_{E}\Psi(E)\cdot\left(\frac{\mu_{en}}{\rho}\right)_{E}dE}{\int\limits_{E}\Psi(E)dE} \qquad \text{(eq. 4.1)}$$

where $\Psi(E)$ is the energy fluence of the x-ray beam (equal to energy times number of photons at that energy from the measured spectrum). The total energy fluence Ψ (in J/m^2/frame) for the beam is then calculated as

$$\Psi = \frac{X(R)\cdot 33.97(J/C)\cdot 2.58\times10^{-4}(C/kg/R)}{\mu_{en}/\rho\,(m^2/kg)} \qquad \text{(eq. 4.2)}$$

where X is the exposure in Roentgens for each frame.

4.2.4 Mouse Images

Two mice were imaged using the four spectra described above, one for the W anode spectra and the second mouse for the Mo anode spectra. Each acquisition consisted of 400 views over a full circle orbit. The data is acquired and reconstructed according to the methods described in chapter 2.

4.2.5 Dose Simulation Methods

The dose for each acquisition is estimated by using a ray-tracing algorithm which exponentially deposits energy from the x-ray beam into the reconstructed image volume. Upon entry into the image volume, the x-ray beam has an energy flux Ψ and this energy flux is deposited according to the magnitude of the attenuation values in the reconstructed image. This dose deposition process is carried out across all projection views in a manner that simulates the CT acquisition process. The result of this simulation is an image of energy deposited per voxel, allowing dose to be calculated by dividing by the density of material in the voxel. Densities used are 1 g/cm^3 for soft tissue and 1.85 g/cm^3 for bone.

4.3 TLD Measurement Methods

4.3.1 TLD Description and Preparation

When a x-ray or gamma photon interacts in a TLD crystal, electron-hole pairs are produced which can become stuck in trapped states. Upon completion of the irradiation, the dose deposited in the TLD can be measured by heating the TLD crystal in order to release the trapped states. When the electrons and holes recombine, visible light is emitted, which can be measured with a photomultiplier tube.

The TLDs used for the dose measurements were $1 \times 1 \times 1$ mm^3 Thermo RMP LiF:Mg,Ti (TLD-100) crystals (Thermo RMP, Solon, OH). Prior to irradiation, the TLD crystals were annealed at 400°C for 1 hour, followed by a rapid cooling to room temperature, followed by a further annealing at 100°C for 2 hours. This annealing

process is done in order to remove any residual trapped electron-hole pairs in the crystal. Upon completion of the annealing process, the TLDs must be kept in the dark since they are sensitive to light.

4.3.2 TLD Readout

The TLD crystals were read out one week after irradiation using a Thermo RMP 3500 TL reader, heating from room temperature to 400°C at a rate of 10°C/s. As a TLD is heated, there are energy thresholds for trapped charge which are passed [Attix, 1986] and each threshold being passed causes an increase in the light output of the TLD crystal. This pattern leads to complicated glow curves as shown in green in figure 4.1. In order to accurately determine the dose deposited in the TLD, the curve must be deconvolved into its component peaks. In figure 4.1, these peaks are represented by the red curves. Generally peak 5, the largest peak in the signal, is used for dosimetry calculations.
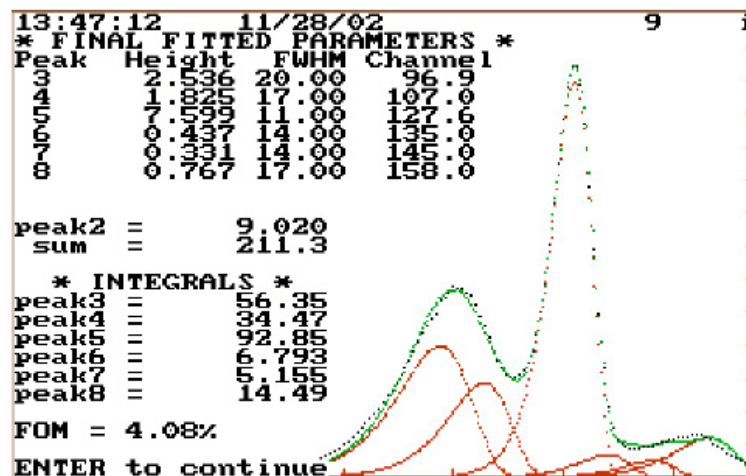
Figure 4.1. A glow curve for a typical TLD crystal. The green line shows the total light output as a function of temperature while the red plots show the individual component peaks deconvolved from the total output curve.
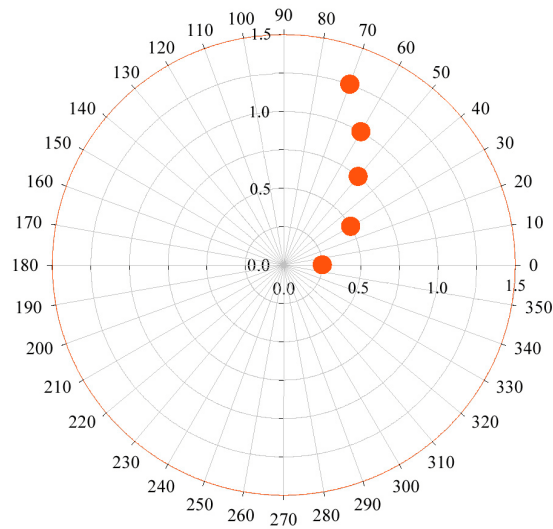
Figure 4.2. Diagram of the mouse-like phantom used to hold the TLDs. Note the
staggered design which ensures that there will be minimal shadowing of the TLDs.

4.3.3   X-ray Settings

TLD dosimetry measurements were done for three different x-ray tube settings,
listed in table 4.2.   The exposure measurements were made with a Keithley 35050
dosimeter with a 96035B ion chamber (Keithley, Cleveland, OH) placed at the centre of
rotation of the CT system. The CT system was set up as described in chapter 2.

Beam	Anode	kVp	mA	Filter	Exposure Time	Exposure per frame
1	W	40	0.6	1 mm Al	1 s	71.5 mR
2	Mo	30	1.0	20 μm Mo + 0.5 mm Al	2 s	128.0 mR
3	W	50	0.5	2 mm Al	1 s	43.0 mR

Table 4.2. X-ray beam characteristics for the TLD measurements. Note that the exposure
measured is at the centre of rotation of the CT system.

4.3.4   TLD Holder Phantom

A mouse phantom was constructed from a stack of 3 cm diameter, 3 mm thick polycarbonate disks. Holes were drilled into the face of each disk to hold the TLDs in two patterns. The first pattern of holes is shown in figure 4.2. The TLDs are placed in a staggered design in order to minimize the shadowing of the crystals during irradiation. The radial distance of the holes is 0.25, 0.5, 0.75, 1.0, and 1.25 cm. The second pattern consisted of a single hole placed at the centre of the phantom. The phantom was assembled using alternating disks of the two types. Once TLDs were placed in the phantom, it was wrapped in black electrical tape in order to keep the TLDs in the dark.

4.3.5   TLD Calibration

In order to calculate the dose deposited in the TLDs, the light output of the TLDs needs to be calibrated by exposing a set of calibration TLDs to a known exposure level for each x-ray spectrum used. To perform the calibration, 3 TLDs were exposed for 300, 600, and 1000 frames for each of the x-ray spectra used. In addition, the effects of any background radiation absorbed by the TLDs is corrected for by reading out five TLDs that were not irradiated, but were kept with together with the TLDs that were irradiated. The signal level of these five TLDs is assumed to be the background level that all of the TLDs will possess, and thus this level is subtracted off of the signal of the TLDs that were irradiated.

4.3.6   Phantom Dosimetry Measurements

Three phantom irradiation measurements were performed using the x-ray tube settings provided in table 4.2. In each case, the phantom was scanned for 800 frames over a 360° orbit. For each scan, the phantom was filled with 19 TLD crystals. This corresponded to 3 disks of the type shown in figure 4.2, and 4 disks with the TLD at the centre only.

4.3.7   Mouse Dosimetry Measurements

Three TLD crystals were wrapped in heat shrink tubing to protect them from water and light. These TLDs were then placed in the right kidney, left kidney, and liver of a euthanized mouse. The mouse was imaged using beam setting 1 from table 4.2 and an 800 frame study.

4.4 Results – Computer Simulations

4.4.1   X-ray Beam Information

Table 4.3 lists $(\mu_{en}/\rho)_{avg}$, exposure per frame, and energy fluence per frame for each of the four spectra. It can be seen that even though the exposure per frame varies widely, the energy fluence is approximately the same for each of the four beams.

Beam	μ_{en}/ρ (m^2/kg)	Exposure/frame (mR)	Ψ (J/m^2)
A	0.09497	90.9	8.39×10^{-3}
B	0.0816	96.5	1.04×10^{-2}
C	0.0584	60.0	9.00×10^{-3}
D	0.0512	49.5	8.47×10^{-3}

Table 4.3. Table listing $(\mu_{en}/\rho)_{avg}$, exposure per frame, and energy fluence for the four spectra being studied.

4.4.2   Dose Calculation Results

Figure 4.3 shows images of energy deposition per voxel for x-ray beams A and D. It can be seen that beam A causes a much sharper gradient in energy deposited from the outside of the image to the centre of the image.   This is most likely an effect of the increased beam hardening due to the lower mean energy of the beam.   Table 4.4 lists the dose to various tissues in the mouse calculated for each of the four x-ray spectra used.

Beam	Bone	Fat	Kidney	Muscle (near skin)	Muscle (near centre)	Testicle
A	D=19.8	D=9.04	D=10.8	D=14.4	D=10.7	D=6.18
B	D=19.7	D=10.0	D=12.3	D=15.2	D=12.0	D=7.30
C	D=19.5	D=7.00	D=9.34	D=11.0	D=9.29	D=6.01
D	D=14.1	D=6.04	D=8.10	D=9.13	D=7.78	D=5.03

Table 4.4. List of doses (in cGy) in various mouse tissues for each of the four x-ray settings.
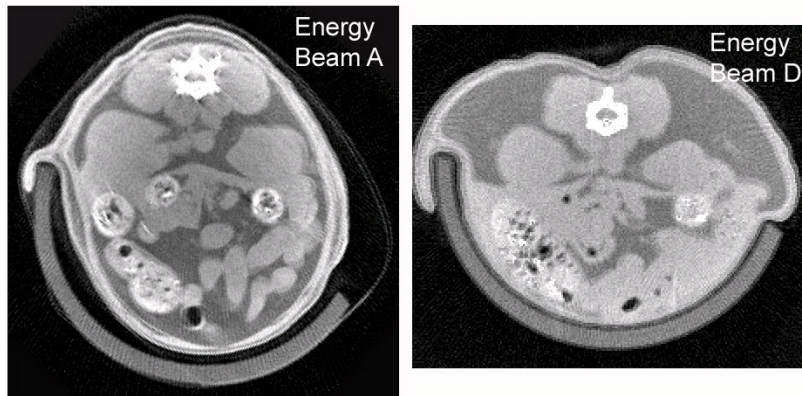
Figure 4.3. Energy deposition maps for beam A and beam D. It is important to note that the images represent energy deposited per unit volume. To get dose, the values need to be divided by the tissue density. Note the sharp dose gradient from the skin to the centre seen in the energy map of beam A due to the lower energy of beam A. This effect can be seen in the energy map for beam D also, but not as dramatically.
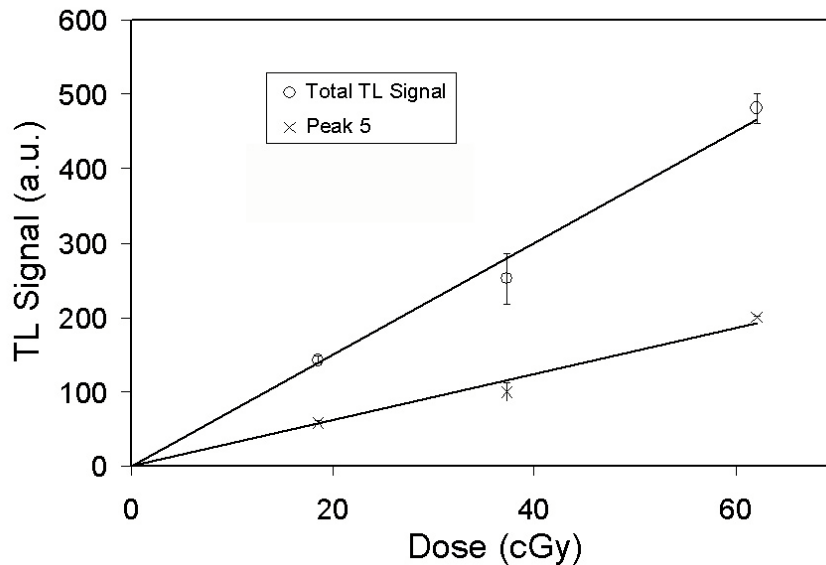
Figure 4.4. Calibration curve for the the 40 kVp, 1 mm Al filtration x-ray beam. The response of the TLDs is linear with dose deposited. The plot shows curves for both the total signal and the signal in peak 5 only.

4.5 Results – TLD Measurements

4.5.1   Calibration Curve

Figure 4.4 shows a calibration curve for x-ray setting 1. It can be seen that the response of the TLDs is linear with the dose. The plot also shows the difference between the total light output of the TLD vs. the output of just peak 5.

4.5.2   Phantom Dose Results

Figure 4.5 shows the dose measured using peak 5 of the TLD signal as a function of radial position for all three x-ray tube settings. The dose at the centre of the phantom for the 800 view studies range from a low of 21 cGy for the 50 kVp W beam to a high of
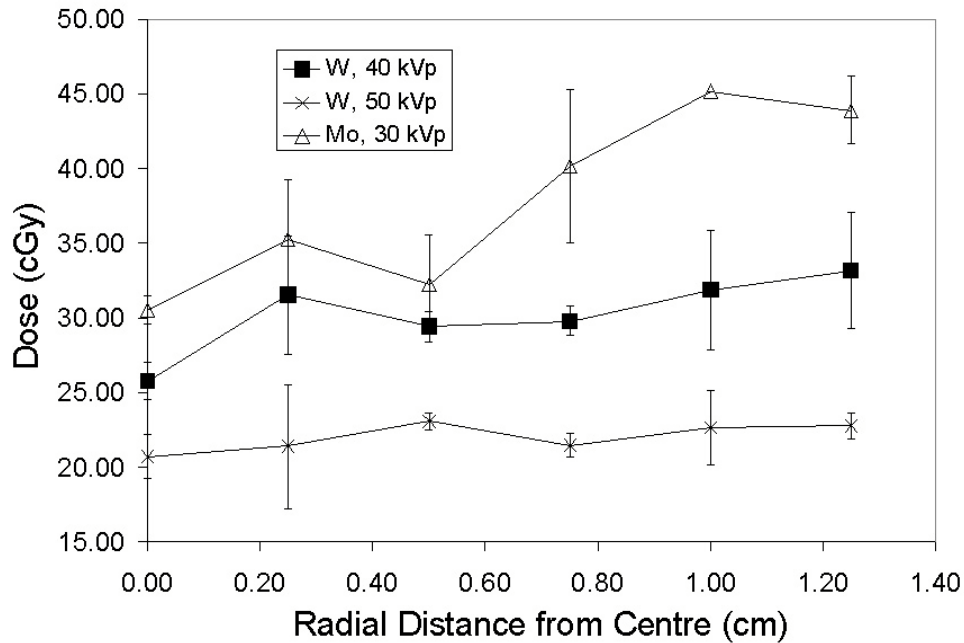
Figure 4.5. Dose as a function of radial position for the three different x-ray settings used. The dose is calculated using the output of peak 5 from the glow curve.

30.5 cGy for the 30 kVp Mo beam. It is also immediately obvious that the gradient of dose from the edge to the centre of the phantom is much steeper for the lower energy beam.

4.5.3 Mouse Dosimetry Results

The left and right kidneys of the mouse received doses of 24.8 cGy and 27.3 cGy respectively while the liver received a dose of 32c cGy. It should be noted that these results are from the placement of one TLD at each location and thus have no error bars associated with them. Since the phantom TLD measurements for the 40 kVp W x-ray beam had an average standard deviation of 2.5 cGy, the assumption can be made that the mouse dose measurements will have an error comparable to this.

4.6 Discussion

The TLD phantom measurements suggest that the dose to a mouse from a routine 400 view study at 40 kVp with 1 mm Al filtration on this microCT system would be vary from 12.5 cGy at the centre of the mouse to 16 cGy at the edge of the mouse. The TLDs implanted in the mouse would record a dose of 12.4 to 16 cGy for a similar scan, showing that the phantom seems to be a good approximation to a mouse for dosimetry purposes. These TLD measurements compare to the dose estimated by the computer simulations of 9.3 cGy to 11 cGy. Both methods predict a much stronger dose gradient for the softer Mo anode x-ray beams than for the higher energy W beam, as well as decreasing dose for higher energy beams. These doses compare favorably with the measurements made by Chow et al. [Chow et al., 2001], who estimated a dose of 10.4 cGy to the bladder of the mouse. These results are considerably lower than the 45 cGy results reported by Paulus [Paulus et al., 2000]. However, according to the Paulus group [Paulus, 2003], some of their measurements might have to be repeated now that they have a greater amount of experience in performing the TLD measurements.

Overall, the simulation and TLD results suggest that the dose to a mouse from a routine microCT scan can be kept below 10 cGy by utilizing a harder x-ray beam combined with a slightly reduced number of views. As was shown in section 2.5.2, there is little contrast lost by using a harder x-ray spectrum. This suggests using a harder x-ray spectrum would cause little compromise to the reconstructed images while at the same time reduce the dose by up to 50%.

Chapter 5. Simultaneous microCT and microPET Imaging of the Mouse

5.1 Introduction

In order to demonstrate the feasibility of simultaneous microCT and microPET imaging of the mouse and to explore the issues related to combining these two modalities, the CT system described in chapter 2 was combined with a small PET system. While multimodality PET/CT systems have also been developed recently for applications in clinical oncology [Beyer et al., 2000], these systems take sequential rather than simultaneous images with two axially displaced and essentially independent imaging systems. This avoids many of the challenges of integrating these two different imaging modalities that have been addressed in this work. These clinical systems are also not suitable for mouse imaging because of the high x-ray energy that is used, their low spatial resolution and cost considerations.

While both PET detectors and x-ray detectors detect high energy photons, they operate in very different modes. PET detectors record coincidences between pairs of 511 keV annihilation photons while x-ray detectors integrate millions of photons in a single frame. The x-ray photons can scatter into the PET detectors, causing a large increase in system deadtime and a corresponding reduction in system performance. Factors such as this will alter the design criteria for the PET system due to the need for shielding from the scattered x-rays.

The design of the PET-CT system is discussed in section 5.2. Section 5.3 discusses the measurements made with the prototype combined PET-CT system. Section

5.4 presents the results of the measurements and section 5.5 provides discussion of the results.

5.2 System Description

The PET detectors built for the combined PET-CT system uses detectors originally designed for a breast imaging system that have previously been characterized [Doshi et al., 2000]. The system has two detector heads, each consisting of a 2×2 plate of detector modules. Each module has a 9×9 array of $3 \times 3 \times 20$ mm^3 LSO crystals coupled via a tapered fibre optic bundle to a Hamamatsu R5900-C8 position sensitive photomultiplier tube (PSPMT) (Hamamatsu Photonics K. K., Japan). The pitch of the crystals in the array, after accounting for the inter-crystal teflon reflector, is 3.3 mm. This gives each detector an area of 60×60 mm^2.

The outputs of the PMTs are multiplexed to produce 4 position-dependent signals from each detector head, X^+, X^- Y^+ and Y^-, each of which is digitized. The location of the detected photon is determined using the equations $X = X^+ / (X^+ + X^-)$ and $Y = Y^+ / (Y^+ + Y^-)$. These X,Y coordinates are assigned to a specific crystal of interaction by using a look-up table (LUT). The LUT is constructed by acquiring a large number of events from a flood irradiation of the detector, which leads to a flood histogram in which all individual LSO elements can be identified. Each possible X,Y value is then assigned to a particular crystal in the array. Due to crystal-to-crystal differences in the detected signal amplitude for 511 keV events, individual energy thresholds are set on each crystal. The energy window for the system is set from $250 - 750$ keV. The PET data is

normalized by scanning a uniform cylinder of activity and measuring the singles rate of each crystal element to calculate the normalization [Casey and Hoffman, 1986]. No correction is currently applied for scatter, attenuation, randoms, or deadtime. Random coincidences and deadtime are minimized in these experiments as the singles count rate on the PET detectors is kept to $< 10^5$ counts per second on each detector head. The timing coincidence window for the system is set at 20 ns. The PET data is collected in fully 3D mode and then resorted into 2D sinograms using Fourier rebinning [Defrise et al., 1997]. The 2D sinograms are then reconstructed using standard 2D filtered back-projection.

The PET and CT components are mounted in a coplanar geometry on an optical
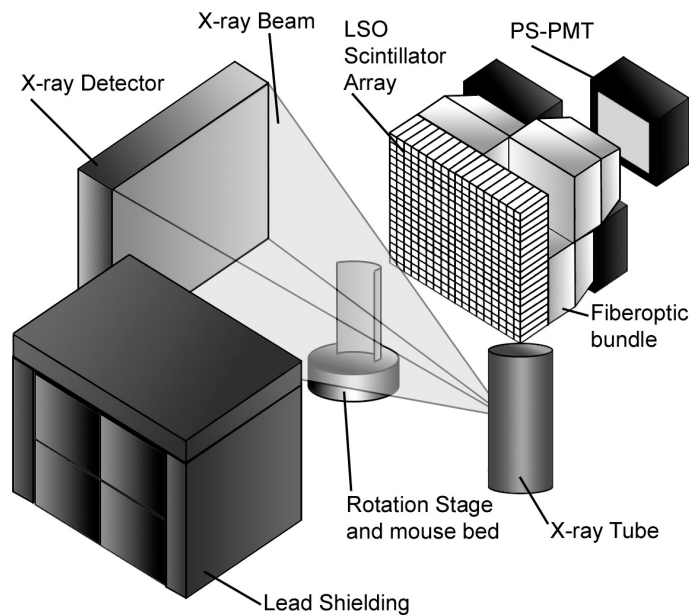
Figure 5.1 Schematic diagram of the experimental setup. The CT and PET components are mounted in a coplanar geometry so that the same portion of the mouse is imaged by both systems at once. The back PET detector is shown without the lead shielding in place in order to show the design of the detector modules. The lead shielding on the entrance face is 1.5 mm thick. The detectors remain stationary while the object is rotated on the bed mounted on the rotation stage.

table as shown in figure 5.1. It should be pointed out that the CT geometry is the same as is described in chapter 2. The distance from the x-ray tube to the x-ray detector is 30 cm while the distance between the two PET detectors is 22 cm. A central rotating stage is used to rotate the phantom or animal in front of the detectors to acquire tomographic information. Since the x-ray flux is many orders of magnitude higher than the 511 keV photon flux, scatter of x-rays from the object can easily saturate the scintillation detectors used to detect the annihilation radiation. For this reason, some shielding of the PET detectors is necessary. The amount of shielding used was 1.5 mm of lead in front of the PET detectors along with large lead bricks around the sides. This choice of shielding is discussed further in Section 5.3.1.

Data is acquired simultaneously for both the CT and PET systems in a step and shoot mode by rotating the object to the appropriate angle and pausing while data is acquired. Typical studies consist of either 200 or 400 views acquired over a 360° object rotation. The total acquisition time for these scans are 18 and 38 minutes respectively. The time to sweep the x-ray shutter at each step is 1 second. The CT and motion control systems are operated through a Windows NT PC running LabWindows/CVI (National Instruments, Austin, TX). The PET system is operated through a separate Windows 98 PC running LabView (National Instruments, Austin, TX). The data acquisition is synchronized between the two machines using a 5 line digital signal link between the data acquisition cards in the separate PCs.

5.3 System Measurements

5.3.1   Scattered X-ray Flux Measurement

The scattered x-ray flux and pulse-height spectrum also was measured using a single pixel $3 \times 3 \times 2$ mm^3 CZT detector (Amptek Inc, Bedford, MA).   These measurements were acquired by placing the CZT detector where one of the PET detectors would normally be placed.   Measurements were performed with no lead shielding, shielding on the front (entrance) side only, and shielding on all sides of the CZT detector. The amount of shielding in front of the CZT detector was varied from 0 mm to 2.25 mm of lead in steps of 0.75 mm.   The x-ray tube was run at 50 kVp and 1.0 mA for all measurements except in the case with no shielding, in which the tube current was reduced to 0.1 mA to prevent saturation of the CZT detector.   A water-filled cylinder, 3 cm in diameter and 10 cm in length, was placed on the rotation stage for these experiments to produce a distribution of scattered x-rays that mimics what would be observed when imaging a mouse.

5.3.2   PET System Measurements

The PET detectors were positioned as shown in figure 5.1 and data was acquired from a 3 cm diameter by 10 cm long cylinder, uniformly filled with a solution of ^{18}F at a concentration of approximately 60 kBq/cc. Coincidence counting rates were compared with no lead shielding in front of the detector and with 1.5 mm of lead in front of the detector with the x-ray tube turned off. With the 1.5 mm of lead shielding, the coincidence counting rate was measured again with the x-ray tube turned on at 50 kVp

with a tube current of 1.0 mA. No energy thresholding was applied to the PET detectors in these counting rate measurements. In addition to measuring the coincidence counting rate, the flood histograms (a histogram of X,Y coordinates over a large number of events) for each PET detector also were acquired and were examined to determine if there were any significant effects of operating the PET detectors while the x-ray tube was switched on. Specifically we looked for any degradation in crystal identification or dynamic range in the flood histograms.

The spatial resolution of the PET system was measured using a 3.7 MBq, 0.5 mm diameter ^{22}Na point source placed at the centre of the system. Projection data were acquired over 400 views with a total acquisition time of 40 minutes. The resolution of the system was measured as the FWHM of the point spread function in the reconstructed PET image. The sensitivity of the PET system was measured using a calibrated ^{68}Ge point source placed at the centre of the system. The energy window was set to 250 – 750 keV and the system was operated in fully 3D mode, with all lines of response being measured. The absolute sensitivity was calculated as the number of detected events divided by the number of decays by positron emission that were predicted to have occurred during the acquisition period.

5.3.3   Combined PET-CT: Phantom Studies

A simple phantom was created by drilling 9 holes varying in size from 3.0 to 5.9 mm in a 3.5 cm diameter acrylic rod. Six of the holes were filled with a solution containing a total of 4.4 MBq of ^{18}F and three holes were left empty. The cylinder was

imaged simultaneously on the benchtop CT-PET system with 200 angular projections being acquired in 18 minutes. The PET images are reconstructed as described in Section 5.2 and the CT images are reconstructed as described in section 2.4. After reconstruction the images are fused and displayed using the AMIDE software package [Loening and Gambhir, 2001].

5.3.4 Combined PET-CT: Mouse Studies

Two 30 g Swiss Webster mice were scanned on the CT/PET system. The mice were anesthetized using an injection of ketamine (100 mg/kg, i.p.) and xylazine (10 mg/kg, i.p.) for the imaging studies. The first mouse was scanned on the system 3 hours after an i.v. injection of 26 MBq of $^{18}F^-$. Fluoride ion is taken up in the bone and thus produces a skeletal image that can easily be correlated with the high contrast of bone seen on the CT images. The mouse was euthanized just prior to imaging, in order to allow experimentation with positioning and a longer scan time. The PET and CT scans were performed simultaneously using a 400 view acquisition protocol taking 38 minutes. The second mouse was imaged *in vivo* 50 minutes after the injection of 8.5 MBq of ^{18}F-FDG. ^{18}F-FDG is a glucose analog that produces images that are reflective of glucose metabolism. Simultaneous PET and CT scans were acquired over 200 projection views in 18 minutes.
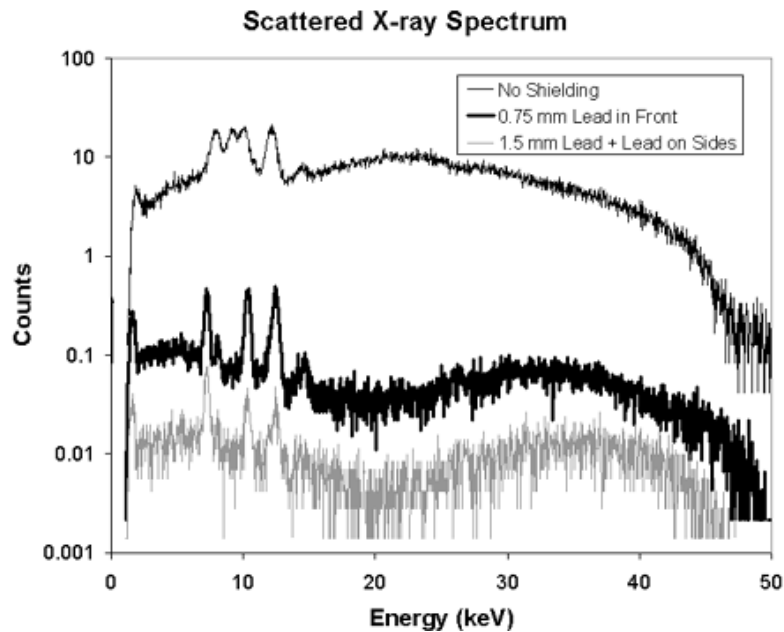
Figure 5.2. Scattered x-ray pulse-height spectra measured using the $3 \times 3 \times 2 \ mm^3$ CZT detector placed where one of the PET detectors normally sits. The counting rate for the three spectra (from top to bottom) was 9800 cps, 102 cps, and 14.7 cps. Note that the measurement with no lead shielding had an x-ray tube current of 0.1 mA while all others were taken with a current of 1.0 mA. All spectra were acquired with the tube set at 50 kVp.

5.4 Results

5.4.1 Scattered X-ray Flux Measurements

The measured counting rates due to scattered x-rays recorded by the CZT detector were 9800 counts per second (cps), 102 cps, 95.1 cps and 94.4 cps for shielding thicknesses of 0, 0.75, 1.5, and 2.25 mm of lead, respectively. With additional shielding around the sides of the detector, the measured count rates were 22.9 cps, 14.7 cps and 4.74 cps for shielding thicknesses of 0.75, 1.5 and 2.25 mm of lead respectively.

Figure 5.2 shows the pulse-height spectra of the scattered x-ray flux obtained with the CZT detector. This plot shows three spectra, corresponding to the measurements with

no shielding, 0.75 mm lead shielding on the front side only, and 1.5 mm lead shielding on the front plus lead shielding on all sides. In the latter case, the observed count rate of 14.7 cps in the 3×3 mm^2 CZT detector would give an approximate singles rate on one of the PET detectors of 4700 cps. This is less than the background due to natural radioactivity from the ^{176}Lu in LSO, which leads to a singles rate of 16,000 cps per detector. For a 20 ns timing window, the combination of LSO background and counts from scattered x-rays would only lead to a randoms coincidence counting rate in the PET system of 9 cps.
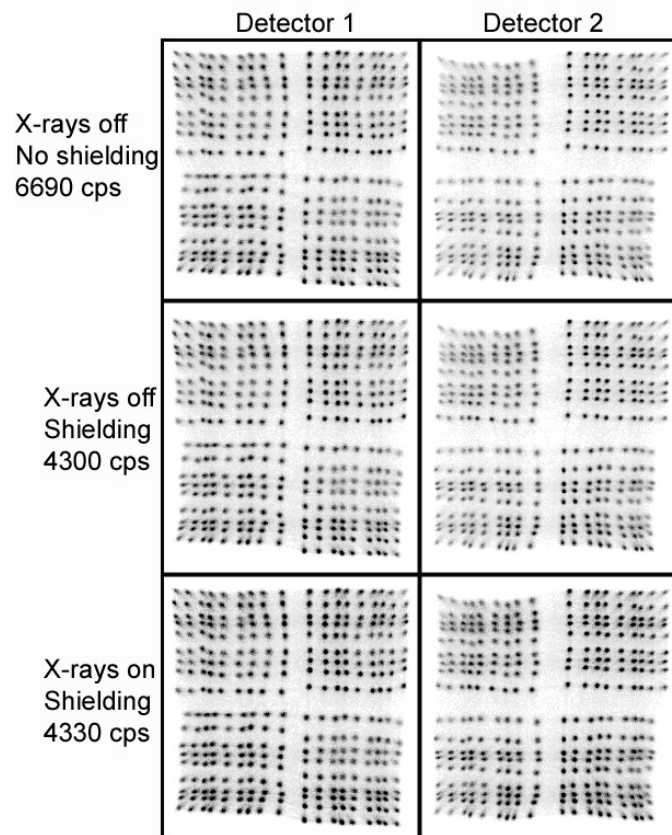
Figure 5.3. PET detector flood histogram images for (from top to bottom): x-ray tube off and no lead shielding; x-ray tube off and 1.5 mm lead shielding; and x-ray tube on and 1.5 mm lead shielding. The coincidence counting rate for the three data sets are 6690 cps, 4300 cps, and 4330 cps. 1.5 mm of lead is clearly sufficient to allow the PET detectors to operate when the x-ray tube is on.

5.4.2 PET System Measurements

Figure 5.3 shows flood histogram images from the two PET detectors. It can be seen that there is no apparent change in the flood histogram images due to the addition of the 1.5 mm thick lead shielding in front of the detector, or the operation of the x-ray tube. The coincidence counting rate dropped from 6690 cps to 4300 cps due to attenuation of the 511 keV annihilation photons by the 1.5 mm thick lead shielding. Operating the x-ray tube while acquiring the PET data increased the measured count rate to 4330 cps. Due to the large energy difference between the 511 keV annihilation photons in PET and the <40 keV x-ray photons for the CT, 1.5 mm of lead shielding removes the vast
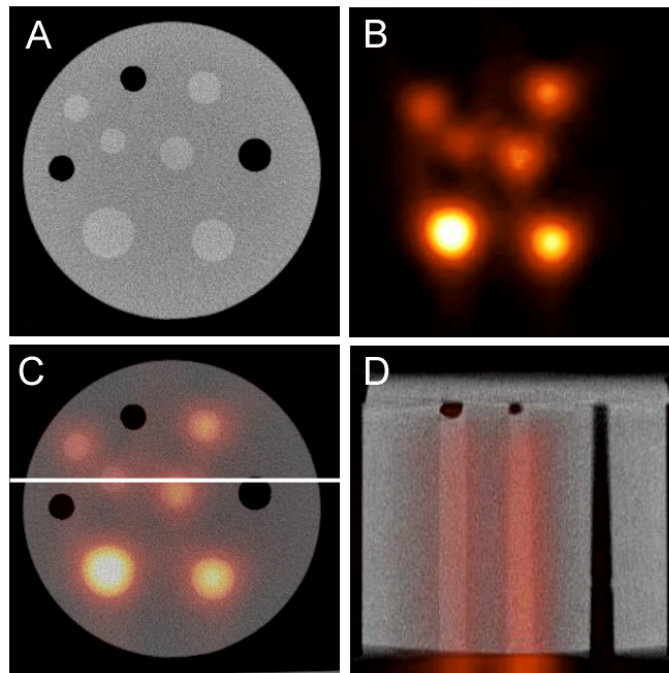
Figure 5.4. A hot-rod phantom containing 4.4 MBq of ^{18}F imaged with the combined PET-CT system. Note that in the CT image (A), six of the nine rods contain fluid with PET tracer, resulting in 6 spots in the PET image (B). The fused transverse image is shown in (C). The sagittal slice in (D) is through the line drawn in (C). The CT data was acquired at 40 kVp. Both the PET and CT data were acquired using 200 views over a 360 degree rotation in 18 minutes.

majority of the scattered x-rays while only absorbing approximately 20% of the annihilation photons. This amount of shielding allows simultaneous operation of the PET and CT systems without apparent artifacts in either data sets.

The reconstructed resolution of the PET system was measured to be 3.15 mm FWHM. The absolute sensitivity of the PET system at the centre of the system was measured as 3.86 cps/kBq (0.4%).

5.4.3   Combined PET-CT: Phantom Measurements

Figure 5.4 shows reconstructed PET and CT images from the phantom data set. Both images are of high quality, and do not demonstrate any noticeable artifacts due to the simultaneous acquisition. The holes containing ^{18}F are clearly visualized in the PET image and are accurately registered with the CT images.
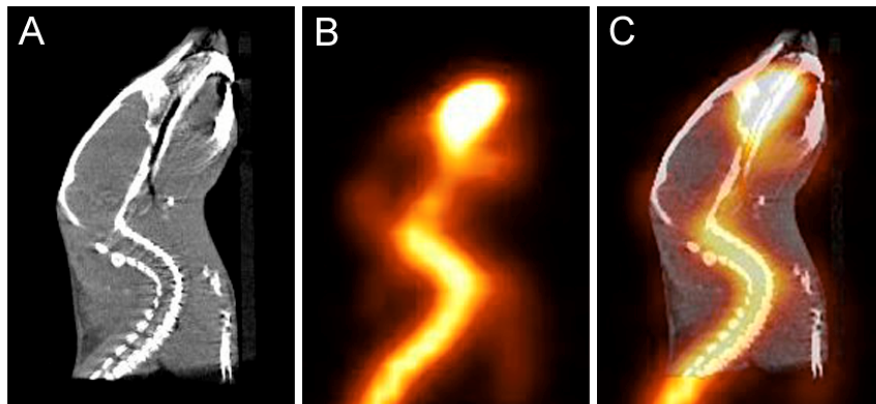
Figure 5.5. Scan of a mouse 3 hours after the injection of 26 MBq of ^{18}F$^-$, a radiotracer that accumulates in bone. Shown here are sagittal slices through the CT scan (A), the PET scan (B), and the fused PET-CT scan (C). Note the overlap of the PET activity with the location of the bones in the CT image. The scan was acquired using 400 views in a time of 38 minutes.

5.4.4   Combined PET-CT: Mouse Measurements

Figure 5.5 shows reconstructed images from the $^{18}F^-$ bone scan of the mouse. Good agreement can be seen between the location of bone in the CT image and the location of bone in the PET image. The quality of the images is excellent and the CT and PET signals are well aligned.

Figure 5.6 shows reconstructed images from the ^{18}F-FDG *in vivo* scan of a mouse, showing extraction of ^{18}F-FDG by the kidneys and excretion into the bladder. The superposition of the PET signal with the appropriate anatomy in the CT image is evident. Once again, no artifacts are apparent in either image set. It should be noted that the bladder appears much larger in the PET image than in the CT image. This is due to the
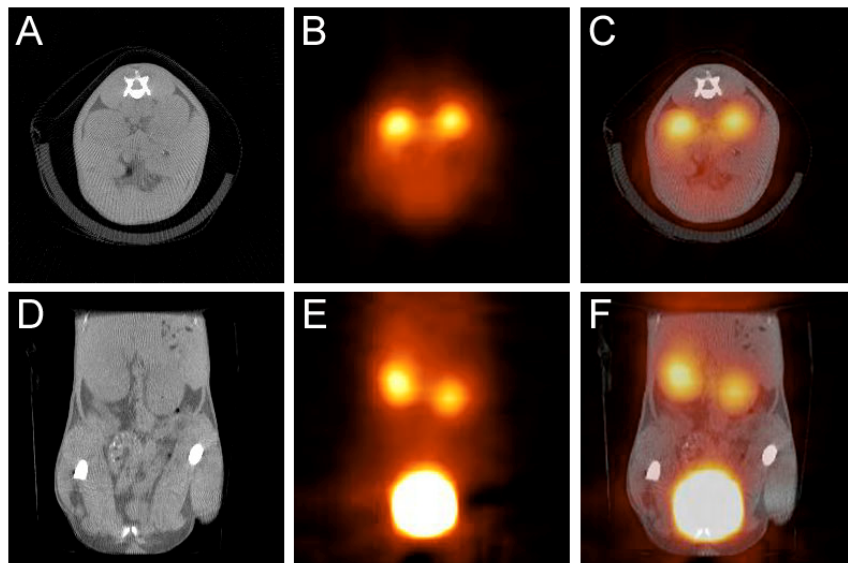
Figure 5.6. Simultaneous *in vivo* ^{18}F-FDG and CT scans of a mouse 50 minutes after injection of 8.5 MBq of ^{18}F-FDG. ^{18}F-FDG is a glucose analog that measures glucose metabolism and is cleared through the renal system. Note the strong signal in the kidneys and bladder in the PET images (transverse slice in B, coronal slice in E) and the corresponding position of the kidneys and bladder in the CT images (transverse slice in A, coronal slice in D). The fused transverse slice is shown in (C) and the coronal slice in (F). The scan was acquired using 200 views in a total scan time of 18 minutes.

extremely high concentration of ^{18}F-FDG in the bladder causing the signal level to exceed the colour scale window of the image.

5.5 Discussion

These results demonstrate the feasibility of simultaneously performing anatomical and molecular imaging *in vivo* using the complementary techniques of PET and x-ray CT. No noticeable artefacts due to the simultaneous acquisition were seen in either the CT or PET images acquired.

This bench top system, while proving the principle of simultaneous PET/CT imaging, does exhibit a number of limitations that must be addressed in order to produce a system suitable for routine *in vivo* studies in the mouse. These limitations include the vertical mounting and rotation of the mouse in the system, the relatively coarse spatial resolution of the PET detectors used, and the need to extend the detector area to be able to cover the entire body of the mouse with a single rotation. The PET data is not quantitative due to a lack of randoms, scatter, deadtime, and attenuation corrections. It should be pointed out that the randoms and deadtime correction should be minimal since the amount of activity in the mouse was kept to a minimal amount. The attenuation correction for a mouse is on the order of 10 – 20%. Another factor to note is that the imaging time required can be reduced by as much as 50% once a new generation of data acquisition system is employed. The current system uses separate data acquisition computers for the PET and CT components and the communication overhead between the two machines has been found to be much longer than is acceptable.

Chapter 6. Future Directions

6.1 Combined microPET/microCT Imaging

The microPET/microCT system designed and constructed for this research produced very promising results, but also exhibited many limitations, as discussed in section 5.5. In order to address these shortcomings, the next generation combined PET-CT system could include PET detectors recently developed that achieve close to 1 mm intrinsic spatial resolution [Chatziioannou *et al* 2001]. Since the PET system will only consist of a partial ring of detectors, the axial field of view of the PET system should be expanded to compensate for the loss in sensitivity. In this way, the partial ring can have as many detector elements as a full ring scanner, albeit in a different configuration. Designing and constructing a gantry, as shown in figure 6.1, that will allow the mouse to
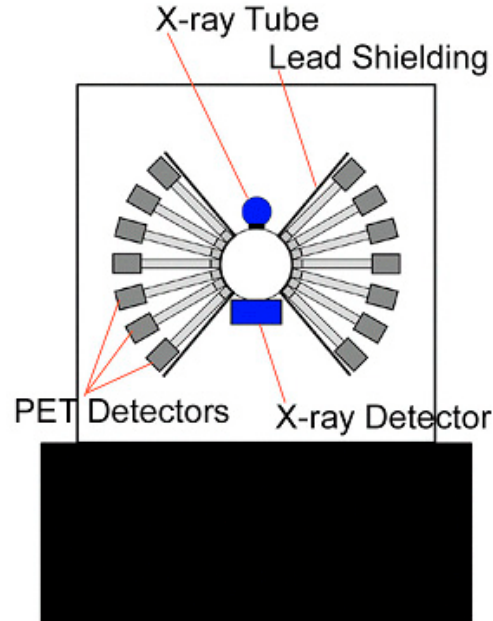
Figure 6.1. Concept drawing showing a combined microPET/microCT system in which the mouse is placed horizontally and the detectors rotate about the mouse.

be positioned horizontally, and in which the detectors and x-ray tube rotate around the mouse, will make reproducible scanning much simpler. Horizontal positioning is also much better tolerated by the mouse and the stationary animal allows physiologic monitoring lines to be attached during a study. Designing such a system requires study of the optimum rate of rotation of the gantry, with both continuous rotation and step and shoot methods needing investigation. The impact of a continuously rotating gantry on the CT image quality will also need investigation.

Since the detectors in such a system would be identical to those used in the microPET II system [Chatziioannou et al., 2001], the PET system performance should be similar to that obtained with the microPET II scanner.

Having the PET and CT systems combined on a single gantry will allow an accurate geometric offset calibration between the two systems to be measured. Since the gantry is fixed, this calibration will remain constant for the lifetime of the system. Knowing this offset will allow routine side by side use of the PET and CT data, unlike in the current system, where the data had to be manually registered for each data set. Besides the advantages of displaying the data together to help with interpretation of the PET data, the alignment of the two systems means that the CT data can be used to improve the quantification of the PET data through corrections requiring accurate anatomical information, such as attenuation correction [Visvikis et al., 2003] and scatter correction of the PET data [Holdsworth et al., 2002]. Before the CT data can be used to correct the PET data, accurate methods of converting the reconstructed μ values from the CT scan into μ values for the PET 511 keV annihilation photons are needed. This could

be particularly problematic with the a-Se based detector system, since as seen in section 3.4.7, the μ value for water changes with repeat scanning.

Material	Z	Density (g/cm^3)	K edge (keV)	L edge (keV)	Ratio of μ 25keV:511keV	Ratio of μ 40keV:511keV
Al	13	2.70	1.56	0.118	63.5	12.4
Fe	26	7.87	7.11	0.846	465.2	112.8
Cu	29	8.96	8.98	1.10	614.0	174.6
Mo	42	10.22	20.0	2.87	1374.5	355.8
Sn	50	7.31	29.2	4.46	285.9	470.4
W	74	19.3	69.5	12.1	484.7	129.1
Pb	82	11.35	88.0	15.9	532.2	143.6

Table 6.1. Comparison of various possible shielding materials.

In the work for this project, lead was the only element considered as a shielding material for the PET detectors. However, as shown in table 6.1, lead is probably not the optimal choice. If the ratio of attenuation at low energies to high energies is used as the sole metric for comparing shielding materials, than lead places third in the list of candidates, behind molybdenum and copper. Since the attenuation is highly dependent on the energy of the K and L edges, it is also quite possible that a layered approach to shielding should be considered, in order to take advantage of the unique absorption properties of individual materials. A clear example of this is the case of tin, which has a relatively poor ratio of attenuation at 25 keV to attenuation at 511 keV of 286, but the ratio rises to 470 for 40 keV:511keV attenuation, the best ratio of any material.

The results of chapter 4 showing that dose to the mouse decreases as x-ray energy increases means that in the future it is very likely that higher energy x-ray beams will be

used, perhaps in the 60 to 80 keV range. If this is the case, then the amount of shielding used will need to be increased and the optimal shielding materials will change.

6.2 microCT Imaging

There are currently no agreed upon standards for the evaluation of mouse microCT imaging systems. Thus there is no simple way to compare the performance of systems made by two different manufacturers. This is clearly a problem that is going to need to be addressed, likely by a committee of users and physicists. Standards for measuring signal to noise ratios, low contrast object detectibility, and resolution are required. Ideally, a phantom needs to be constructed that would provide a standard object to be imaged on different systems. The phantom should include several key factors, such as regions of different materials (for contrast), a series of closely spaced holes or grooves (for resolution), and a uniform region (to measure noise).

Having a standard phantom will also provide the additional advantage of providing an object that can be imaged routinely on a system to ensure that the performance of the system has not changed with time. It also will make it much easier to assess whether changes made to the system through changes to the geometry, source, detector, scanning protocol, etc. had a positive or negative impact. Very few test objects were scanned on the prototype microCT system built for this research, largely due to a lack of standard objects to image. As a result, little is known about how the performance of the system has changed with time.

The majority of the microCT work for this project was carried out using the a-Se detector, which as shown in chapter 3 has a very high DQE relative to indirect detectors. Yet the question remains of whether the a-Se device is a superior CT detector. The results of section 3.4.7 show that the reconstructed CT images from the a-Si detector were less noisy than those acquired using the a-Se device. Further study is required to determine the effects of detector pixel size on the noise in the reconstructed image.

The TLD dose measurements of chapter 4 included only a single measurement, utilizing three TLDs, of the dose in a mouse *ex vivo*. In order to validate the dose measurement results, further mouse dosimetry will be required. The goal of the further studies should be to specifically compare the dose in the mouse to the dose in the phantom to validate that the dose to the phantom correlates well with the dose to the mouse. Since placing TLDs in the phantom is much simpler than placing them in a mouse, it would definitely be preferable to study the dose to a phantom, but this is not possible until the validation is complete. If further studies involving implanting TLDs into mice *ex vivo* are to be performed, then a reliable method of encapsulating the TLDs must be developed. This encapsulation is necessary to protect the TLDs from moisture and light.

It seemingly has become accepted that cone beam microCT systems using flat-panel detectors are the best way to build a mouse imaging system. However, cone-beam systems are inherently susceptible to scatter. The magnitude of the effect of the scatter has never been investigated for a mouse-imaging system. A simple technique such as collimating the x-ray beam at the source, so that the beam is a fan instead of a cone,

would allow the differences between fan-beam and cone-beam image quality to be assessed. If fan-beam systems prove to be greatly superior in performance, then a redesign of microCT imaging systems should be considered. Besides the improvement in scatter, a fan beam system would allow exact reconstruction through 2-D filtered back projection, rather than the approximate methods of the Feldkamp cone-beam algorithm. The limiting factor for fan-beam imaging of a mouse has traditionally been low x-ray tube output. However, new x-ray tube models capable of higher output are being introduced which could make this a practical reality.

Appendix A. Effect of Phantom Voxelization in CT Simulations

A.1 Introduction

The ideal description of a phantom in a x-ray CT computer simulation closely approaches the almost continuous nature of a physical object. Analytical phantoms such as the Shepp-Logan head phantom [Shepp and Logan, 1974] or the mathematical cardiac torso (MCAT) phantom [Tsui et al., 1993] are confined to continuous smooth geometrical shapes and are useful for testing reconstruction algorithms [Feldkamp et al., 1984; Nuyts et al., 1998]. Analytical phantoms can also be easily deformed by stretching to simulate moving anatomy such as a beating heart [Peter et al., 1999; Pretorius et al., 1997]. This approach, however, can have problems with describing complex 3D shapes due to the large number of surfaces involved. Realistic phantoms of biological systems are composed of many geometrical shapes and thus using them in a simulation can be difficult due to the overhead involved of keeping track of which objects are overlaid on others, what material in located within the overlapping regions, and calculating intersection points with complex object shapes. Many such simulations therefore use a voxelized phantom representation [Lazos et al., 2000; Guan and Gordon, 1996] due to the simpler data generation problem and the ability to define biologically accurate phantoms using MRI or CT scans [Collins et al., 1998].

Discretization of the phantom introduces errors since the phantom edges are no longer smooth but rather are composed of cubic edges. However, if the assumption is made that a finely sampled phantom matrix is a very good approximation to the continuous phantom case, then a simulation using an extremely fine voxelized phantom

description should be equivalent to a simulation with a continuous phantom. Such fine phantom matrices can mean greatly increased computation time and computer memory requirements. Thus as coarse a phantom matrix as possible should be used and as few rays as possible traced in order to speed up the simulation while avoiding artifacts due to the discretization of the phantom.

When computer simulations are being used to optimize scanner geometry or validate reconstruction algorithms, it is important to be certain that phantom voxelization is not influencing the results of the simulation since the discretization of the phantom is an inherently artificial construct. A search of the literature revealed no recommendations on what phantom matrix size was acceptable to produce simulations free of discretization induced artifacts. It was also found that no recommendations existed for how many rays should be projected through the phantom matrix per detector element. To avoid discretization errors in our discrete simulations, while minimizing computation time, we
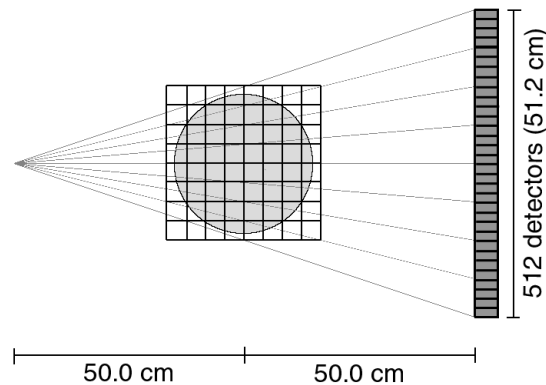
Figure A.1. Diagram of geometry used in the simulations. The phantom matrix size was varied from 256 voxels square to 8192 voxels square, contained within a 51.2 cm^2 area.

wanted to determine some guidelines with respect to how coarsely we could voxelize a phantom and how few line integrals we needed to calculate.

A.2 Methods

A.2.1   Simulation Geometry

A fan beam geometry with a linear detector of 512 pixels was used as illustrated in figure A.1. The phantom was at the centre of rotation, halfway between the source and detector. The geometry was that of a human CT scanner with the source-phantom distance and the phantom-detector distance both being 50 cm. The detector pixel size was 1 mm. For computational ease the x-ray source was considered to be a point source. This simplification also has the advantage of avoiding any smoothing of the projection data due to blurring induced by a finite sized source which could mask the artifacts that are being examined. Line integrals were calculated by tracing rays through the phantom using the method of Siddon [Siddon, 1985]. The Siddon method was used since it calculates the exact path length through a matrix. No interpolation was used since we wished to look at the worst case scenario for artifacts. The number of rays traced per detector pixel was 1, 2, 4, 8, or 16. 1000 projection angles were calculated for each data set. The images were reconstructed on a 512×512 matrix using the RECLBL FBP reconstruction package [Huesman et al., 1977] with a pixel size of 0.5 mm, equal to the detector element size projected to the centre of rotation. A ramp filter was used for all reconstructions. Since statistical noise is the dominant noise factor in CT [Cohen and DiBianca, 1979], simple Poisson noise was added to the projection data at levels simulating 10^3 to 10^7 photons per detector element prior to attenuation. These numbers

Figure A.2. Rebinning a phantom onto a coarser matrix by summing small voxels into larger ones. Each rebinning increased the length of a voxel side by a factor of 2.
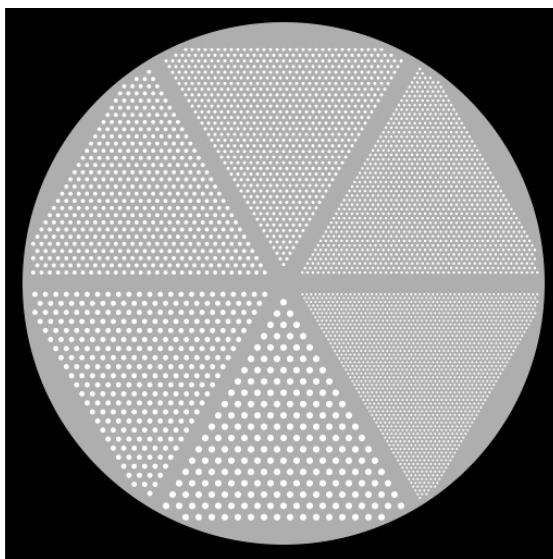
Figure A.3. Rod type phantom designed to test effects of phantom voxelization on a high frequency object.
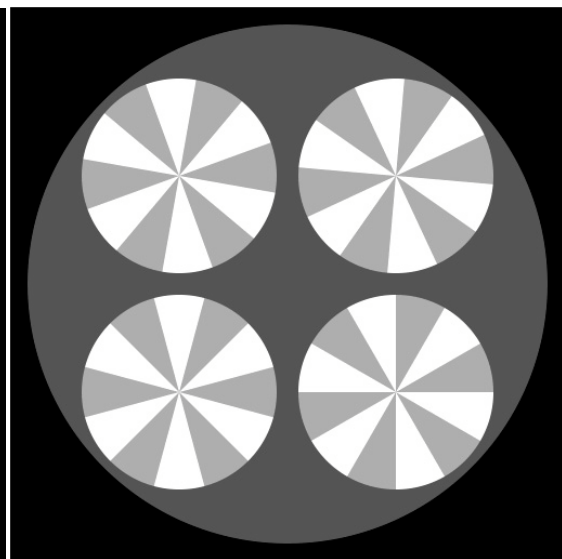
Figure A.4. Pie type phantom designed to test effects of phantom voxelization on a low frequency object.

of photons simulate noise levels of between 10% and 0.03% in the projection data. 10^6 –

10^7 photons correspond to levels commonly encountered in clinical CT procedures [Guan

and Gordon, 1996].

A.2.2   Phantoms

Phantoms were constructed on an 8192×8192 matrix with a voxel size equal to 0.03125 mm (0.0625 times the reconstructed voxel size). The phantoms were then rebinned onto coarser matrix sizes of 4096, 2048, 1024, 512, and 256 voxels square as shown in figure A.2.

Three types of phantoms were used in the simulations. The first was a rod phantom shown in figure A.3, designed to test the effects of voxelization on high frequency objects. This phantom consisted of a 24 cm diameter water equivalent cylinder (relative density = 1) with higher density rods inserts. The rods had diameters of 3, 2.4, 1.9, 1.5, 1.2, and 1.0 mm. Two versions of this phantom were used. The first was high contrast, with the rods having a density 50% higher (relative density = 1.5) than the background, and the second was low contrast, with the rods being 1% more dense (relative density = 1.01) than the background. The second phantom was a pie type phantom, shown in figure A.4, designed to test the effects of phantom voxelization on straight boundaries oriented at small angles to the phantom matrix. This phantom consists of a 24 cm diameter water equivalent cylinder with inserts that have alternating density values of 2 and 3 times the background (water) value. The third phantom was a 20 cm diameter uniform water cylinder designed to see if effects were caused by differences at the edge of a cylinder. Attenuation values for the phantoms were chosen to simulate a monoenergetic 100 keV photon beam in order to properly calculate the statistical noise after attenuation.

A.2.3   Analysis

Differences were assessed in the reconstructed images in three ways. Firstly, images were compared qualitatively by visual inspection. Secondly, profiles were drawn through the images and compared to the "exact" solution, which was the phantom rebinned onto a 512×512 matrix with the same voxel size as the reconstructed image. The rebinned phantom was used in order to eliminate the possibility that errors seen were due only to the fact that the image was being displayed on a 512×512 matrix. Finally, the average fractional error (AFE) was calculated by comparing the reconstructed image to the "gold standard", which was the reconstructed image from the noise free simulation with the finest phantom matrix (8192×8192). The AFE was defined as the sum of the absolute differences between the reconstructed image of interest and the gold standard image divided by the average voxel value in the gold standard image. The AFE is only evaluated for voxels contained within the phantom region only. Other quantitative measures such as mean square error were investigated but it was found that they all behaved in a very similar manner to the measure of AFE.
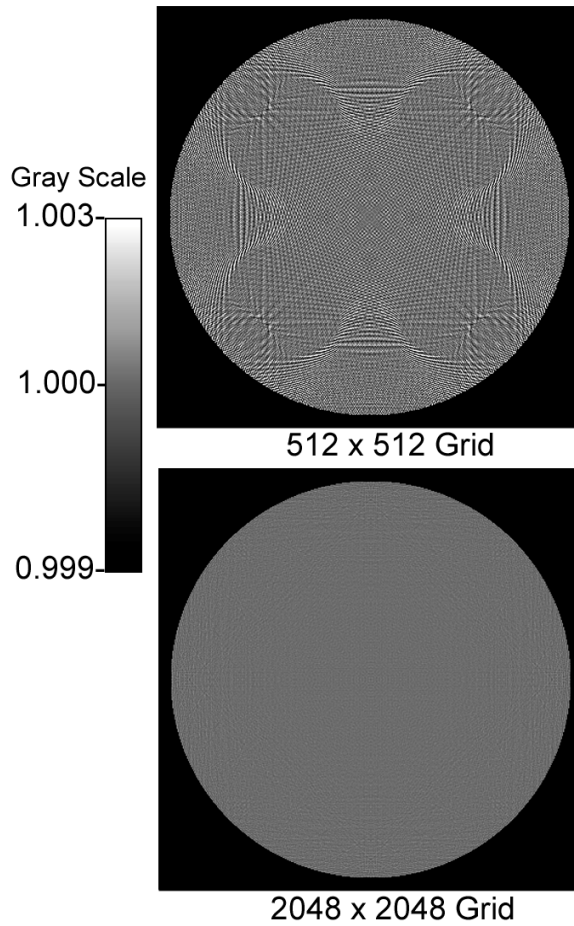
Figure A.5. Effect of voxelization on a noise free simulation of a uniform cylinder phantom. The pattern seen in the 512 voxel image is due only to discretization differences at the edge of the cylinder. These effects are not seen in the finer matrix simulation.
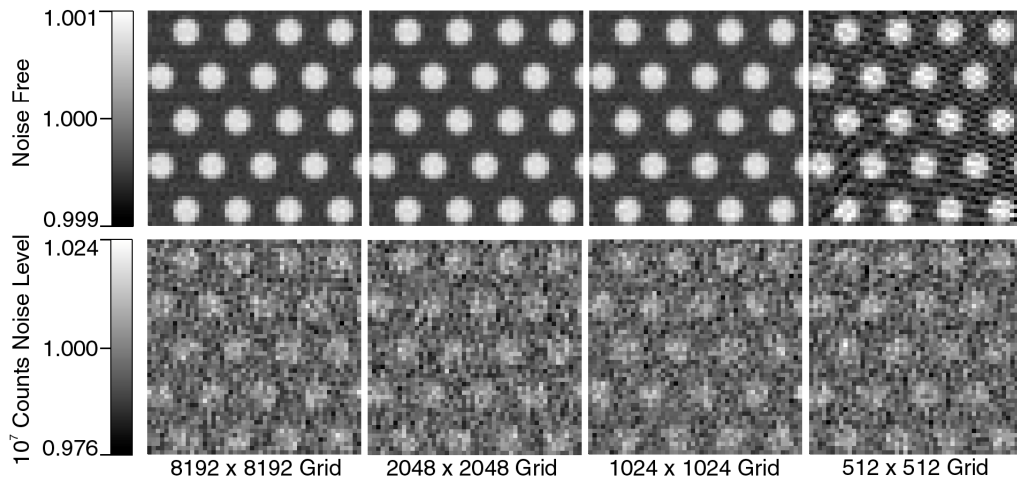
Figure A.6. Detail of 3 mm rods in the low contrast rod phantom for different simulation matrix sizes. Note different grey scales for upper and lower rows. For the noise free case, no appreciable differences are seen by using a grid finer than 1024 voxels square. For noisy data, using a finer matrix results in no visible improvement.

A.3 Results

A.3.1 Qualitative Assessment

Fig. A.5 shows the effects of phantom voxelization on the uniform phantom when the number of rays traced per detector is held constant at 16. On a compressed gray scale (0.997 – 1.003), "interference" type patterns are seen in the phantom due to differences in the phantom voxelization at the edge of the phantom. These effects are not seen in images with noise equivalent to 10^7 photons since they are small in amplitude (0.15% of water intensity) and are masked by the noise. Figure A.6 shows a region of the low
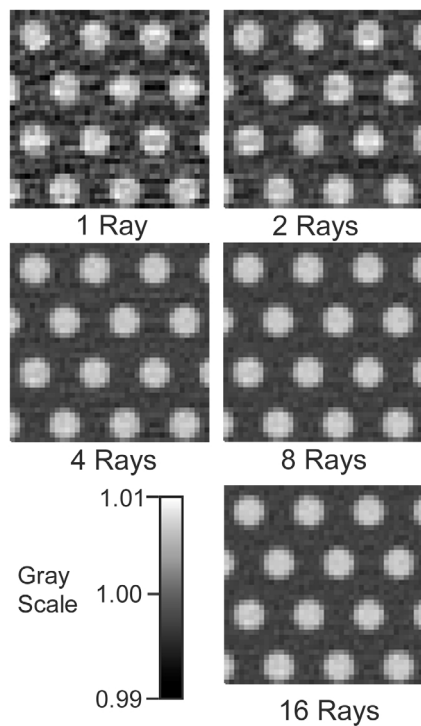
Figure A.7. Detail of 3 mm rods in the low contrast rod phantom for the 1024 simulation matrix with varying number of rays projected per detector. Using more than 4 rays per detector results in no visible improvement in image quality.
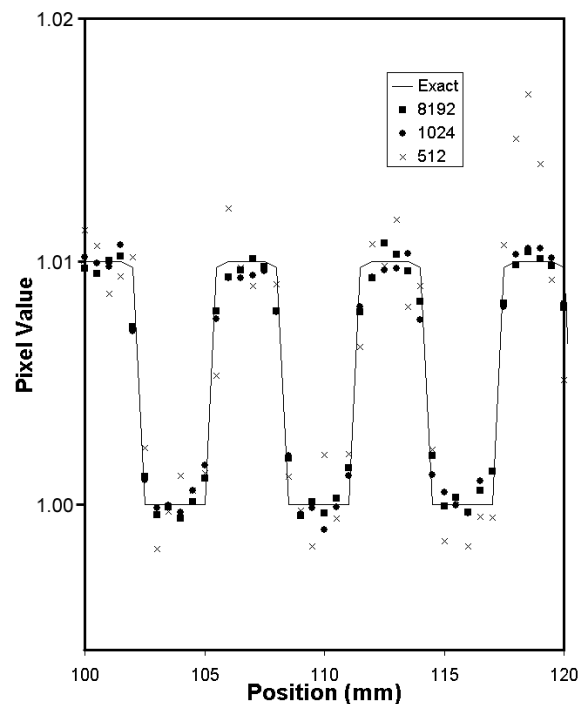
Figure A.8. Profiles through the 3 mm diameter rods in the low contrast rod phantom for different simulation matrix sizes with noise free projection data. There is not a substantial improvement beyond the 1024 phantom matrix size.
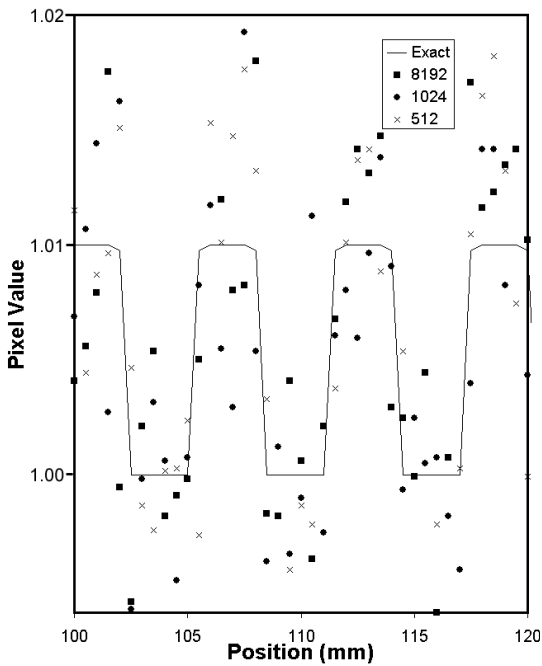
Figure A.9. Profiles through the 3 mm diameter rods in the low contrast rod phantom for different simulation matrix sizes with 10^7 photons noise level. Any improvement gained by using a finer phantom matrix is lost in the noise.
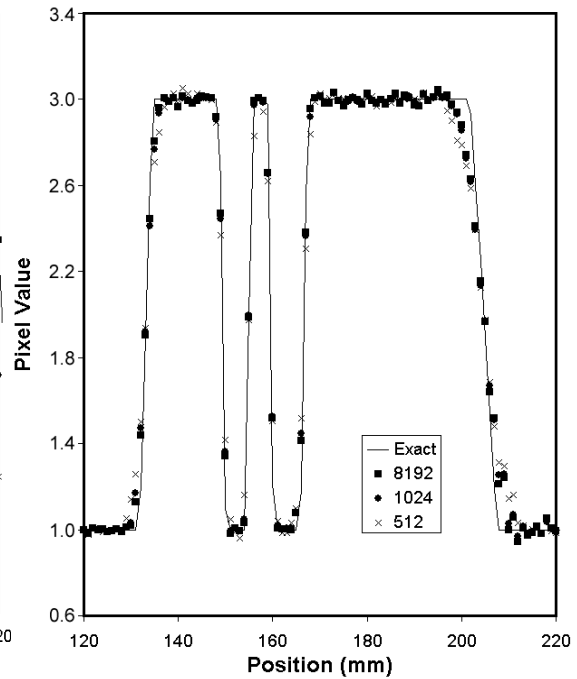
Figure A.10. Profiles through the pie phantom for different simulation matrix sizes with noise free data. Note the error at the 200 mm position due a partial volume effect in rebinning the phantom to a coarser resolution.
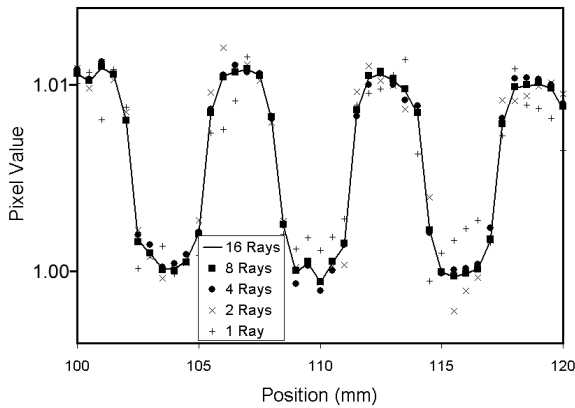
Figure A.11. Profiles through the 3 mm diameter rods in the low contrast rod phantom for different number of rays being traced with noise free data. There is no substantial improvement by projecting more than 4 rays per detector element.
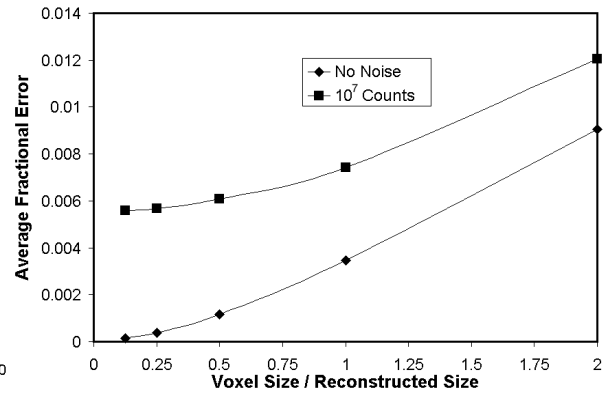
Figure A.12. Plot of AFE vs. voxel size for the uniform water phantom for projection data with 16 rays traced per detector pixel. The error in the noise free case continues to decrease. When noise is present the error converges to a non-zero value.
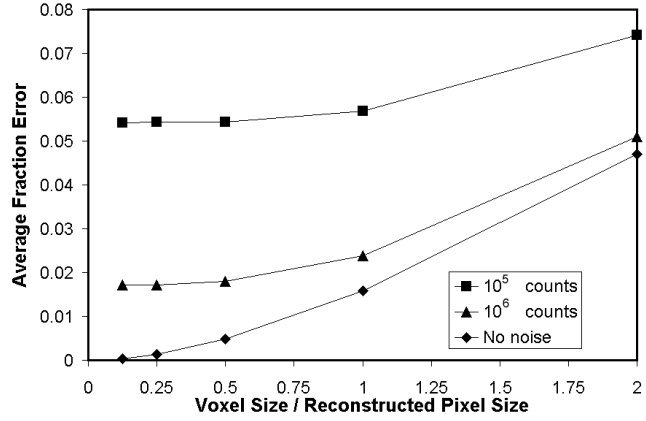
Figure A.13. Plot of AFE vs. voxel size for the high contrast rod phantom for projection data with 16 rays traced per detector pixel.
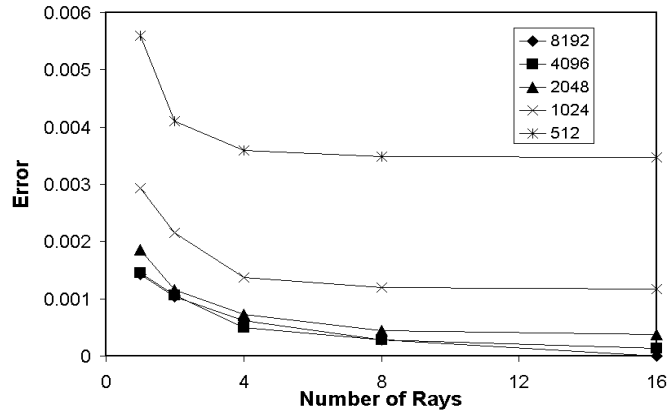
Figure A.14. Plot of AFE vs. number of rays traced for the uniform water phantom with noise free projection data. For all phantom matrix sizes, there is almost no improvement by projecting more than 4 rays per detector element.
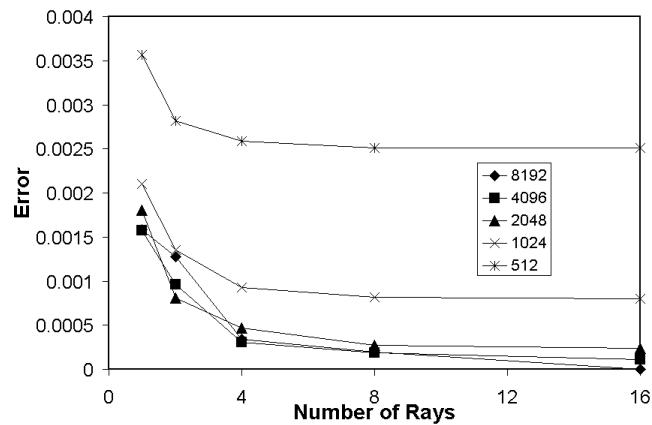
Figure A.15. Plot of AFE vs. number of rays traced for the low contrast rod phantom with noise free projection data. For all phantom matrix sizes, there is almost no improvement by projecting more than 4 rays per detector element.

contrast rod phantom containing the largest set of rods (3 mm diameter). The noise free images improve as the phantom matrix becomes finer but in the images from the data simulating 10^7 photons per detector, the improvement is lost in the noise. Figure A.7 shows a similar region for the case of tracing different numbers of rays for each detector pixel with no noise added to the data. It can be seen that there seems to be no noticeable improvement beyond the 4 rays per pixel image.

A.3.2   Image Profiles

Profiles through the low contrast rod phantom with no projection noise and 16 rays traced per detector element are shown in figure A.8. Profiles through the same phantom with noise corresponding to 10^7 photons are shown in figure A.9. It can be seen that the noise free reconstructions do not improve much beyond the 1024 matrix size and that when noise is added the noise masks the differences. Profiles through the noise free pie phantom simulation with 16 rays traced per detector element are shown in figure A.10. It can be seen in these profiles that even the finest matrix sizes do not always result in the reconstructed image exactly approaching the true object. This is likely due in part to discretization errors introduced by the backprojection step in the reconstruction process, and is not related to the simulation. Figure A.11 shows profiles through the 3 mm rods in the low contrast rod phantom for the case of varying the number of rays traced per detector pixel. It can be seen that no appreciable gain is achieved by using more than 4 rays per detector pixel.

A.3.3   Error in Images

The AFE vs. voxel size for the uniform phantom is plotted in figure A.12.   One can see that there is very little improvement by going to a voxel size smaller than half the reconstructed voxel size in the presence of realistic noise levels.   Figure A.13 shows the AFE vs. voxel size for the high contrast rod phantom.   In this plot the asymptotic behaviour of the AFE is even more pronounced.   The AFE vs. voxel size for the low contrast rod phantom behaves in much the same manner (not shown).   Figures A.14 and A.15 show the AFE versus number of rays for the uniform water phantom and low contrast rod phantoms, respectively.   Both plots show that there is not a sizeable improvement in the reduction of the AFE by going beyond 4 rays per detector pixel.

A.4 Conclusion/Discussion

When noise free data are reconstructed, voxelization effects can be seen even in uniform objects due to differences in the discretization at the edge of the object propagating inside the object.   For noise free data the error in the reconstructed images continues to decrease as the voxel size decreases.   When even small amounts of noise are added to the projection data, there is no appreciable gain be going to a phantom matrix with a voxel size finer than twice the reconstructed voxel size.   There is no appreciable improvement by tracing more than 4 rays per detector pixel, however there is a large improvement by tracing 4 rays versus just 1 or 2.   The results indicate that a voxelized phantom is sufficient for use in a simulation with realistic noise levels provided the phantom matrix is twice as fine as the reconstruction matrix and at least 4 rays per

detector pixel are traced. The use of a voxelized approach allows much more intricate and anatomically realistic phantoms to be created. In the case of a complicated analytical phantom, it may be quicker to voxelize the phantom and then run the simulation.

The results also indicate that the lower contrast the object of interest is in the image, the more likely one is to see artifacts due to phantom discretization in other areas with high contrast, such as the outer phantom boundaries. Thus more caution must be used when using voxelized phantoms in simulation to study such things as soft tissue contrast. It is likely that projecting rays through the phantom matrix using a stepping algorithm with interpolated pixel values could reduce some of the discretization errors if a small enough step size was chosen [Köhler et al., 2000]. Choosing a point x-ray source and using the Siddon ray tracing algorithm clearly combine to produce the worst case scenario but also probably means that the guidelines developed are safe or conservative. Future work could include testing how stepping algorithm with interpolation would impact the results and how the effect of a finite sized x-ray source.

References

Amundson et al., 2001	Amundson, S.A., Bittner, M., Meltzer, P., Trent, J. and Fornace Jr, A.J. "Induction of Gene Expression as a Monitor of Exposure to Ionizing Radiation." Radiat Res., 156:657-61, 2001.
Andre et al., 1998	Andre, M.P., Spivey, B., Martin, P. et al., "An Integrated CMOS-Selenium X-ray Detector for Digital Mammography." SPIE 3336:204-209, 1998.
Attix, 1986	Attix, F.H., "Introduction to Radiological Physics and Radiation Dosimetry." John Wiley & Sons, New York, 1986.
Azari et al., 1993	Azari, N.P., Pettigrew, K.D., Schapiro, M.B. et al., "Early detection of Alzheimer's disease: a statistical approach using positron emission tomographic data." J Cer Bl Fl Met., 13(3):438-47, 1993.
Bai et al., 2002	Bai, B., Li, Q., Holdsworth, C.H. et al., "Model-based normalization for iterative 3D PET image reconstruction." Phys Med Biol., 47(15):2773-84, 2002.
Beyer et al., 2000	Beyer, T., Townsend, D.W., Brun, T. et al., "A Combined PET/CT Scanner for Clinical Oncology." J Nuc Med., 41(8):1369-79, 2000.
Boone, 2001	Boone, J.M., "Determination of the presampled MTF in computed tomography." Med Phys., 28(3):356-60, 2001.
Budinger et al., 1996	Budinger, T.F., Brennan, K.M., Moses, W.W. and Derenzo, S.E., "Advances in positron emission tomography for oncology." Nucl Med Biol., 23(6):659-67, 1996.
Bushberg et al., 1994	Bushberg, J.T., Seibert, J.A., Leidholdt Jr., E.M., Boone, J.M., "The Essential Physics of Medical Imaging." Williams & Wilkins, Baltimore, 1994.
Casey and Hoffman, 1986	Casey, M.E. and Hoffman, E.J., "Quantitation in position emission computed tomography. VII. A technique to reduce noise in accidental coincidence measurements and coincidence efficiency calibration." J Comput Assist Tomogr., 10:845-50, 1986.
Chatziioannou et al., 1999	Chatziioannou, A.F., Cherry, S.R., Shao, Y. et al., "Performance Evaluation of microPET: A High-Resolution Lutetium Oxyorthosilicate PET Scanner for Animal Imaging." J Nuc

Med., 40(7):1164-75, 1999.

Chatziioannou et al., 2001 — Chatziioannou, A.F., Tai, Y.-C., Doshi, N. and Cherry, S.R., "Detector development for microPET II: a 1 μl resolution PET scanner for small animal imaging." Phys Med Biol., 46(11):2899-910, 2001.

Cherry and Gambhir, 2001 — Cherry, S.R. and Gambhir, S.S., "Use of positron emission tomography in animal research." Ilar J. 42(3):219-32, 2001.

Cherry et al., 1997 — Cherry, S.R., Shao, Y., Silverman, R.W. et al., "MicroPET: A High Resolution PET Scanner for Imaging Small Animals." IEEE Trans Nucl Sci., 44(3):1161-66, 1997.

Chotas et al., 1997 — Chotas, H.G., Carey, E.F., and Ravin, C.E., "Memory Artifact Related to Selenium-based Digital Radiography Systems." Radiology, 203:881-83, 1997.

Chow et al., 2001 — Chow, P.L., Goertzen, A.L., Berger, F. et al., "Monte Carlo Model for Estimation of Dose Delivered to Small Animals During 3D High Resolution X-ray Computed Tomography." Conference Record of IEEE NSS-MIC, San Diego, CA, 4-10 Nov., 2001.

Cohen and DiBianca, 1979 — Cohen, G. and DiBianca, F.A., "The use of contrast-detail-dose evaluation of image quality in a computed tomographic scanner." J Comput Assist Tomogr., 3:189-85, 1979.

Collins et al., 1998 — Collins, D.L., Zijdenbos, A.P. Kollokian, V. et al., "Design and Construction of a Realistic Digital Brain Phantom." IEEE Trans Med Imag., 17:463-68, 1998.

Contag et al., 2000 — Contag, C.H., Jenkins, D., Contag, P.R. and Negrin, R.S. "Use of reporter genes for optical measurements of neoplastic disease in vivo." Neoplasia. 2:41-52, 2000.

Corrigan et al., 1999 — Corrigan, N.M., Chavez, A.E., Wisner, E.R. and Boone, J.M., "A multiple detector array helical x-ray microtomography system for specimen imaging." Med Phys., 26(8):1708-13, 1999.

Czernin, 2002 — Czernin, J., "Clinical applications of FDG-PET in oncology." Acta Med Austriaca., 29(5):162-70, 2002.

Da Silva et al., 2001 — Da Silva, A.J., Tang H.R., Wong, K.H. et al., "Absolute quantification of regional myocardial uptake of 99mTc-sestamibi with SPECT: experimental validation in a porcine model." J

Nucl Med., 42:772-9, 2001.

Defrise et al., 1997   Defrise, M., Kinahan, P.E., Townsend, D.W., Michel, C., Sibomana, M. and Newport, D.F., "Exact and approximate rebinning algorithms for 3-D PET data." IEEE Trans Med Imag., 16:145-58, 1997.

Dobbins et al., 1995   Dobbins, J.T., Ergun, D.L., Rutz, L. et al., "DQE(f) of four generations of computed radiography acquisition devices." Med Phys., 22(10):1581-93, 1995.

Doshi et al., 2000   Doshi N.K., Shao, Y., Silverman, R.W. and Cherry, S.R., "Design and evaluation of an LSO PET detector for breast cancer imaging." Med Phys., 27:1535-43, 2000.

Feldkamp et al., 1984   Feldkamp, L.A., Davis, L.C. and Kress, J.W., "Practical cone-beam algorithm." J Opt Soc Am A, 1:612-19, 1984.

Ford et al., 2001   Ford, N.L., Thornton, M.M., and Holdsworth, D.W., "Fundamental Limits to Precision in Small-Animal Computer Tomography." 2001 High Resolution Imaging in Small Animals Conference, Rockville, Maryland.

Fornace et al., 2002   Fornace Jr, A.J., Amundson, S.A., Do, K.T. et al. "Stress-gene induction by low-dose gamma irradiation." Mil Med. 167(2 Suppl):13-5, 2002.

Foster et al., 2000   Foster, F.S., Pavlin, C.J., Harasiewicz, K.A., Christopher, D.A. and Turnbull, D.H., "Advances in ultrasound biomicroscopy." Ultrasound Med Biol. 26:1-27, 2000.

Fujita et al., 1992   Fujita, H., Tsai, D.-Y., Itoh, T. et al., "A simple method for determining the modulation transfer function in digital radiography." IEEE Trans Med Imaging, MI-11:34-39, 1992.

Gambhir, 2002   Gambhir, S.S., "Molecular imaging of cancer with positron emission tomography." Nat Rev Cancer, 2(9):683-93, 2002.

Gambhir et al., 2000   Gambhir, S.S., Herschman, H.R., Cherry, S.R. et al., "Imaging Transgene Expression with Radionuclide Imaging Technologies." Neoplasia, 2(1-2):118-138, 2000.

Goode et al., 1999   Goode, A.R., Williams, M.B., Simoni, P.U. et al., "A System for Dual Modality Breast Imaging." 1999 IEEE Medical Imaging Conference, Seattle, WA.

Guan and Gordon, 1996	Guan, H. and Gordon, R., "Computed tomography using algebraic reconstruction techniques (ARTs) with different projection access schemes: a comparison study under practical situations." Phys Med Biol., 41:1727-43, 1996.
Hoffman et al., 1982	Hoffman, E.J., Huang, S.-C., Plummer, D. and Phelps, M.E., "Quantitation in positron emission computed tomography. VI. Effect of nonuniform resolution" J Comp Assist Tomogr., 6:987-99, 1982.
Holdsworth et al., 2002	Holdsworth, C.H., Levin, C.S., Janecek, M., Dahlbom, M. and Hoffman, E.J., "Performance analysis of an improved 3-D PET Monte Carlo simulation and scatter correction." IEEE Trans Nuc Sci., 49:83-9, 2002.
Hounsfield, 1973	Hounsfield, G.N., "Computerized transverse axial scanning (tomography). 1. Description of System." Br J Radiol., 46(552):1016-22, 1973.
Hounsfield, 1980	Hounsfield, G.N., "Nobel Award address. Computer medical imaging." Med Phys., 7(4):283-90, 1980.
Huesman et al., 1977	Huesman, R.H., Gullberg, G.T., Greenberg, W.L. and Budinger, T.F., "RECLBL Library Users Manual." Lawrence Berkeley Laboratory, Berkeley, CA, Pub 214, 1977.
Iwata et al., 2000	Iwata, K., Kwon, S.-I., Hasegawa, B.H. et al., "Description of a prototype combined CT-SPECT system with a single CdZnTe detector." Conference record of 2000 IEEE Nuclear Science Symposium and Medical Imaging Conference, Lyon, France.
Jacobs et al., 1999	Jacobs, R.E., Ahrens, E.T., Meade, T.J. and Fraser, S.E., "Looking deeper into vertebrate development." Trends Cell Biol. 9:73-6, 1999.
Jeavons et al., 1999	Jeavons, A.P., Chandler, R.A. and Dettmar, C.A.R., "A 3D HIDAC-PET camera with sub-millimetre resolution for imaging small animals." IEEE Trans Nuc Sci. 46:468-73, 1999.
Johnson et al., 1997	Johnson, G.A., Benveniste, H., Engelhardt, R.T., Qui, H. and Hedlund, L.W., "Magnetic resonance microscopy in basic studies of brain structure and function." Ann N Y Acad Sci. 820:139-47, 1997.
Jorgensen et al., 1998	Jorgensen, S.M., Demirkaya, O. and Ritman, E.L., "Three-dimensional imaging of vasculature and parenchyma in intact

rodent organs with X-ray micro-CT." Am J Physiol. 275:H1103-14, 1998.

Karellas et al. 1992   Karellas, A., Harris, L.J., Liu, H., Davis, M.A. and D'Orsi, C.J., "Charge-coupled device detector: Performance considerations and potential for small-field mammographic imaging applications." Med Phys., 19(4):1015-23, 1992.

Kinahan et al., 1998   Kinahan, P.E., Townsend, D.W., Beyer, T. and Sashin, D., "Attenuation correction for a combined 3D PET/CT scanner." Med Phys., 25:2046-53, 1998.

Köhler et al., 2000   Köhler, T., Turbell, H., and Grass, M., "Efficient Forward Projection Through Discrete Data Sets Using Tri-Linear Interpolation." Conference Record of 2000 IEEE Nuclear Science Symposium and Medical Imaging Conference, Lyon, France.

Lanza and Wickline, 2001   Lanza, G.M. and Wickline, S.A. "Targeted ultrasonic contrast agents for molecular imaging and therapy." Prog. Cardiovasc. Dis. 44:13-31, 2001.

Lazos et al., 2000   Lazos, D., Kolitsi, Z. and Pallikarakis, N., "A Sortware Data Generator for Radiographic Imaging Investigation." IEEE Trans Inf Tech Biom. 4:76-79, 2000.

Lecomte et al., 1996   Lecomte, R., Cadorette, J., Rodrigue, S. et al., "Initial Results from the Sherbrooke Avalanche Photodiode Positron Tomograph." IEEE Trans Nuc Sci. 45(3):1952-57, 1996.

Loening and Gambhir, 2001   Loening, A.M. and Gambhir, S.S., "AMIDE: A completely free system for medical imaging data analysis." J Nucl Med., 42:827, 2001.

Louie et al., 2000   Louie, A.Y., Huber, M.M., Ahrens, E.T. et al., "In vivo visualization of gene expression using magnetic resonance imaging." Nat. Biotechnol. 18:321-5, 2000.

McDaniel et al., 2001   McDaniel, B., Sheng, H., Warner, D.S., Hedlund, W. and Benveniste, H., "Tracking brain volume changes in C57BL/6J and ApoE-deficient mice in a model of neurodegeneration: a 5-week longitudinal micro-MRI study." Neuroimage. 14:1244-55, 2001.

Meltzer et al., 1990   Meltzer, C., Leal, J.P., Mayberg, H.S. and Wagner, F.J.J., "Correction of PET data for partial volume effects in human

cerebral cortex by MR imaging." J Comput Assist Tomogr., 14:561-70, 1990.

Ntziachristos et al., 2002   Ntziachristos, V., Tung, C.H., Bremer, C. and Weissleder, R., "Fluorescence molecular tomography resolves protease activity in vivo." Nat Med. 8:757-60, 2002.

Nuyts et al., 1998   Nuyts, J., De Man, B., Dupont, P. et al., "Iterative reconstruction for helical CT: a simulation study." Phys Med Biol., 43:729-37, 1998.

Pan et al., 1998   Pan, L., Zan, L. and Foster, F.S., "Ultrasonic and viscoelastic properties of skin under transverse mechanical stress in vitro." Ultrasound Med Biol. 24:995-1007, 1998.

Patchen et al., 1992   Patchen M.L., MacVittie T.J., and Souza L.M., "Postirradiation treatment with granulocyte colony-stimulating factor and preirradiation WR-2721 administration synergize to enhance hemopoietic reconstitution and increase survival." Int J Radiat Oncol Biol Phys., 22(4):773-9, 1992.

Paulus et al., 1999   Paulus, M.J., Sari-Sarraf, H., Gleason, S.S. et al., "A new X-ray computed tomography system for laboratory mouse imaging." IEEE Trans Nuc Sci., 46(3):558-64, 1999.

Paulus et al., 2000   Paulus, M.J., Gleason, S.S., Kennel, S.J. et al., "High Resolution X-ray Computed Tomography: An Emerging Tool for Small Animal Cancer Research." Neoplasia, 2(1-2):62-70, 2000.

Paulus, 2003   Paulus, M.J., Private communication.

Peter et al., 1999   Peter, J., Gilland, D.R., Jaszczak, R.J. and Coleman, R.E., "Four-Dimensional Superquadric-Based Cardiac Phantom for Monte Carlo Simulation of Radiological Imaging Systems." IEEE Trans Nuc Sci., 46:2211-17, 1999.

Phelps, 2000   Phelps, M.E., "PET: the merging of biology and imaging into molecular imaging." J Nucl Med., 41(4):661-81, 2000.

Phelps et al., 1978   Phelps, M.E., Hoffman, E.J., Huang, S.C., and Kuhl, D.E., "ECAT: a new computerized tomographic imaging system for positron-emitting radiopharmaceuticals." J Nuc Med., 19(6):635-47, 1978.

Phelps et al., 1979   Phelps, M.E., Huang, S.-C., Hoffman, E.J. et al., "Tomographic measurement of local cerebral glucose metabolic rate in humans

with (F-18)2-fluoro-2-deoxy-D-glucose: validation of method." Annals of Neurology, 6(5):371-88, 1979.

Press et al., 1989   Press, W.H., Flannery, B.P., Teukolsky, S.A. and Vetterling, W.T., "Numerical Recipes in C." Cambridge University Press, New York, 1989.

Pretorius et al., 1997   Pretorius, P.H., Xia, W., King, M.A. et al., "Evaluation of right and left ventricular volume and ejection fraction using a mathematical cardiac torso phantom for gated pool SPECT." J Nuc Med., 38:1528-34, 1997.

Rahn et al., 1999   Rahn, J.T., Lemmi, F., Mei, P. et al., "High resolution, high fill factor a-Si:H sensor arrays for optical imaging x-ray medical imaging." Conference record of Amorphous and Heterogeneous Silicon Thin Films: Fundamentals to Devices – 1999 Symposium, Mater Res Soc., pp. 809-14.

Ruegsegger et al., 1996   Ruegsegger, P., Koller, B. and Muller, R., "A microtomographic system for the nondestructive evaluation of bone architecture." Calcif Tissue Int. 58:24-9, 1996.

Shao et al., 1997   Shao, Y., Cherry, S.R., Farahani, K. et al., "Simultaneous PET and MR imaging." Phys Med Biol., 42:1965-70, 1997.

Sharpe et al., 2002   Sharpe, J., Ahlgren, U., Perry, P. et al., "Optical Projection Tomography as a Tool for 3D Microscopy and Gene Expression Studies." Science. 296:541-5, 2002.

Shepp and Logan, 1974   Shepp, L.A. and Logan, B.F., "The Fourier reconstruction of a head section." IEEE Trans Nuc Sci., 21:21-43, 1974.

Siddon, 1985   Siddon, R.L., "Fast calculation of the exact radiological path length for a three-dimensional CT array." Med Phys., 12:252-55, 1985.

Slates et al., 1999a   Slates, R.B., Farahani, K., Shao, Y. et al., "A study of artefacts in simultaneous PET and MR imaging using a prototype MR compatible PET scanner." Phys Med Biol., 44(8):2015-27, 1999.

Slates et al., 1999b   Slates, R., Cherry, S., Boutefnouchet, A. et al., "Design of a small animal MR compatible PET scanner." IEEE Trans Nuc Sci., 46(3):565-70, 1999.

Sorenson and Phelps, 1987   Sorenson, J.A. and Phelps, M.E., Physics in nuclear medicine, 2nd ed. Orlando, FL, Grune and Stratton, 1987.

Tai et al., 2001   Tai, Y.C., Chatziioannou, A., Siegel, S. et al., "Performance evaluation of the microPET P4: a PET system dedicated to animal imaging." Phys Med Biol. 46:1845-62, 2001.

Tang et al., 1999   Tang, H.R., Brown, J.K., Da Silva, A.J. et al., "Implementation of a Combined X-ray CT-Scintillation Camera Imaging System for Localizing and Measuring Radionuclide Uptake: Experiments in Phantoms and Patients." IEEE Trans Nuc Sci., 46(3):551-57, 1999.

Tsui et al., 1993   Tsui, B.M.W., Terry, J.A. and Gullberg, G.T., "Evaluation of cardiac cone-beam SPECT using observer performance experiments and ROC analysis." Inv Rad., 28:1101-12, 1993.

Vandenberghe et al., 2001   Vandengerghe, S., D'Assler, Y., Van de Walle, R. et al., "Iterative reconstruction algorithms in nuclear medicine." Comput Med Imaging Graph. 25(2):105-11, 2001.

Vaquero et al., 2001   Vaquero, J.J., Seidel, J., Lee, I, Barbosa, F.J., and Green, M.V., "The NIH ATLAS Small Animal PET Scanner." 2001 High Resolution Imaging in Small Animals Conference, Rockville, Maryland.

Vedantham et al., 2000   Vedantham, S., Karellas, A., Suryanarayanan, S. et al., "Full breast digital mammography with an amorphous silicon-based flat panel detector: Physical characteristics of a clinical prototype." Med Phys., 27(3):558-67, 2000.

Visvikis et al., 2003   Visvikis, D., Costa, D.C., Croasdale, I. et al., "CT-based attenuation correction in the calculation of semi-quantitative indices of [(18)F]FDG uptake in PET." Eur J Nucl Med Mol Imaging., 30(3):344-53, 2003.

Weissleder et al., 1999   Weissleder, R., Tung, C.H., Mahmood, U. and Bogdanov, A., "In vivo imaging of tumors with protease-activated near-infrared fluorescent probes." Nat. Biotechnol. 17**:375-8, 1999.

Williams et al., 2000   Williams, M.B., Zhang, G., More, M.J. et al., "Integrated CT-SPECT system for small-animal imaging." SPIE, 4142:265-74, 2000

Yazaki et al., 2001   Yazaki, P.J., Shively, L., Clark, C. et al., "Mammalian expression and hollow fiber bioreactor production of recombinant anit-CEA diabody and minibody for clinical applications." J Immunol Methods, 253(1-2):195-208, 2001.

Zaidi and Hasegawa, 2003 Zaidi, H. and Hasegawa, B., "Determination of the attenuation map in emission tomography." J Nucl Med., 44(2):291-315, 2003.